

The background of the cover is a blue-tinted microscopic image showing a complex, interconnected network of cells or fibers, characteristic of a 3D tissue structure. The cells are roughly spherical and arranged in a porous, lattice-like pattern.

**3D Tissue Formation
The Kinetics Of Human
Mesenchymal Stem Cells**

Gustavo A. Higuera

3D Tissue Formation

The Kinetics Of Human Mesenchymal Stem Cells

Gustavo A. Higuera

Members of the Committee

Chairman:	Prof. Dr. M. Peters	University of Twente
Promoter:	Prof. Dr. C.A. van Blitterswijk	University of Twente
Assistant Promoter:	Dr. Ir. A.J.B. van Boxtel	Wageningen University
Members:	Prof. Dr. R.O.C. Oreffo	University of Southampton
	Prof. Dr. Ir. R.H. Wijffels	Wageningen University
	Prof. Dr. J.P.T.M. van Leeuwen	Erasmus MC
	Prof. Dr. V. Subramaniam	University of Twente
	Prof. Dr. H.F.J.M. Koopman	University of Twente
	Dr. J. de Boer	University of Twente

3D Tissue Formation

The Kinetics Of Human Mesenchymal Stem Cells

Gustavo A. Higuera

ISBN: 978-90-365-3065-1

The research described in this book was financially supported by SenterNovem research grant 15044112.

The printing of this thesis was financially supported by:



Anna
Fonds

Steunt orthopedische research

Printed by: WÖHRMANN PRINT SERVICE, Zutphen, Nederland.

Cover Art by: Clara Hermoso and Gustavo A. Higuera, 3DF PEOT/PBT scaffolds seeded with human mesenchymal stem cells and stained with methylene blue.

3D TISSUE FORMATION THE KINETICS OF HUMAN MESENCHYMAL STEM CELLS

DISSERTATION

to obtain
the degree of doctor at the University of Twente,
on the authority of the rector magnificus,
prof. dr. H. Brinksma,
on account of the decision of the graduation committee,
to be publicly defended
on Friday 3rd of September, 2010 at 15.00

by
Gustavo Andrés Higuera Sierra

born on January 25th, 1979
in Tunja, Colombia

Promoter: prof. dr. Clemens A. van Blitterswijk

Assistant Promoter: dr. ir. Anton van Boxtel

Copyright: 2010, Gustavo A. Higuera, Enschede, The Netherlands.

Neither this book nor its parts may be reproduced without prior consent from the author.

ISBN: 978-90-365-3065-1

Niets is, alles wordt.

Heraclitus

A mis abuelos

Table of Contents

Preface	9
Introduction: The Physics of Tissue Formation With Mesenchymal Stem Cells.	11
I. 2D Kinetics of hMSCs	33
Chapter 1: Quantifying <i>in vitro</i> Growth and Metabolism Kinetics of Human Mesenchymal Stem Cells Using a Mathematical Model	35
Chapter 2: Patterns of Amino Acid Metabolism by Proliferating Human Mesenchymal Stem Cells	59
II. 3D Kinetics of hMSCs	83
Chapter 3: Darcian permeability constant as indicator for shear stresses in regular scaffold systems for tissue engineering	85
Chapter 4: Concentration Gradients Correlate With Three-dimensional Proliferation and Migration Patterns of Human Mesenchymal Stem cells	105
III. From Kinetics to Application	135
Chapter 5: High-throughput in 3D: Cell and Tissue Screening <i>in vitro</i> and <i>in vivo</i>	137
General Discussion	157

Summary	165
Samenvatting	167
Resumen	170
Acknowledgements	173
List of Publications	176
Curriculum Vitae	177

Preface

The main thesis of this book proposes that physical phenomena underlies the formation of 3D tissue. To show this, we investigated stem cell proliferation under diffusive mass transport and shear stress. In our quest to engineer musculoskeletal tissues with mesenchymal stem cells (MSCs), the introduction reviews the known responses by MSCs to physical phenomena. Since our goal is to engineer human musculoskeletal tissues, human mesenchymal stem cells (hMSCs) are at the center of four out of five experimental chapters. Chapter 1 explores whether hMSCs kinetics are consistent at different seeding densities. Chapter 2 proposes that hMSCs proliferation in 2D and bioreactor culture have patterns of amino acid metabolism. Chapter 3 studies shear stress inside 3D scaffolds with interconnected and defined pore architecture. Chapter 4 shows that there is a correlation between concentration gradients and hMSCs proliferation and migration patterns in 3D scaffolds. The monolayer (Chapter 1 and 2) to 3D organization (Chapter 3, 4 and 5) of hMSCs lead to Chapter 5. In this chapter, a 3D well for hMSCs culture is created and developed into an *in vivo* high-throughput screening system. Finally, the discussion explains how the findings in each chapter contribute to the engineering of musculoskeletal tissues.

Introduction

The Physics of Tissue Formation With Mesenchymal Stem Cells

Gustavo A. Higuera¹, Lorenzo Moroni¹, Anton van Boxtel², and Clemens A. van Blitterswijk¹

¹Department of Tissue Regeneration, Institute for Biomedical Technology, University of Twente, Enschede, The Netherlands.

²Systems and Control Group, Wageningen University, Wageningen, The Netherlands.

Developing and adult tissues display the exquisite combination of physical, chemical and biological processes [1]. Clinicians have successfully regenerated, replaced or induced [2, 3] tissue formation with limited knowledge of the processes that make functional tissue possible. To be able to develop more treatments for regenerating complex tissues and treating diseases, the physical principles that govern tissue formation and maintenance need attention.

Out of the many tissues that are currently actively studied, musculoskeletal tissues and their cells have inspired some of the best examples on how physics can induce cells to form and maintain tissue [4, 5]. Because of their potential as cell sources in treatments of musculoskeletal tissues diseases and traumas, mesenchymal stem cells (MSCs) have been the focus of many studies that aim to understand their biology and harness their therapeutical potential in a controlled manner [6-8]. To be able to exploit this potential, the physical phenomena that underlies the MSCs therapeutic role needs to be considered and better understood to create successful medical treatments. In this review, we enumerate the physical forces that stimulate MSC biology in the direction of tissue formation and maintenance. Furthermore, we offer an outlook on how physical forces can support the regeneration of musculoskeletal tissues *in vitro*.

The structure of the review is based on MSCs responses to physical forces from the macroscopic to the molecular level. The fluid statics, fluid dynamics, and surface physics phenomena involved in MSCs regulation will be discussed. Furthermore, mechanotransduction and kinetics will be also introduced as critical elements in understanding cell activity. The choice for focusing on MSCs is due to the growing body of literature showing that MSCs are sensitive to many physical forces. This has inspired the use of conventional and unconventional techniques [9-11] such as,

nanotechnology and mathematical modeling, to understand how physical phenomena stimulates MSCs.

Fluid Statics

Fluid statics is the study of fluids at rest. The effect on MSCs of physical phenomena in this category include hydrostatic pressure and diffusive mass transport.

Hydrostatic pressure

Hydrostatic pressure (HP) refers to the pressure that a body of fluid exerts on a surface depending on gravity (g), density (ρ) and height (h), $HP = \rho gh$, assuming the fluid is incompressible. In the study of HP on MSCs differentiation, HP refers to the fluid's pressure change by an external force in a closed geometry (Fig. 1). The external force (ΔP_{ex}), which can be that exerted by compression (Fig. 1A), tension (Fig. 1B) or ultrasound (Fig. 1C), increases $HP = \Delta P_{ex} + \rho gh$. The term ρgh is negligible because it increases HP by about 100 pascal per centimeter of height. Thus, external stimulation is the main cause of pressure changes.

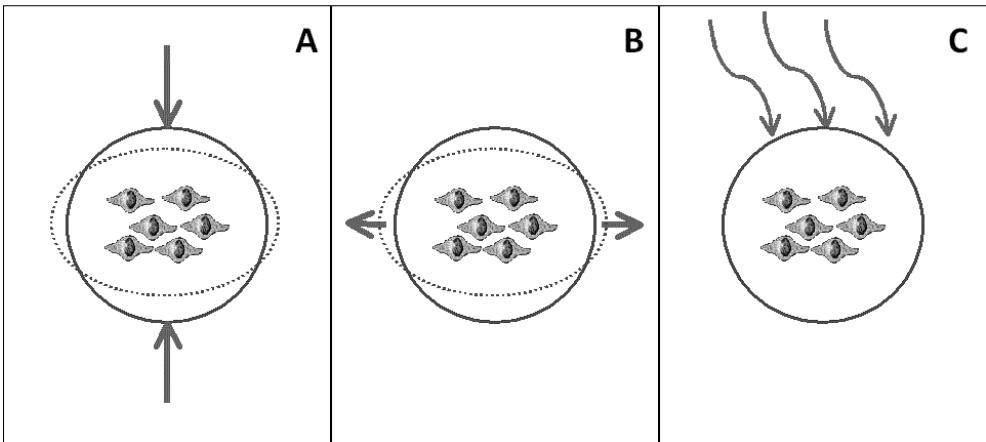


Figure 1 A sphere containing MSCs under, **A**: Compression. **B**: Tension **C**: Ultrasound.

A range of loads determine MSCs chondrogenic or osteogenic differentiation as highlighted by Gurkan and Akkus (2008) [4]. In osteogenesis, physiological loadings in the range of $7 \times 10^3 - 2.7 \times 10^4$ Pa have an osteogenic effect [5, 12-16], whereas in chondrogenesis, physiological loadings in the range of $1 \times 10^5 - 1 \times 10^8$ Pa have a chondrogenic effect [17-21]. So that, higher HP stimulate chondrogenesis and lower HP stimulate osteogenesis. In addition, intermittent or cyclic loading is more effective in chondrogenesis than static loading [19, 20].

Ultrasound also induces changes in hydrostatic pressure (Fig. 1). Per definition, ultrasound is a cyclic pressure induced by sound waves at high frequencies (above 20 KHz). Pressure applied in this manner increases the yield of MSCs from the human umbilical cord [22] and induce osteogenic [23], and chondrogenic [24-27] differentiation of MSCs at intensities between 30 to 200 mW/cm². In general terms, low intensities induce osteogenic differentiation and high intensities induce chondrogenic differentiation. It must be noted that the intensity threshold for osteogenic and chondrogenic differentiation is not yet clearly defined because ultrasound also depends on the frequency, which varies in the induction of osteogenesis with respect to chondrogenesis studies.

Although for a complete pressure-ultrasound relationship, the volume and frequency need to be considered; it seems that these intensities can induce MSCs chondrogenic differentiation in the same manner as loadings between 1×10^5 - 1×10^8 Pa. The HP changes by compression or tension require physical contact with the stimulated body whereas ultrasound does not (Fig. 1C). Thus, sound waves may induce HP more homogeneously than compression or tension enhancing MSCs viability and preventing MSCs death [25].

HP induces MSC differentiation depending on at least three factors, as a force transfers from the macroscopic to the molecular level (Fig. 1). First, the geometry of a construct determines the distribution of forces and the amount of pressure each MSCs experiences, and hence the type of differentiation. For example, forces applied on meniscus-like structures yield cartilage [28, 29]; on elongated structures results in tendon substitutes [30], or in cell death [31]. Second, viscosity changes the HP with a specific differentiation effect on MSCs [32-34]. Third, HP induces changes of morphology in MSCs [35], which depend on the viscoelastic properties of MSCs populations [36]. There is one important unifying characteristic to consider with respect to the three factors described: How HP transfers in a solid differs from how it would transfer in a liquid. Thus, two situations arise: In a liquid (less viscous) environment, compression induces localized deformation, where only some cells in a construct sense the HP changes (Fig. 2). In a solid (more viscous) environment, all cells in the geometry sense the changes in HP and adjust to it (Fig. 3). Consequently, how HP distributes inside a geometry may largely depend on the internal stiffness of cell-cell interactions with extracellular components.

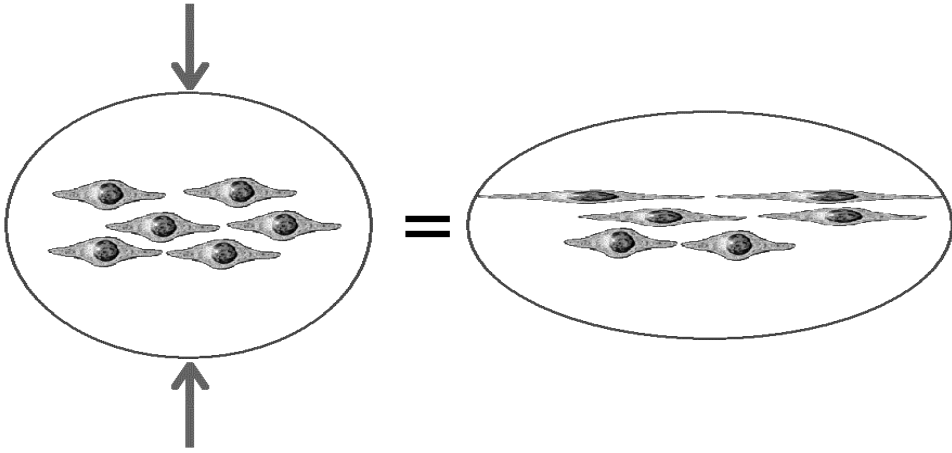


Figure 2 Liquid or soft ECM environment surrounding hMSCs under compression. Note only some MSCs sense the change of shape of the sphere.

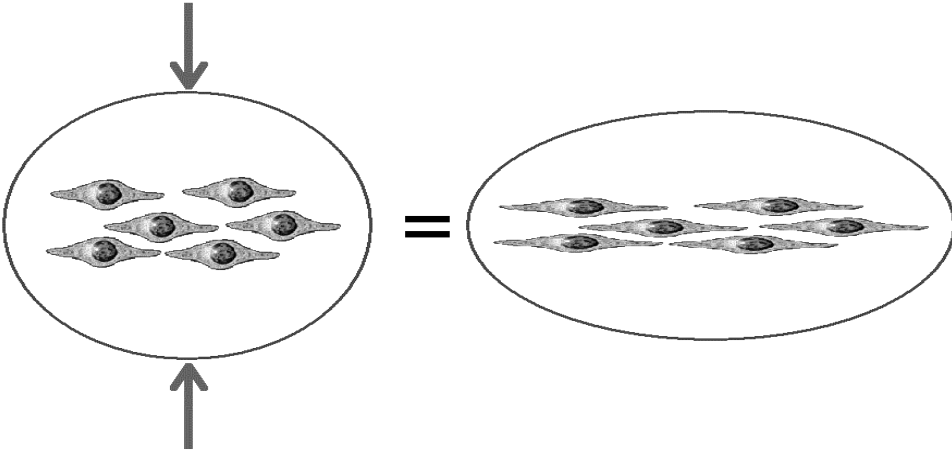


Figure 3 Solid or hard ECM environment surrounding hMSCs under compression. Note all MSCs sense the change of shape of the sphere.

Elucidating the HP distribution in complex 3D structures will further unravel the geometrical function [37] of musculoskeletal tissues *in-vivo*. Particularly, how MSCs and ECM change to HP changes will be essential. Significant steps in this direction may be first taken in micro-fluidic devices, where the HP can be controlled with little variation over small distances [38]. Then, tissue changes to HP may be elucidated from HP distribution and cell-ECM interactions.

Diffusive Mass Transport

Diffusive mass transport occurs when a molecule's concentration varies at different locations, creating a chemical potential. Diffusive mass transport is important

all throughout musculoskeletal tissues, particularly in the regions away from blood vessels. In those cases, the chemical potential becomes a driving force for mass transport from regions of higher to regions of lower molecular concentrations. According to Fick's first law [39], the mass transport can be defined by a flow rate (j) of a molecule equal to $j = \rho \cdot D \cdot dw/dy$, where (ρ) is the density of the tissue/medium, (D) is the diffusivity of the molecule in that tissue/medium, and the term (dw/dy) represents the mass fraction (w) change of a molecule in a distance (y). The term dw/dy is the driving force of (j) and the mathematical interpretation of concentration gradients (Fig. 4). Musculoskeletal tissues evolved blood vessels at defined distances to assist diffusive mass transport in maintaining viable MSCs.

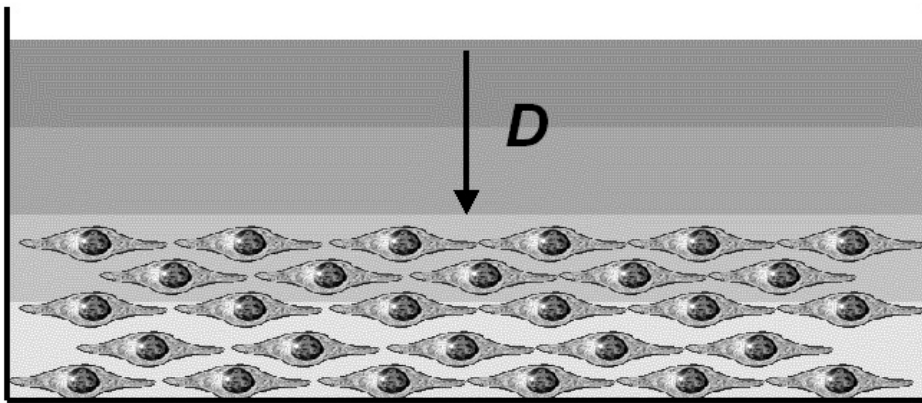


Figure 4 Cross section of MSCs multilayer static culture. Diffusive mass transport maintains a flux of molecules to the cells (Diffusion constant). Gradients are formed across the MSCs layers.

MSCs are highly sensitive to concentrations, which stimulate differentiation [40, 41], homing [42, 43], angiogenesis [44], or death [45]. MSCs always need a group of molecules to survive, thus dw/dy may never be equal to zero in their natural environment for a required molecule. Consequently, diffusive mass transport is always present. The profiles or steepness of the gradients are variable. The profile of concentration gradients is dependent on the diffusion constant (D) and kinetics of MSCs for a particular molecule. Therefore, concentration-gradient profiles must be controlled [46] to be able to determine the potential responses by MSCs. Diffusive mass transport can help unravel the biophysical nature of transport of molecules, such as trophic factors [47], which stimulate the formation and maintenance of musculoskeletal tissues.

Fluid Dynamics

Fluid dynamics is the study of fluids in motion by convection. This improves the supply of molecules to MSCs. But also, it causes shear stress.

Shear stress

Shear stress is defined as the stress (T) caused by a force in a direction parallel or tangential to a surface $T=F/A$, where (F) is force, and (A) is the area of contact of F . In MSCs culture, the force on cells is caused by fluid flow around cells (Fig. 5). Shear stress stimulates MSCs proliferation and differentiation [48-52] with oscillatory flow increasing the proliferation rates of MSCs [50]. As determined by Zhao et al. [53], a shear stress of 1.2×10^{-4} Pa resulted in 1.4 times higher proliferation rate, higher CFU-F formation, and more fibronectin and heat shock protein HSP-47 secretion. On the other hand, a shear stress of 1×10^{-5} Pa upregulated the osteogenic differentiation potential of MSCs.

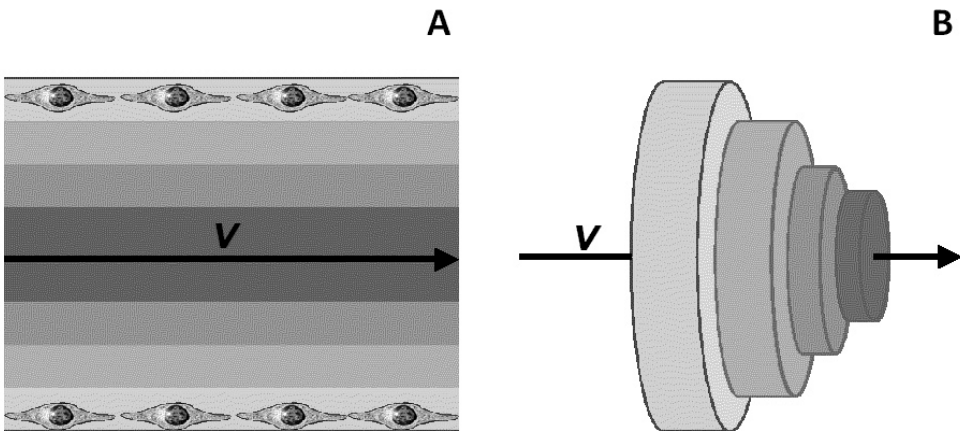


Figure 5 Shear stress in a cylindrical pore (e.g. a blood vessel) under laminar flow. **A:** Fluid velocity (V) changes radially across the cylindrical pore. MSCs experience the fluid velocities closer to them and thereby shear stress. **B:** In the cylindrical pore, molecular concentrations decrease through the length of the cylinder. Thus gradients are longitudinal in the presence of fluid flow.

Shear stress orients the organization of tissue. For example, bone rods can form perpendicular to a surface under turbulent fluid dynamics with eddies of $250 \mu\text{m}$ [54]. In addition, shear stress (5×10^{-3} Pa) can also form bone rods parallel to the fluid flow direction in perfusion bioreactors [54]. Thus, shear stress has also structural implications in tissue formation with MSCs. The 3D structure as well as the fluid flow rate [55] determine the flow streamlines in different bioreactor configurations. Thus, bone rods determine the response of MSCs to eddies and flow [56]. To control shear

stress, different configurations have been designed to maintain a homogenous environment and a consistent effect on MSCs [57-59]. As a result, genes significantly expressed in response to shear stress (0.1 - 1 Pa) and its duration (10 min, 1 and 24 h) were identified [60]. In addition, combined shear stress and cyclic flexure have also dramatically accelerated tissue formation with MSCs within engineered heart valves [61].

The shear stress effect on MSCs to engineer cartilage, bone and ligament was summarized by Vunjak-Novakovic et al. [62] as follows: For cartilage, dynamic laminar flow patterns are better than either static (no flow) or turbulent steady flow. For bone, flow induces changes in the geometry, distribution, and orientation of bone-like trabeculae. For ligament, combining dynamic stretch and torsion improves cell differentiation, alignment and functional assembly.

The response of MSCs to shear stress shows that replacing the vascular system *in vitro* helps the formation of musculoskeletal tissues, but cannot replace the maintenance and control role of the vascular system. The role of shear stress in MSCs biology has laid a strong foundation to use novel systems [63, 64] combined with mathematical modeling [59, 65, 66] to be able to address questions, under fluid dynamics, about the effect on MSCs of gradients, cell communication, and ECM development.

Surface Physics

Surface physics studies the physical changes that alter the bio-chemical interactions at interfaces. Physical changes cause changes to a surface's chemistry. Since MSCs in culture require an attachment surface, the need for substrates has produced a broad range of materials that can influence MSCs proliferation and differentiation. Through the use of methods that modify the nano-structure and micro-structure of materials [67-69], MSCs response to surface physics lies in the surfaces' chemistry and disorder (Fig. 6).

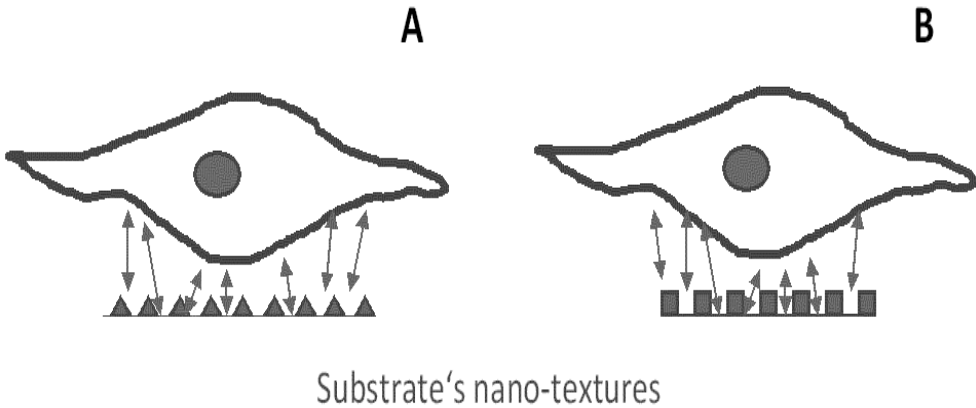


Figure 6 Substrates nano-textures interact with MSCs membrane proteins to differentiate MSCs. Triangular (A) and (B) square modifications represent the fact that MSCs response to surfaces is highly specific.

Surface chemistry

Surface chemistry involves the interaction of cells with a surface through hydrogen and/or covalent bonds. Due to the nature of the methods used to physically change surfaces, surface modification affects the number and type of bonds possible. Thus, making a surface's chemistry and its physics intertwined. A comparison of nano and micro-sized surface modifications of the same material showed that MSCs on nano-textured surfaces showed higher osteogenic differentiation than on micro-textured surfaces [69]. This suggested that it is necessary to explore the MSCs proteins, such as focal adhesions (membrane protein complexes) to explore the effect of surface modifications on MSC differentiation.

For the past 150 years, chemists and physicists have dealt with the nature of how different elements of the periodic table interact with each other to change and maintain a protein's conformation through bonds. Altering bonds and elements of a surface have maintained or promoted MSCs proliferation and differentiation [67]. Cytoskeleton rearrangements during differentiation suggest that focal adhesions play a major role in this process of lineage commitment [10, 70-73]. How the signal is transduced from surface modifications to the gene expression level to establish the lineage commitment can be deduced with the structural components of this process, which include at least focal adhesions, proteins RhoA and ROCK, the actin-myosin cytoskeleton, MAP kinase, and Wnt signaling associated transcripts [10, 70-73]. It is possible that quantities of a component might determine one lineage over another. For example, the number of focal adhesions induced by a surface could determine the differentiation lineage of MSCs.

Disorder

Musculoskeletal tissues are organized 3D structures, where organization of cells is characteristic for each tissue. A fundamental aspect of this organization has been discovered through surface physics by showing that the degree of order on surfaces [74] can provide the optimal conditions for stimulating MSCs to form bone cells [75]. The implication of this is that there are degrees of order and disorder achieved by nature, which support tissue functioning and some that do not. Disorder and tissue organization can inspire new stimuli for MSCs differentiation. The degree of disorder translates into distances between cells that determine the structure of extracellular matrix and affect transport phenomena and cell communication.

The study of physical forces at the molecular level in MSCs has produced important advances in two areas: mechanotransduction and kinetics. These are affected by, surface physics, fluid statics or dynamics to induce changes in MSCs during formation and maintenance of musculoskeletal tissues. Mechanotransduction and kinetics can influence each other. How that can occur is not clear because these have been studied in different research contexts.

Mechanotransduction

Physical forces induce a cascade of molecular, biochemical, and physical changes that result in proliferation or differentiation of MSCs. The study of how physical phenomena affects cells is called mechanotransduction and has been studied in MSCs with respect to its shape.

Cell shape

Each MSC is basically a 3D structure. Determining its linear dimensions, such as the height [76] can help us determine how forces inside the cell (Fig. 7) cause it to live, die [77] or differentiate. For example, a disc-like shape of MSCs has been correlated with maintaining a healthy intervertebral disc [78]. To be able to understand how MSCs control their shape, the structural components in the cytoskeleton have been determined [10, 71, 73, 79]. Among them, tension and proteins such as RhoA, myosin, and actin can initiate the stem cell lineage commitment. The cytoskeleton dynamics are so powerful that these can alone make MSCs into mature bone cells [79]. Upon cytoskeleton disruption, forces inside MSCs change and determine MSCs fate [10, 73]. Using the correct cytoskeletal components and in their right amounts is essential to control MSCs shape and fate because MSCs can buffer even the strongest of tension fluctuations [72].

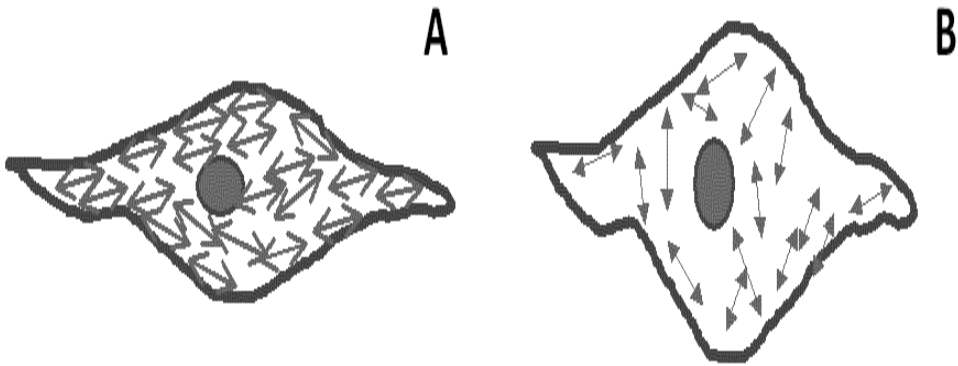


Figure 7 A-B: Cell shape causes variation in the force balance of the cytoskeleton inside MSCs. These changes modulate MSCs tissue differentiation.

Mechanotransduction is establishing the components necessary to robustly initiate and maintain tissues. In addition, new theories on cell mechanosensing are opening new possibilities to control and induce cell and tissue organization [80]. Thus, it is necessary to apply mechanotransduction theory and concepts to 3D MSCs culture under the presence of controlled fluid statics or dynamics. For example, the combination of theoretical tension fields [81] with experimentally measured forces [82, 83] can unravel the rigidity of 3D [84, 85] environments inducing MSCs differentiation. This rigidity can be tested against assumptions made in tensegrity [80] to define force balances for cells and ECM within tissues. In this manner, it would be possible to determine the physical cues and molecular components necessary to understand how musculoskeletal tissues work at the cellular level.

Kinetics

Kinetics refers to the movement of mass by the law of conservation of mass, which states that mass is not created nor destroyed. This means that in a closed volume, any molecule that enters will either stay in, go out or be converted into some other molecule. In kinetic studies, any molecule (m) whose molar concentration changes in time (dC_m/dt) is defined by the following equation, $dC_m/dt = Cin_m - Cout_m + Rx_A - Rx_B$, where Cin_m and $Cout_m$ describe the molar concentration of m going into and out of the volume, respectively. $RxnA_m$ and $RxnB_m$ describe the conversion of molecules by MSCs (Fig. 8). The signs in the reactions denote whether m is consumed or produced by MSCs. In addition, conversion of molecules can occur through spontaneous reactions that must be identified to make accurate estimates and predictions.

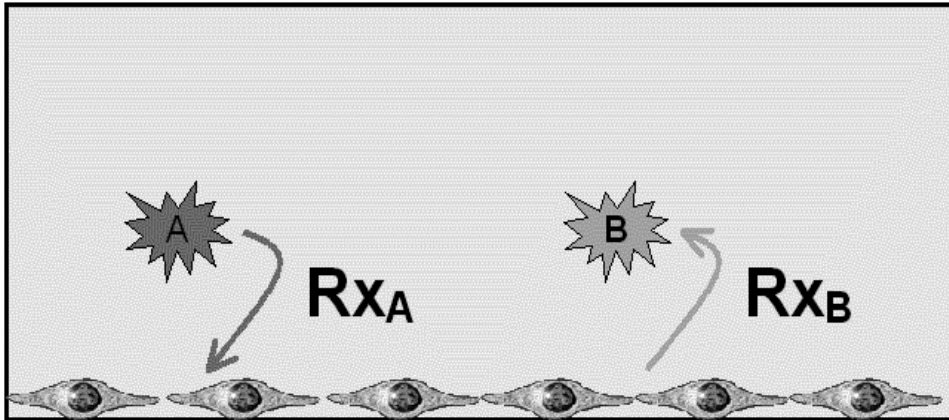


Figure 8 Mass balance of molecule m in volume. $C_{in,m}$ and $C_{out,m}$ are equal to zero. Concentration changes of m are only caused by reaction rates Rx_A and Rx_B .

Proliferation Kinetics:

Kinetics have been used to describe MSCs proliferation due to the need to expand them. This has produced several studies regarding the kinetics of MSCs proliferation on tissue culture plastic [86, 87] and bioreactors [53, 59, 88, 89]. So far, studies have dealt with the kinetic effect on MSCs of seeding densities [86, 87], the 3D microenvironment [59, 88, 89], and shear stress [53]. The main contribution of kinetics to MSCs biology have been to quantify proliferation and describe it in parameters that can lay the foundation to control, understand, and optimize research and industrial uses of MSCs. Thus, MSCs proliferation and differentiation have been described according to proliferation rates or growth rates and production or consumption of essential molecules, such as extra cellular matrix [88], alkaline phosphatase [40, 53], calcium [53], oxygen [59], glucose, lactate, ammonia, glutamine and glutamate [45, 87, 89]. This approach to control cell cultures has been successfully performed with vaccine and food production after identifying major pathways and components involved in a biological process. In the case of MSCs, the list of components required for any biological process is arguably larger because MSCs proliferation and differentiation are inherently more complex. However, systematic analysis of small sets of reactions can develop into quantitative description of pathways and complex processes. In this manner, kinetics can continue to identify the amounts and optimal conditions for initiating regeneration or maintaining function of musculoskeletal tissues.

Future perspective

MSCs response to physical phenomena can stimulate the development of medical treatments. For example, instead of homogeneously seeding MSCs all throughout a scaffold to regenerate tissue, MSCs could be concentrated along with their trophic effects [47] in strategic locations in scaffolds. This could benefit tissue regeneration of live tissue in three ways: (i) reduce the number of MSCs and thus the need for expansion; (ii) stimulate extensive implanted cell-host cell contact in desired regions around the scaffold; (iii) prevent MSCs exposure to nutrient limitation *in vivo* after *in vitro* culture. In this approach, for therapeutic effects to occur in realistic time spans, the diffusive mass transport and kinetics of biological factors need to be determined. Imaging techniques [90-94] can contribute to monitoring of trophic factors and the *in vivo* behaviour of stem cells.

Furthermore, in a bottom-up approach to regenerate tissue with MSCs, each phase of tissue regeneration could be established according to physical phenomena. First, the surface physics are defined for a specific MSCs lineage. Then, fluid statics and dynamics that support 3D organization of MSCs in a lineage are introduced. So that, physical phenomena combined in timed stages of regeneration can provide the most stable and efficient conditions for stimulating the robust creation of a tissue. Mechanotransduction and kinetics provide the fundamental knowledge required to screen conditions and stimulators of mechanosensitive pathways in MSCs [81, 95, 96]. As an example, bone relies heavily on the vascular system [4]. Thus, angiogenesis could benefit from shear stress studies. A number of studies in this review show that physical phenomena change the shape and organization of MSCs resulting in functional [97] differentiated MSCs. The shear stress regimes can define the conditions for vascularization of mm-size bone constructs in bioreactors. This means integrating shear stress data with biological cues to harness the vascularization properties of MSCs.

Many studies have indicated that physical phenomena significantly determines the biological response of MSCs [4]. As it has been shown in this review, the response of MSCs to physical phenomena has been largely studied *in vitro*. This is due to the difficulty to performing controlled experiments *in vivo*. On-line monitoring [98] of tissue biology in animal experiments [99] could provide some of the fundamental principles necessary to recreate natural tissue in 3D *in vitro* models. Mimicking physical and biochemical conditions *in vitro* to test MSCs (and other cells) responses lays the foundations for successful application of MSCs in medical treatments [100, 101]. High throughput screening (HTS) has also contributed to finding the fundamental aspects of tissue biology [102-104]. The disadvantage here is that *in vitro* HTS screening can be biased with respect to the true conditions that regenerate tissue *in vivo*. Thereby, producing false positives. A possibility to avoid false

positives would be to create an *in vivo* HTS. This would create a top-down approach to regenerate tissue, where biomaterials could be processed to create a controlled environment for screening multiple conditions in animal models. In this manner, fundamental principles of tissue regeneration could be identified to acquire basic knowledge and medical treatments that would significantly accelerate the progress of medicine.

References

1. Forgács, G. and S. Newman, *Biological physics of the developing embryo*. 2005, Cambridge: Cambridge University Press. vi, 337 p.
2. Atala, A., *Tissue-engineered autologous bladders for patients needing cytoplasty*. *Lancet*, 2006. **367**(9518): p. 1241 - 1246.
3. Macchiarini, P., et al., *Clinical transplantation of a tissue-engineered airway*. *Lancet*, 2008. **372**(9655): p. 2023 - 2030.
4. Gurkan, U.A. and O. Akkus, *The mechanical environment of bone marrow: a review*. *Ann Biomed Eng*, 2008. **36**(12): p. 1978-91.
5. Rubin, J., C. Rubin, and C.R. Jacobs, *Molecular pathways mediating mechanical signaling in bone*. *Gene*, 2006. **367**: p. 1-16.
6. Caplan, A., *Why are MSCs therapeutic? New data: new insight*. *Journal of Pathology*, 2009. **217**(2): p. 318-324.
7. Caplan, A.I. and S.P. Bruder, *Mesenchymal stem cells: Building blocks for molecular medicine in the 21st century*. *Trends in molecular medicine*., 2001. **7**(6): p. 259 - 264.
8. Meirelles, L.d.S., et al., *Mechanisms involved in the therapeutic properties of mesenchymal stem cells*. *Cytokine and Growth Factor reviews*, 2009. **20**(5): p. 419 - 427.
9. Nelson, C.M. and C.S. Chen, *Cell-cell signaling by direct contact increases cell proliferation via a PI3K-dependent signal*. *Febs Letters*, 2002. **514**(2-3): p. 238-242.
10. McBeath, R., et al., *Cell shape, cytoskeletal tension, and RhoA regulate stem cell lineage commitment*. *Developmental Cell*, 2004. **6**(4): p. 483-495.
11. Byrne, D.P., et al., *Simulation of tissue differentiation in a scaffold as a function of porosity, Young's modulus and dissolution rate: application of mechanobiological models in tissue engineering*. *Biomaterials*, 2007. **28**(36): p. 5544-54.
12. Bryant, J.D., *The Effect of Impact on the Marrow Pressure of Long Bones Invitro*. *Journal of Biomechanics*, 1983. **16**(8): p. 659-&.
13. Downey, D.J., P.A. Simkin, and R. Taggart, *The Effect of Compressive Loading on Intraosseous Pressure in the Femoral-Head Invitro*. *Journal of Bone and Joint Surgery-American Volume*, 1988. **70A**(6): p. 871-877.
14. Kumar, S., P.R. Davis, and B. Pickles, *Bone-Marrow Pressure and Bone Strength*. *Acta Orthopaedica Scandinavica*, 1979. **50**(5): p. 507-512.
15. Robling, A.G., A.B. Castillo, and C.H. Turner, *Biomechanical and molecular regu-*

- lation of bone remodeling. Annual Review of Biomedical Engineering, 2006. **8**: p. 455-498.
16. Turner, C.H., V. Anne, and R.M.V. Pidaparti, *A uniform strain criterion for trabecular bone adaptation: Do continuum-level strain gradients drive adaptation?* Journal of Biomechanics, 1997. **30**(6): p. 555-563.
 17. Angele, P., et al., *Cyclic, mechanical compression enhances chondrogenesis of mesenchymal progenitor cells in tissue engineering scaffolds.* Biorheology, 2004. **41**(3-4): p. 335-346.
 18. Angele, P., et al., *Cyclic hydrostatic pressure enhances the chondrogenic phenotype of human mesenchymal progenitor cells differentiated in vitro.* Journal of Orthopaedic Research, 2003. **21**(3): p. 451-457.
 19. Miyanishi, K., et al., *Dose- and time-dependent effects of cyclic hydrostatic pressure on transforming growth factor-beta 3-induced chondrogenesis by adult human mesenchymal stem cells in vitro.* Tissue Engineering, 2006. **12**(8): p. 2253-2262.
 20. Miyanishi, K., et al., *Effects of hydrostatic pressure and transforming growth factor-beta 3 on adult human mesenchymal stem cell chondrogenesis in vitro.* Tissue Engineering, 2006. **12**(6): p. 1419-1428.
 21. Schumann, D., et al., *Mechanobiological conditioning of stem cells for cartilage tissue engineering.* Bio-Medical Materials and Engineering, 2006. **16**(4): p. S37-S52.
 22. Yoon, J.H., et al., *Introducing pulsed low-intensity ultrasound to culturing human umbilical cord-derived mesenchymal stem cells.* Biotechnol Lett, 2009. **31**(3): p. 329-35.
 23. Moignes, J.J., et al., *Ultrasound accelerated bone tissue engineering monitored with magnetic resonance microscopy.* Conf Proc IEEE Eng Med Biol Soc, 2006. **1**: p. 484-8.
 24. Ebisawa, K., et al., *Ultrasound enhances transforming growth factor beta-mediated chondrocyte differentiation of human mesenchymal stem cells.* Tissue Eng, 2004. **10**(5-6): p. 921-9.
 25. Lee, H.J., et al., *Low-intensity ultrasound inhibits apoptosis and enhances viability of human mesenchymal stem cells in three-dimensional alginate culture during chondrogenic differentiation.* Tissue Eng, 2007. **13**(5): p. 1049-57.
 26. Lee, H.J., et al., *Low-intensity ultrasound stimulation enhances chondrogenic differentiation in alginate culture of mesenchymal stem cells.* Artif Organs, 2006. **30**(9): p. 707-15.
 27. Schumann, D., et al., *Treatment of human mesenchymal stem cells with pulsed low*

- intensity ultrasound enhances the chondrogenic phenotype in vitro*. *Biorheology*, 2006. **43**(3-4): p. 431-43.
28. Yamasaki, T., et al., *Meniscal regeneration using tissue engineering with a scaffold derived from a rat meniscus and mesenchymal stromal cells derived from rat bone marrow*. *J Biomed Mater Res A*, 2005. **75**(1): p. 23-30.
29. Yamasaki, T., et al., *Transplantation of meniscus regenerated by tissue engineering with a scaffold derived from a rat meniscus and mesenchymal stromal cells derived from rat bone marrow*. *Artif Organs*, 2008. **32**(7): p. 517-524.
30. Kall, S., et al., *In vitro fabrication of tendon substitutes using human mesenchymal stem cells and a collagen type I gel*. *Handchir Mikrochir Plast Chir*, 2004. **36**(4): p. 205-11.
31. Kearney, E.M., P.J. Prendergast, and V.A. Campbell, *Mechanisms of Strain-Mediated Mesenchymal Stem Cell Apoptosis*. *Journal of Biomechanical Engineering-Transactions of the Asme*, 2008. **130**(6): p. 61004.
32. Pek, Y.S., et al., *A thixotropic nanocomposite gel for three-dimensional cell culture*. *Nat Nanotechnol*, 2008. **3**(11): p. 671-5.
33. Terraciano, V., et al., *Differential response of adult and embryonic mesenchymal progenitor cells to mechanical compression in hydrogels*. *Stem Cells*, 2007. **25**(11): p. 2730-8.
34. Yow, S.Z., et al., *Collagen-based fibrous scaffold for spatial organization of encapsulated and seeded human mesenchymal stem cells*. *Biomaterials*, 2009. **30**(6): p. 1133-42.
35. Eggum, T.J. and C.J. Hunter, *Development and Validation of a System for the Growth of Cells and Tissues Under Intermittent Hydrostatic Pressure*. *Journal of Biomechanical Engineering-Transactions of the Asme*, 2008. **130**(6): p. -.
36. Ofek, G., et al., *Mechanical Characterization of Differentiated Human Embryonic Stem Cells*. *Journal of Biomechanical Engineering-Transactions of the Asme*, 2009. **131**(6): p. -.
37. Thompson, D.A.W. and J.T. Bonner, *On growth and form*. an abridged edition. / edited by John Tyler Bonner. ed. 1971, [S.l.]: Cambridge University Press.
38. Sim, W.Y., et al., *A pneumatic micro cell chip for the differentiation of human mesenchymal stem cells under mechanical stimulation*. *Lab Chip*, 2007. **7**(12): p. 1775-82.
39. Bird, R.B., W.E. Stewart, and E.N. Lightfoot, *Transport phenomena*. 2nd rev. ed. ed. 2007, New York ; Chichester: J. Wiley. xii, 905 p.
40. Grayson, W.L., et al., *Effects of hypoxia on human mesenchymal stem cell expansion*

- sion and plasticity in 3D constructs*. Journal of Cellular Physiology, 2006. **207**(2): p. 331-339.
41. Pan, H.C., et al., *Human amniotic fluid mesenchymal stem cells in combination with hyperbaric oxygen augment peripheral nerve regeneration*. Neurochem Res, 2009. **34**(7): p. 1304-16.
 42. Potapova, I.A., I.S. Cohen, and S.V. Doronin, *Apoptotic endothelial cells demonstrate increased adhesiveness for human mesenchymal stem cells*. J Cell Physiol, 2009. **219**(1): p. 23-30.
 43. Potapova, I.A., et al., *Culturing of human mesenchymal stem cells as three-dimensional aggregates induces functional expression of CXCR4 that regulates adhesion to endothelial cells*. J Biol Chem, 2008. **283**(19): p. 13100-7.
 44. Potapova, I.A., et al., *Mesenchymal stem cells support migration, extracellular matrix invasion, proliferation, and survival of endothelial cells in vitro*. Stem Cells, 2007. **25**(7): p. 1761-8.
 45. Schop, D., et al., *Growth, Metabolism and Growth Inhibitors of Mesenchymal Stem Cells*. Tissue Engineering: Part A, 2009. **15**.
 46. Singh, M., C. Berkland, and M.S. Detamore, *Strategies and Applications for Incorporating Physical and Chemical Signal Gradients in Tissue Engineering*. Tissue Engineering Part B-Reviews, 2008. **14**(4): p. 341-366.
 47. Caplan, A. and J. Dennis, *Mesenchymal stem cells as trophic mediators*. J Cell Biochem, 2006(98): p. 1076.
 48. Braccini, A., et al., *Three-dimensional perfusion culture of human bone marrow cells and generation of osteoinductive grafts*. Stem Cells, 2005. **23**(8): p. 1066-1072.
 49. Chen, X., et al., *Bioreactor expansion of human adult bone marrow-derived mesenchymal stem cells*. Stem Cells, 2006. **24**(9): p. 2052-2059.
 50. Li, Y.J., et al., *Oscillatory fluid flow affects human marrow stromal cell proliferation and differentiation*. Journal of Orthopaedic Research, 2004. **22**(6): p. 1283-1289.
 51. Nagatomi, J., et al., *Effects of cyclic pressure on bone marrow cell cultures*. Journal of Biomechanical Engineering-Transactions of the Asme, 2002. **124**(3): p. 308-314.
 52. Sikavitsas, V.I., et al., *Flow perfusion enhances the calcified matrix deposition of marrow stromal cells in biodegradable nonwoven fiber mesh scaffolds*. Annals of Biomedical Engineering, 2005. **33**(1): p. 63-70.
 53. Zhao, F., R. Chella, and T. Ma, *Effects of shear stress on 3-D human mesenchymal*

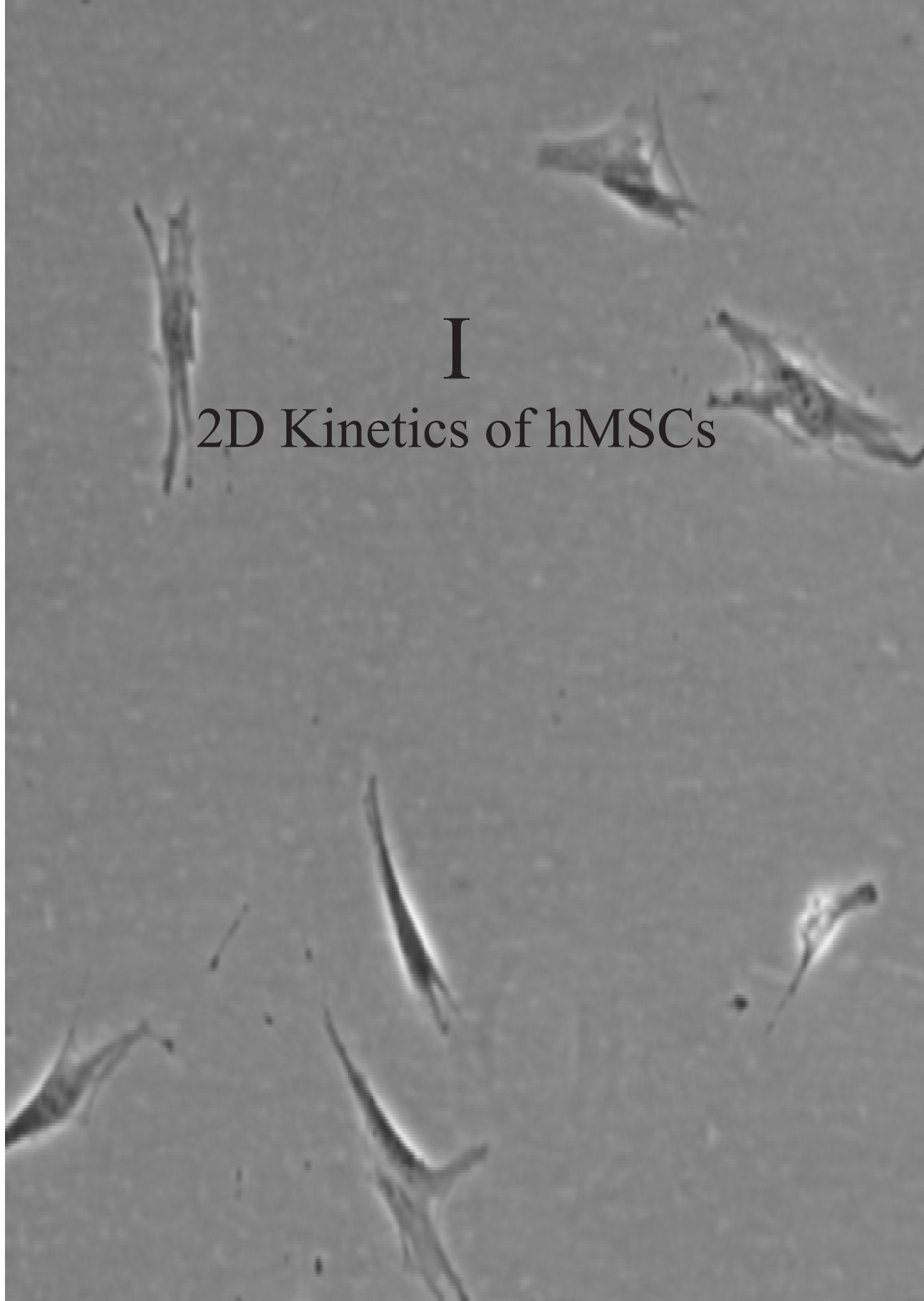
- stem cell construct development in a perfusion bioreactor system: Experiments and hydrodynamic modeling.* Biotechnol Bioeng, 2007. **96**(3): p. 584-95.
54. Meinel, L., et al., *Bone tissue engineering using human mesenchymal stem cells: effects of scaffold material and medium flow.* Ann Biomed Eng, 2004. **32**(1): p. 112-22.
55. Shanglong, X., et al., *Cell distribution in a scaffold with random architectures under the influence of fluid dynamics.* J Biomater Appl, 2008. **23**(3): p. 229-45.
56. 'tRiet, K.v. and J. Tramper, *Basic Bioreactor Design.* First ed. 1991, New York, Basel: Marcel Dekker, Inc. 465.
57. Chen, X., et al., *Bioreactor expansion of human adult bone marrow-derived mesenchymal stem cells.* Stem Cells, 2006. **24**(9): p. 2052-9.
58. Timmins, N.E., et al., *Three-dimensional cell culture and tissue engineering in a T-CUP (tissue culture under perfusion).* Tissue Eng, 2007. **13**(8): p. 2021-8.
59. Zhao, F., et al., *Effects of oxygen transport on 3-D human mesenchymal stem cell metabolic activity in perfusion and static cultures: Experiments and mathematical model.* Biotechnol. Prog., 2005. **21**: p. 1269-1280.
60. Glossop, J.R. and S.H. Cartmell, *Effect of fluid flow-induced shear stress on human mesenchymal stem cells: differential gene expression of IL1B and MAP3K8 in MAPK signaling.* Gene Expr Patterns, 2009. **9**(5): p. 381-8.
61. Engelmayer, G.C., Jr., et al., *Cyclic flexure and laminar flow synergistically accelerate mesenchymal stem cell-mediated engineered tissue formation: Implications for engineered heart valve tissues.* Biomaterials, 2006. **27**(36): p. 6083-95.
62. Vunjak-Novakovic, G., et al., *Bioreactor cultivation of osteochondral grafts.* Orthod Craniofac Res, 2005. **8**(3): p. 209-18.
63. Toh, Y.C., et al., *A novel 3D mammalian cell perfusion-culture system in microfluidic channels.* Lab Chip, 2007. **7**(3): p. 302-9.
64. Ong, S.M., et al., *A gel-free 3D microfluidic cell culture system.* Biomaterials, 2008. **29**(22): p. 3237-44.
65. Anderson, E.J. and M.L. Knothe Tate, *Design of tissue engineering scaffolds as delivery devices for mechanical and mechanically modulated signals.* Tissue Eng, 2007. **13**(10): p. 2525-38.
66. Vossenbergh, P., et al., *Darcian permeability constant as indicator for shear stresses in regular scaffold systems for tissue engineering.* Biomech Model Mechanobiol, 2009.
67. Curran, J.M., R. Chen, and J.A. Hunt, *The guidance of human mesenchymal stem*

- cell differentiation in vitro by controlled modifications to the cell substrate*. Biomaterials, 2006. **27**(27): p. 4783-4793.
68. Catledge, S.A., et al., *Mesenchymal stem cell adhesion and spreading on nanostructured biomaterials*. J Nanosci Nanotechnol, 2004. **4**(8): p. 986-9.
69. Wei, J., et al., *Comparison of physical, chemical and cellular responses to nano- and micro-sized calcium silicate/poly(epsilon-caprolactone) bioactive composites*. J R Soc Interface, 2008. **5**(23): p. 617-30.
70. Kilian, K.A., et al., *Geometric cues for directing the differentiation of mesenchymal stem cells*. Proceedings of the National Academy of Sciences of the United States of America, 2010. **107**(11): p. 4872-4877.
71. Rosel, D., et al., *Up-regulation of Rho/ROCK signaling in sarcoma cells drives invasion and increased generation of protrusive forces*. Mol Cancer Res, 2008. **6**(9): p. 1410-20.
72. Titushkin, I. and M. Cho, *Distinct membrane mechanical properties of human mesenchymal stem cells determined using laser optical tweezers*. Biophys J, 2006. **90**(7): p. 2582-91.
73. Yourek, G., M.A. Hussain, and J.J. Mao, *Cytoskeletal changes of mesenchymal stem cells during differentiation*. ASAIO J, 2007. **53**(2): p. 219-28.
74. Dalby, M.J., et al., *The control of human mesenchymal cell differentiation using nanoscale symmetry and disorder*. Nature Materials, 2007. **6**(12): p. 997-1003.
75. Gadegaard, N., et al., *Optimizing substrate disorder for bone tissue engineering of mesenchymal stem cells*. Journal of Vacuum Science & Technology B, 2008. **26**(6): p. 2554-2557.
76. Takagi, M., et al., *Noninvasive measurement of three-dimensional morphology of adhered animal cells employing phase-shifting laser microscope*. J Biomed Opt, 2007. **12**(5): p. 054010.
77. Chen, C.S., et al., *Geometric control of cell life and death*. Science, 1997. **276**(5317): p. 1425-1428.
78. Nelea, V., et al., *Selective inhibition of type X collagen expression in human mesenchymal stem cell differentiation on polymer substrates surface-modified by glow discharge plasma*. J Biomed Mater Res A, 2005. **75**(1): p. 216-23.
79. Titushkin, I. and M. Cho, *Modulation of cellular mechanics during osteogenic differentiation of human mesenchymal stem cells*. Biophys J, 2007. **93**(10): p. 3693-702.
80. Ingber, D.E., *Tensegrity-based mechanosensing from macro to micro*. Progress in biophysics and molecular biology, 2008. **97**: p. 163 - 179.

81. Engler, A.J., et al., *Multiscale modeling of form and function*. Science, 2009. **324**(5924): p. 208-12.
82. Oh, S., et al., *Stem cell fate dictated solely by altered nanotube dimension*. Proc Natl Acad Sci U S A, 2009. **106**(7): p. 2130-5.
83. Engler, A.J., et al., *Microtissue elasticity: measurements by atomic force microscopy and its influence on cell differentiation* Methods Cell Biol., 2007. **83**: p. 521-45.
84. Huebsch, N., et al., *Harnessing traction-mediated manipulation of the cell/matrix interface to control stem cell fate*. Nat Mater, 2010. **9**(6): p. 518-26.
85. Huebsch, N. and D.J. Mooney, *Inspiration and application in the evolution of biomaterials*. Nature, 2009. **462**(7272): p. 426-32.
86. Sekiya, I., et al., *Expansion of Human Adult Stem Cells from Bone Marrow Stroma: Conditions that Maximize the Yields of Early Progenitors and Evaluate their Quality*. Stem Cells, 2002. **20**: p. 530 - 541.
87. Higuera, G., et al., *Quantifying In Vitro Growth and Metabolism Kinetics of Human Mesenchymal Stem Cells Using a Mathematical Model*. Tissue Engineering Part A, 2009. **15**(9): p. 2653-2663.
88. Lemon, G., et al., *Mathematical modelling of human mesenchymal stem cell proliferation and differentiation inside artificial porous scaffolds*. Journal of Theoretical Biology, 2007(249): p. 543 - 553.
89. Schop, D., et al., *Expansion of Mesenchymal Stem Cells Using a Microcarrier Based Cultivation System: Growth and Metabolism*. Journal of Tissue Engineering and Regenerative Medicine, 2008. **2**(2 - 3): p. 126 - 35.
90. Yang, C.Y., et al., *Labeling of human mesenchymal stem cell: Comparison between paramagnetic and superparamagnetic agents*. Journal of Applied Physics, 2009. **105**(7): p. -.
91. Suh, J.S., et al., *Efficient labeling of mesenchymal stem cells using cell permeable magnetic nanoparticles*. Biochem Biophys Res Commun, 2009. **379**(3): p. 669-75.
92. Reddy, A.M., et al., *Functional characterization of mesenchymal stem cells labeled with a novel PVP-coated superparamagnetic iron oxide*. Contrast Media Mol Imaging, 2009. **4**(3): p. 118-26.
93. Jing, X.H., et al., *In vivo MR imaging tracking of magnetic iron oxide nanoparticle labeled, engineered, autologous bone marrow mesenchymal stem cells following intra-articular injection*. Joint Bone Spine, 2008. **75**(4): p. 432-8.
94. Bulte, J.W., et al., *Chondrogenic differentiation of mesenchymal stem cells is inhibited after magnetic labeling with ferumoxides*. Blood, 2004. **104**(10): p. 3410-2; author reply 3412-3.

95. Gomez-Sjoberg, R., et al., *Versatile, fully automated, microfluidic cell culture system*. *Anal Chem*, 2007. **79**(22): p. 8557-63.
96. Reilly, G.C. and A.J. Engler, *Intrinsic extracellular matrix properties regulate stem cell differentiation*. *J Biomech*, 2010. **43**(1): p. 55-62.
97. Ingber, D.E., *Mechanical Control of Tissue Growth: Function Follows Form*. *Proc Natl Acad Sci U S A*, 2005. **102**(33): p. 11571- 11572.
98. Kloss, D., et al., *Drug testing on 3D in vitro tissues trapped on a microcavity chip*. *Lab on a Chip*, 2008. **8**(6): p. 879-884.
99. Bratlie, K.M., et al., *Rapid Biocompatibility Analysis of Materials via In Vivo Fluorescence Imaging of Mouse Models*. *Plos One*, 2010. **5**(3): p. -.
100. Mazzei, D., et al., *A high-throughput Bioreactor system for simulating physiological environments*. *Ieee Transactions on Industrial Electronics*, 2008. **55**(9): p. 3273-3280.
101. Yang, S.T., X.D. Zhang, and Y. Wen, *Microbioreactors for high-throughput cytotoxicity assays*. *Current Opinion in Drug Discovery & Development*, 2008. **11**(1): p. 111-127.
102. Kunz-Schughart, L.A., et al., *The use of 3-D cultures for high-throughput screening: The multicellular spheroid model*. *Journal of Biomolecular Screening*, 2004. **9**(4): p. 273-285.
103. Chung, B.G., L.F. Kang, and A. Khademhosseini, *Micro- and nanoscale technologies for tissue engineering and drug discovery applications*. *Expert Opinion on Drug Discovery*, 2007. **2**(12): p. 1653-1668.
104. Vandenburgh, H., *High-Content Drug Screening with Engineered Musculoskeletal Tissues*. *Tissue Engineering Part B-Reviews*, 2010. **16**(1): p. 55-64.



A grayscale microscopy image showing several elongated, spindle-shaped cells (hMSCs) scattered across the field. The cells exhibit characteristic morphology with tapered ends and some internal structure. The background is a uniform light gray.

I

2D Kinetics of hMSCs

Quantifying *In Vitro* Growth and Metabolism Kinetics of Human Mesenchymal Stem Cells Using a Mathematical Model

Gustavo Higuera¹, Deborah Schop², Frank Janssen¹, Riemke van Dijkhuizen-Radersma², Anton van Boxtel³, and Clemens A. van Blitterswijk¹

¹Department of Tissue Regeneration, Institute for Biomedical Technology, University of Twente, Enschede, The Netherlands.

²Xpand Biotechnology BV, Bilthoven, The Netherlands.

³Systems and Control Group, Wageningen University, Wageningen, The Netherlands.

Abstract

Human mesenchymal stem cell (hMSCs) metabolism needs better quantitative understanding in order to identify, understand and subsequently optimize the processes in hMSCs expansion *in vitro*. For this purpose, we analysed hMSCs growth *in vitro* with a mathematical model based on the mass balances for viable cell numbers, glucose, lactate, glutamine and glutamate. The mathematical modelling had two aims: (1) to estimate kinetic parameters of important metabolites for hMSCs monolayer cultures, and (2) to quantitatively assess assumptions on hMSCs growth. Two cell seeding densities were used to investigate growth and metabolism kinetics of MSCs from three human donors. We analysed growth up to confluency and used metabolic assumptions described in literature. Results showed a longer initial phase, a slower growth rate and a higher glucose, lactate, glutamine and glutamate metabolic rates at the lower cell seeding density. Higher metabolic rates could be induced by a lower contact inhibition effect when seeding at 100 cells/cm² than when seeding at 1000 cells/cm². In addition, parameter estimation describing kinetics of hMSCs in culture, depending on the seeding density, showed doubling times in the order of 17 to 32 h, specific glucose consumption in the order of 1.25×10^{-1} to 3.77×10^{-1} pmol/cell/h, specific lactate production in the order 2.48×10^{-1} to 7.67×10^{-1} pmol/cell/h, specific glutamine production in the order of 7.04×10^{-3} to 2.27 pmol/cell/h, and specific glutamate production in the order of 4.87×10^{-1} to 23.4 pmol/cell/h. Lactate to glucose yield ratios confirmed that hMSCs use glucose via anaerobic glycolysis. In addition, glutamine and glutamate metabolic shifts were identified that could be important for understanding hMSCs growth *in vitro*. This study showed that the mathematical modelling approach supports quantitative analysis of important mechanisms in hMSCs proliferation *in vitro*.

Introduction

The emerging discipline of tissue engineering has as one of its grand aims to understand the principles of tissue growth, and apply this to produce functional replacement tissue for clinical use [1]. Different tissue engineering strategies use human mesenchymal stem cells (hMSCs) because of their multipotency, i.e. their ability to differentiate into different cell types, such as cartilage, bone, muscle, tendon, ligament, and fat [2-4]. Because hMSCs numbers are low in the body, expansion is necessary in order to obtain sufficient cells to induce clinically-relevant sized tissue.

Currently, hMSCs growth continues to be the focus of not only qualitative, but also quantitative studies [5, 6]. Due to the high complexity of biological systems, mathematical modelling in the scope of systems biology will be useful in analysing hMSCs growth quantitatively as shown in other cell cultures [7, 8]. MacArthur and Oreffo (2005) have suggested that the integration of mathematical modelling with experimentation in an iterative framework may prove crucial in taking tissue engineering from concept to reality; where integration of mathematical modelling and experimentation would be practical for channelling knowledge from different fields of expertise towards a common goal.

The use of mathematical models is common for simulation, optimisation and control purposes. Mathematical models can also aid in the understanding and elucidation of underlying mechanisms and highlight the accuracy or descriptive ability in parts of the mathematical model where experimental and simulated data cannot be reconciled [9]. Two notable examples of mathematical modelling of hMSCs growth and metabolism are found in the literature: The first is Zhang *et al.*, (2005) who investigated hMSCs growth kinetics and metabolism under static and perfusion conditions on poly (ethylene) terephthalate (PET) constructs. This study focused on the oxygen transport equations across the construct with respect to static and perfusion conditions and a kinetic description of cell growth in this constructs from offline measurements of cell numbers [10]. In the other example, Lemon *et al.*, (2007) developed a mathematical model which describes how the quantity of undifferentiated and differentiated hMSCs and the amount of extra-cellular matrix (ECM) evolve with time under both hypoxic and normoxic conditions inside fibrous PET scaffolds [11]. However, these papers did not address the dynamic role of metabolites. Therefore, we have designed a study where a mathematical model is used to investigate the dynamics of components of the citric acid (TCA) cycle and amino acid metabolism in hMSCs cultivation.

Because of their importance in mammalian cultures, glucose, lactate, glutamine and glutamate were considered in this work to assess growth quantitatively. Figure 1 shows the main compounds involved in the metabolism of glucose, lactate, glutamine and glutamate. The latest studies estimate that complete aerobic oxidation of glucose yields a maximum of 30 moles adenine triphosphate (ATP) per mol glucose [12] whereas glucose catabolism by anaerobic glycolysis yields two moles of ATP and two moles of lactate per mole of glucose [13]. Therefore, the stoichiometry of glycolysis can provide information on hMSCs energy production efficiency under different conditions.

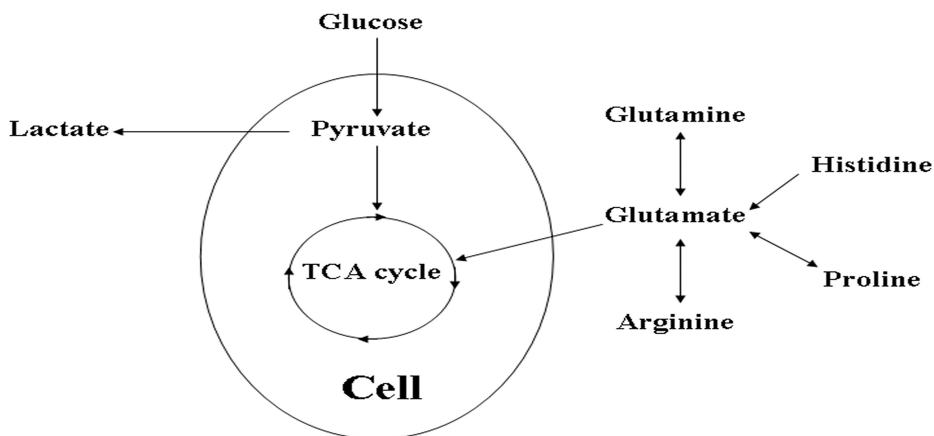


Figure 1 Overview of pathways investigated. Amounts of glucose, lactate, glutamine and glutamate were measured in the experimental work.

Glutaminolysis (i.e. the conversion of glutamine into glutamate via the citric acid cycle) yields about 27 moles of ATP and 2 moles of ammonia. Glutamine metabolism can either yield 2 moles of lactate, 1 mole of ammonia, and 9 mole of ATP or 1 mole of alanine, 1 mole of ammonia and 9 mole of ATP [14]. In addition to glutamine, the carbon skeletons of three five-carbon amino acids (proline, arginine, and histidine) enter the TCA cycle at α -ketoglutarate. These amino acids are first converted into glutamate [13] and then fed into the TCA cycle. Thus, glutamine and glutamate profiles can indicate changes on the amino acid metabolic status of hMSCs.

In this work, we used a basic mathematical model for the analysis and understanding of growth processes with two aims: (1) to estimate kinetic parameters from measurements of glucose, lactate, glutamine and glutamate, (2) to quantitatively assess assumptions on hMSCs growth in two-dimensional cultures. For the latter aim, we investigated different cell seeding densities (100 and 1000 cells/cm²) since studies show that low cell seeding densities favour hMSCs expansion and longer doubling times [15-19]. Medium samples and hMSCs were harvested every day

up to confluency. For every time point, measurements for viable cells, dead cells, glucose, lactate, glutamine and glutamate were obtained.

Sidoli *et al.*, (2004) explained that mathematical models can be classified as structured or unstructured, segregated or unsegregated, deterministic or stochastic [9]. First, a structured mathematical model includes a detailed description of the intracellular processes in either the physical or the biochemical sense, while in unstructured models, these processes are only partially considered. Second, an unsegregated mathematical model assumes an average cell, so that the cell population can be considered homogeneous. Deterministic models assume that the cells are not subject to random variability which is taken into account by stochastic models.

In the mathematical model described here, it is assumed that an hMSCs population is a homogeneous population whose behaviour can be described by an average cell. The mathematical model is represented by differential equations describing the mass balance for each metabolite. Thus, the mathematical model we used can be classified as an unstructured, unsegregated, and deterministic.

We chose this approach to clarify and identify the metabolic processes that occur during hMSCs growth in standard hMSCs cultivation. From data and mathematical model, kinetic parameters were identified that characterize growth quantitatively in a closed two-dimensional batch system such as the tissue culture flask (T-flask). These parameters can be used for comparing the metabolic status of hMSCs in different two-dimensional and three-dimensional expansion systems.

Materials and Methods

Isolation, culture and cryopreservation of hMSCs

We isolated, cultured and cryopreserved human mesenchymal stem cells (hMSCs) as described by Both *et al.*, (2007) [19]. We obtained hMSCs from 3 donors (Table 1) who were undergoing total hip replacement surgery and gave informed consent for bone marrow biopsy, approved by the local medical ethical committee. Mononucleated cells were counted in the aspirate and plated at a density of 500,000 cells/cm² in T-flasks (Nunc, Thermo Fischer Scientific, Roskilde, Denmark). After addition of α -minimal essential medium (α MEM) proliferation medium, cells were cultured for four to five days. The α MEM proliferation medium contained minimal essential medium (GIBCO, Carlsbad, CA); 10 % fetal bovine serum of a selected batch (FBS; Biowhittaker, lot:4SB0010); 0.2mM l-ascorbic-acid-2-phosphate (Sigma, St Louis, MO); penicillin G (100 Units/ml, Invitrogen); streptomycin (100 μ g/ml, Invitrogen); 2mM l-glutamine (Sigma) and 1ng/ml basic fibroblast growth factor (Instruchemie,

Delfzijl, The Netherlands). Cells were cultured at 37°C in a humidified atmosphere of 5% carbon dioxide.

Table 1 hMSC donor information.

Donor	Aspiration site	Sex	Age	Fold increase at 100 cells/cm ²	Fold increase at 1000 cells/cm ²	Total culture period [h]	Total culture period [h]
1	Acetabulum	F	81	54 after 119 h	23 after 119 h	217	119
2	Acetabulum	M	65	45 after 117 h	26 after 117 h	231	117
3	Acetabulum	F	76	73 after 95 h	37 after 95 h	239	95

After the four to five day culture period, non-adherent cells and α MEM proliferation medium were discarded. Adherent cells were thoroughly washed twice with phosphate-buffered-saline (PBS, Sigma) and α MEM proliferation medium was refreshed. We proliferated adherent cells for two passages and cryopreserved them. The passage number was defined by every harvest with 0.25% trypsin/EDTA (GIBCO).

Culture density and proliferation

Cryopreserved cells were thawed and hMSCs - passage 2 - were recounted and plated at 100 and 1,000 cells/cm² in 25 cm² T-flasks (T-25 flasks) in α MEM proliferation media. hMSCs were cultured in Sanyo incubators. α MEM proliferation medium was not refreshed to maintain a batch culture configuration. Every day, for each seeding density, three T-25 flasks were sacrificed per seeding density to obtain cell numbers and their metabolic profile. The medium was analysed on the same day of harvest. To harvest cells, the T-25 flasks were washed with PBS before hMSCs were enzymatically detached with 0.25% trypsin/EDTA.

Viable and dead hMSCs

After harvest, viable cell numbers were obtained with the Bürker-Türk method by discriminating viable and dead hMSCs with trypan blue (Sigma). Cell death was quantified with both trypan blue and medium analysis of lactate dehydrogenase (LDH) signal with the Cytotox-one Homogeneous Membrane Integrity Assay (Promega). LDH signal was calibrated for every hMSCs donor by measuring the LDH signal three times ($n = 3$) for each of five cell concentrations from 2×10^3 to 2.5×10^5 cells/ml. The slope estimated from linear regression corresponded to the LDH signal/cell ratio (Donor 1: 6.5×10^{-3} , Donor 2: 8.1×10^{-3} and Donor 3: 5.6×10^{-3}). From three runs per donor i.e. three T-25 flasks sacrificed per day, four medium samples per run ($n = 12$) were obtained and its LDH signal measured in time. Dead

cell numbers for every donor were obtained by dividing the signal in time by their respective LDH signal/cell ratio.

Metabolic profile and volume

Daily measurements were performed for every donor from independent T-25 flasks ($n = 3$). Glucose and lactate were measured in the Vitros DT60 II chemistry system (Ortho-Clinical Diagnostics). In addition, glutamine and glutamate were measured with the Glutamine/Glutamate determination kit (Sigma). Volume change of 2.1×10^{-3} ml/h (with 2.1×10^{-4} as a standard deviation for $n = 3$) was measured in a Sanyo incubator at 37 Celsius with 60% relative humidity. Concentrations measured were normalised to the volume changes.

Estimation of degradation kinetics

All degradation experiments included medium incubated without cells at 37 °C and 5% CO₂, where metabolites were measured with their respective methods. LDH signal for dead cell numbers degraded linear in time (Fig. 3 Right) at a rate of $2.8 \pm 0.36 \times 10^{-1}$ LDH signal/h from three replicates ($n = 3$) per data point. For every donor, LDH signals were measured from four medium samples per run (Runs per donor = 3, $n = 12$). Then, these were normalized to their degradation in time before dead cell numbers were calculated. Glutamine degradation obeys first-order kinetics [20]. The degradation rate constant for glutamine (k_{gd}) was estimated experimentally to be $6.37 \pm 0.85 \times 10^{-3}$ h⁻¹. Also, the first-order degradation constant for glutamate (k_{ed}) was estimated experimentally to be $7.3 \pm 1.4 \times 10^{-3}$ h⁻¹. Furthermore, degradation of glucose and lactate was measured experimentally to be negligible thus we put $k_{gd} = 0$ on equation (4).

Statistical Analysis

For every donor, all data points for cell number, glucose, lactate, glutamine and glutamate are based on replicates for each of three parallel runs i.e. three T-25 flasks sacrificed per day. Error bars in graphs with experimental data represent the standard deviation of measurements.

Analysis of growth and metabolism characteristics was performed by parameter estimation and the obtained parameter values were evaluated on the basis of their 95 % confidence intervals.

Mathematical Model Description

The principles to model were chosen based on literature on mammalian cell cultures [7-9, 21]. A T-flask is considered as a batch system, where cells grow on their metabolites. The system can be described with the set of mass balances equations (1) through (4). The viable biomass is given by:

$$\frac{dX_v}{dt} = X_v \cdot (\mu - \mu_d) \quad (1)$$

Equation (1) describes the change of the total number of viable cells with time in a differential equation form and includes both viable cell growth (μX_v) and cell death ($\mu_d X_v$). The specific growth rate for the cells is given by

$$\mu = \mu_{max} \cdot \frac{X_g}{K_g + X_g} \quad (2)$$

with μ as specific growth rate which is based on Monod type kinetics for glucose. The Monod equation (2) indicates that for glucose concentrations around the Monod constant (K_g), the specific growth rate (μ) is half the maximum specific growth rate (μ_{max}). If K_g is much smaller than the glucose concentration, μ equals μ_{max} . The value of K_g , 0.4mM (i.e. 2×10^{-6} moles in 5 ml volume) is taken from literature [22]. With total glucose amounts in 5 ml ranging from 1.5 to 2.25×10^{-5} moles, μ is $90 \pm 2\%$ of μ_{max} .

The amount of dead cells is given by the mass balance:

$$\frac{dX_d}{dt} = X_v \cdot \mu_d \quad (3)$$

With X_d as the total dead cell number (X_d) produced from the lysis of the cell membrane with μ_d defined as the death rate h^{-1} of viable cells (X_v).

The mass balances of metabolites are given by:

$$\frac{dX_m}{dt} = \pm q_m \cdot X_v - k_{md} \cdot X_m \quad (4)$$

where the subscript m refers to the metabolites (glucose, lactate, glutamine or glutamate). q_m refers to the specific metabolite (m) reaction rate per average cell per h, q_m is constant and may be positive or negative (\pm) depending on whether the metabolite is produced or consumed, respectively. k_{md} represents the first-order degradation rate constant for the metabolites.

We expect that throughout a cultivation glucose and glutamine are consumed; while lactate and glutamate are produced. Maintenance coefficients are the minimum amounts of a substrate that a cell needs for its survival. However, because of a high parameter correlation, maintenance coefficients cannot be estimated from batch experiments. Consequently, q_g and q_q on equation (4) include both an unknown maintenance coefficient and the consumption towards biomass production.

Mathematical modelling and parameter estimation

The mathematical model equations 1 - 4 comprise a set of ordinary differential equations (ODEs) which were solved with a standard differential equation solver in Matlab (`ode45` in version 7.0.4 release 2007a; Mathworks, Natick, MA) on a windows-based system. The initial values for solving the differential equation were set to the seeding density and the experimentally determined composition (glucose, lactate, glutamine and glutamate) in fresh α MEM proliferation medium from three medium samples. Mathematical model parameter values for the three donors were obtained by nonlinear least squares regression which minimizes the sum of the quadratic error over an experiment (Matlab function `nlinfit`). Next, the 95 % confidence intervals for the parameters were calculated (Matlab function `nlparci`).

The experimentally obtained initial values had a low variation and were not considered as parameters to be estimated by nonlinear least squares regression.

Results

This study used a mass-balance-based mathematical model to analyse *in vitro* growth and metabolism kinetics of hMSCs seeded at 100 and 1000 cells/cm². Viable cell numbers, dead cell numbers, glucose, lactate, glutamine and glutamate were experimentally measured and analysed at both cell seeding densities. The results of the analysis are described below.

1. Cell growth

Figure 2 shows the counted viable cell numbers and the mathematical model results for three donors. The cell numbers increased in time up to 130 h when seeded at 1000 cells/cm² and up to 230 h when seeded at 100 cells/cm². When seeding at 1000 cells/cm², cell counting repeatedly showed larger standard deviations after 130 h. The three donors showed high dispersion in cell numbers after 130 h. This result lead us to set limits for the mathematical model based on reliable cell number measurements.

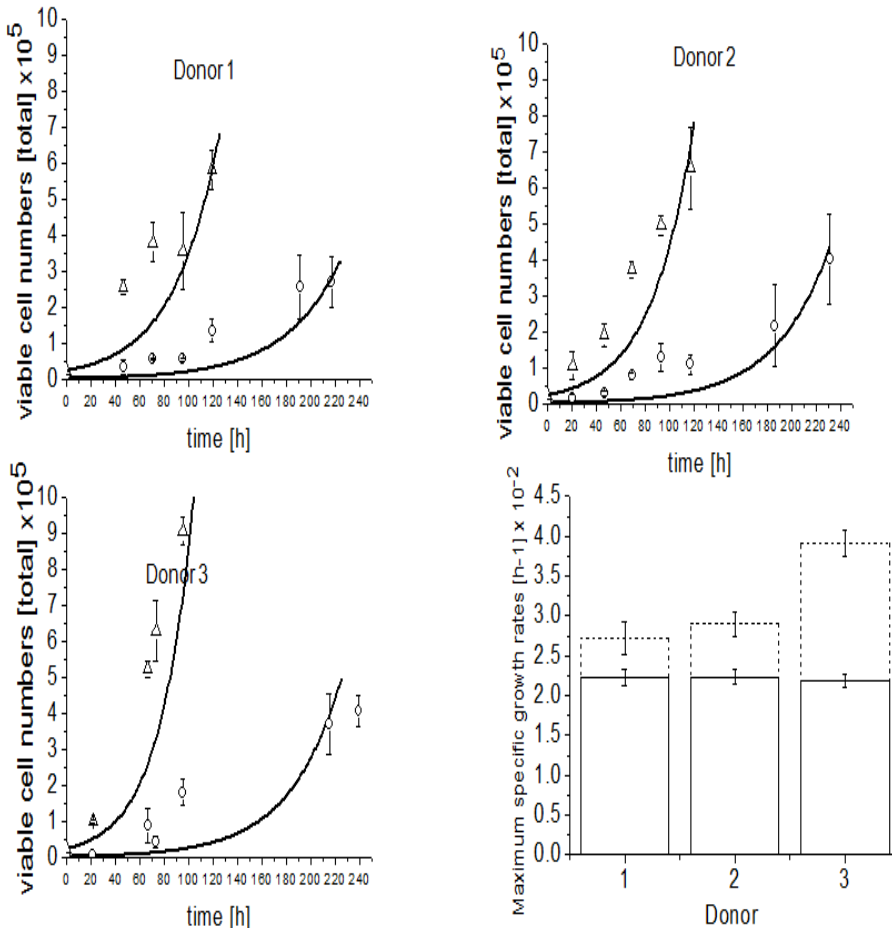


Figure 2 Total hMSCs viable cell numbers for the three donors. Viable cell numbers for seeding densities 100 cells/cm² (\circ) and 1000 cells/cm² (Δ). Mathematical modelling results (—) for both seeding densities. *Bar plot (Bottom right) shows for the three donors the estimated specific growth rates and their 95 % confidence interval when seeding at 100 cells/cm² (—) or at 1000 cells/cm² (---). *See erratum at the end of chapter showing significance for donor 3 only.

Dead cell numbers (Fig. 3 left) showed on average ($n = 3$ donors) as high as 0.035 % dead cells from total cells (dead and viable). Visual inspection with trypan blue also confirmed the presence of only a few dead cells. Thus, cell death was assumed negligible and μ_d in equations (1) and (3) was equal to zero. In addition, pH remained within physiological values throughout the culture period (7.2 to 7.3).

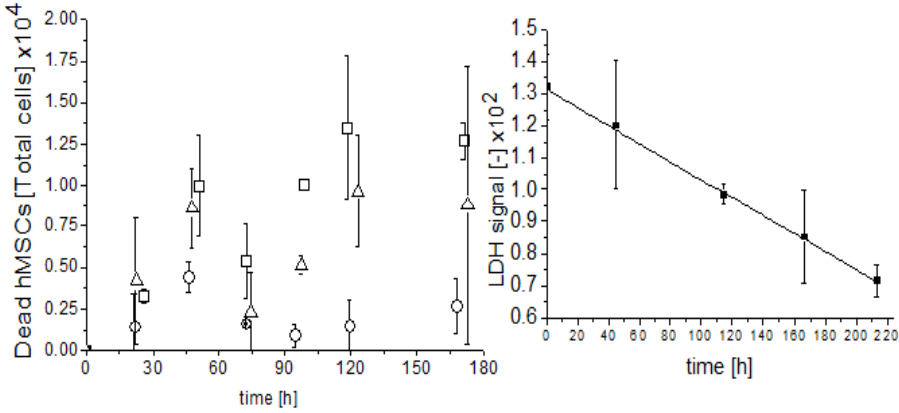


Figure 3 Measured total dead cell numbers (Right) for donor 1 (□), donor 2 (o) and donor 3 (Δ) at seeding densities 1000 cells/cm². Each LDH signal was normalized to LDH signal/cell values depending on the donor to yield their respective dead cell numbers. LDH signal degrades in standard culture conditions (Right). Each data point was measured three times; mean value and standard deviation are plotted.

In this work, we present the growth regions as initial and exponential phases to describe the growth differences relative to the seeding densities. The initial phase is the period where cell growth is still close to the seeding density and where growth is difficult to detect. The exponential phase is the region where the cell growth can be detected and where the cell numbers increase exponentially according to mathematical modelling results. The mathematical model results showed that for the investigated hMSCs seeding densities, the initial phase was 35 to 45 h long at 100 cells/cm², and negligible at 1000 cells/cm². In addition, mathematical modelling viable-cell numbers were below experimental values during the time interval (40 - 100 h).

Table 2 Maximum specific growth rates (μ_{max}) or doubling times (t_d) at both cell seeding densities for the three donors.

Donor	μ_{max} [h ⁻¹] x 10 ⁻² 100 cells/cm ²	Doubling time [h] 100 cells/cm ²	μ_{max} [h ⁻¹] x 10 ⁻² 1000 cells/cm ²	Doubling time [h] 1000 cells/cm ²
1	2.23 +/- 0.11	31.1	2.72 +/- 0.21	25.5
2	2.23 +/- 0.09	31.1	2.9 +/- 0.16	23.9
3	2.19 +/- 0.08	31.7	3.91 +/- 0.17	17.7

By fitting equation (1) and (2) to the data, the maximum growth rates for the three donors (μ_{max}) were estimated. μ_{max} results are shown in Figure 2 (Bottom right) and Table 2. The 95 % confidence intervals in Figure 2 show that for the three donors μ_{max} is significantly lower at 100 cells/cm². In addition, μ_{max} values did not vary significantly between donors at 100 cells/cm² whereas at 1000 cells/cm² a significant variation between the donors was found. Solving equation (1) and rewriting leads to the doubling time ($t_d = \ln(2) / \mu_{max}$). Doubling times ranged from 31.1 to 31.7 h when cells were seeded at 100 cells/cm² and from 17.7 to 25.5 h when cells were seeded at 1000 cells/cm² (Table 2).

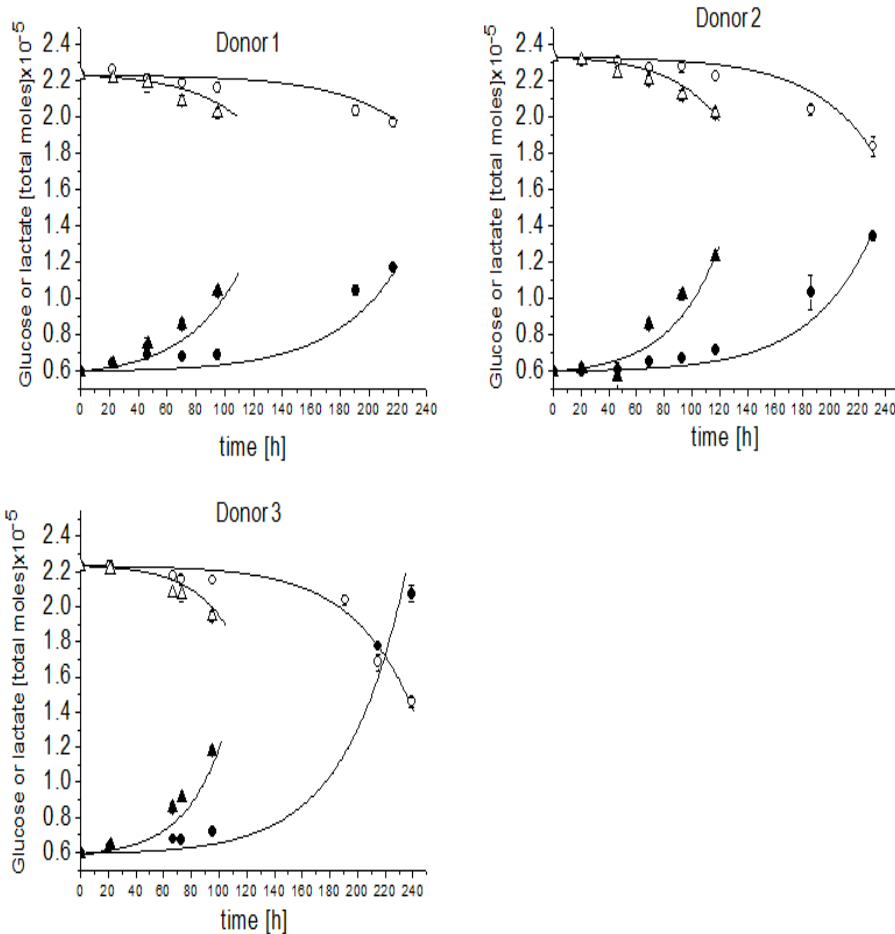


Figure 4 Total moles of glucose and lactate in medium for the three donors. Moles of glucose at seeding densities 100 cells/cm² (o) and 1000 cells/cm² (Δ). Moles of lactate at seeding densities 100 cells/cm² (\bullet) and 1000 cells/cm² (\blacktriangle). Mathematical modelling results (—) for both seeding densities.

2. Glucose and lactate metabolism

Figure 4 shows the mathematical modelling results for both glucose and lactate throughout the culture period of cells seeded at 100 and 1000 cells/cm². Experimental measurements showed that glucose was consumed and lactate was produced in both cell seeding densities. In addition, experimental results showed that proliferation-inhibiting concentrations for lactate of 25mM [23] were not reached during the culture period. Mathematical model results for glucose and lactate were close to the experimental values in both cell seeding densities.

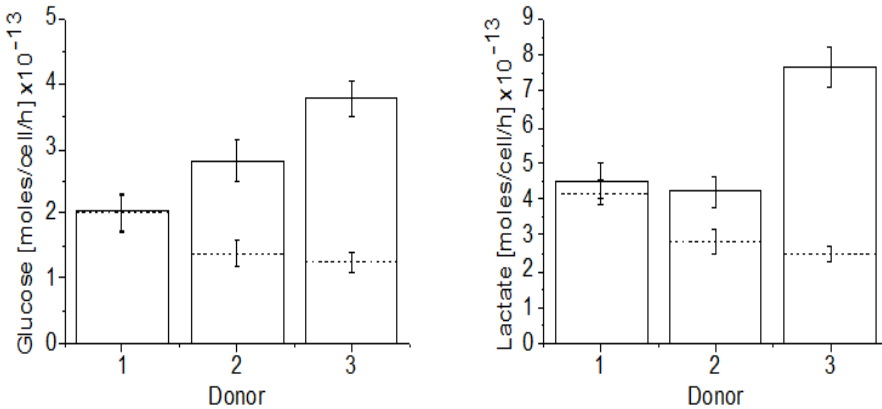


Figure 5 Specific glucose consumption rates q_g (left) and lactate production rates q_l (right) for the three donors. Seeding densities 100 cells/cm² (—) and 1000 cells/cm² (.). Estimated values through non-linear least squares regression and 95 % confidence intervals are given. Parameter values are listed in table 3.

The estimated specific reaction rates under these conditions are shown in Figure 5. From the 95 % confidence intervals follows that the estimated values for q_g and q_l were significantly higher at the lower cell seeding density for donors 2 and 3. In addition, the results showed that q_g and q_l vary within donors. The lactate to glucose ratio ($Y_{l/g}$) is defined as the ratio of q_l to q_g . $Y_{l/g}$ describes the efficiency of the anaerobic glycolysis reaction. $Y_{l/g}$ values for each donor and seeding density are found on Table 3.

Table 3 Glucose specific consumption rates (q_g), and lactate specific production rates (q_l) and lactate to glucose ratio ($Y_{l/g}$) when seeding at 100 cells/cm² and 1000 cells/cm² for the three donors.

Donor	$q_g \times 10^{-12}$ 100 cells/cm ²	$q_g \times 10^{-12}$ 1000 cells/cm ²	$q_l \times 10^{-12}$ 100 cells/cm ²	$q_l \times 10^{-12}$ 1000 cells/cm ²	$Y_{l/g}$ 100 cells/cm ²	$Y_{l/g}$ 1000 cells/cm ²
1	0.203 +/- 0.028	0.2 +/- 0.029	0.45 +/- 0.049	0.419 +/- 0.0373	2.21	2.1
2	0.281 +/- 0.032	0.139 +/- 0.0212	0.42 +/- 0.041	0.282 +/- 0.0351	1.5	2.03
3	0.377 +/- 0.0267	0.125 +/- 0.0156	0.767 +/- 0.0545	0.248 +/- 0.0215	2.03	1.98

3. Glutamine and glutamate metabolism

Figure 6 shows experimental glutamine and glutamate measurements and their respective mathematical model values. Figure 6 shows that there is a net decrease of the amount of glutamine throughout culture at both cell seeding densities. However, for all donors, the measured values and the mathematical model results are above the line for spontaneous degradation of glutamine. This leads, surprisingly, to the conclusion that hMSCs are glutamine producers instead of consumers. This result is reflected by model fitting results up to 130 h which give the specific production rates of glutamine (Fig. 7).

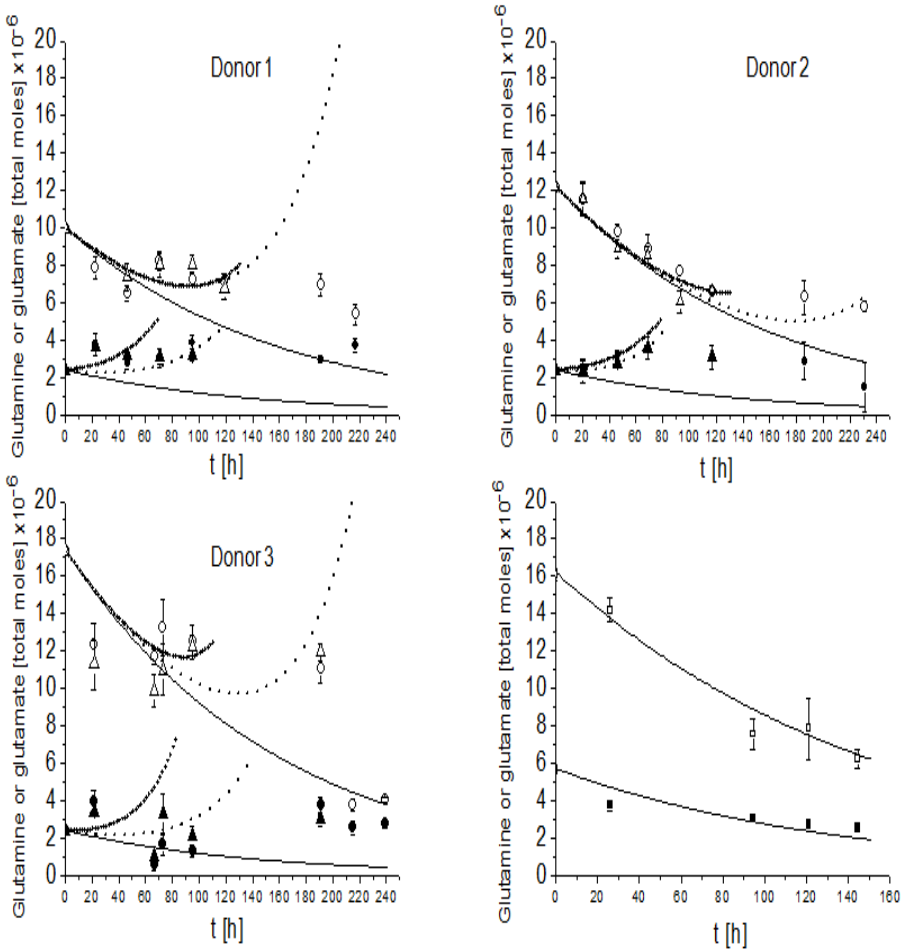


Figure 6 Total moles of glutamine or glutamate for the three donors. Moles of glutamine at seeding densities 100/cells/cm² (o) and 1000/cells/cm² (Δ). Moles of glutamate at seeding densities 100/cells/cm² (●) and 1000/cells/cm² (▲). Degradation in cell free medium of glutamine (□) (Bottom right) and glutamate (■) (Bottom right). Mathematical modelling results for glutamine and glutamate at seeding densities 100/cells/cm² (—) and 1000/cells/cm² (••). Spontaneous degradation in cell-free medium of glutamine and glutamate is plotted in the graphs (—) for each donor and for experimental values (Bottom right).

The mathematical model tracked experimental data on production of glutamate q_e for the first 30 – 70 h of culture, depending on the donor (Fig. 6). The assumption by equation (4) of glutamate hMSCs production only holds for the beginning of the culture in all donors. Thereafter, different trends depending on the donor were observed. For all donors, the measured values and the mathematical model results are above the line for spontaneous degradation of glutamate.

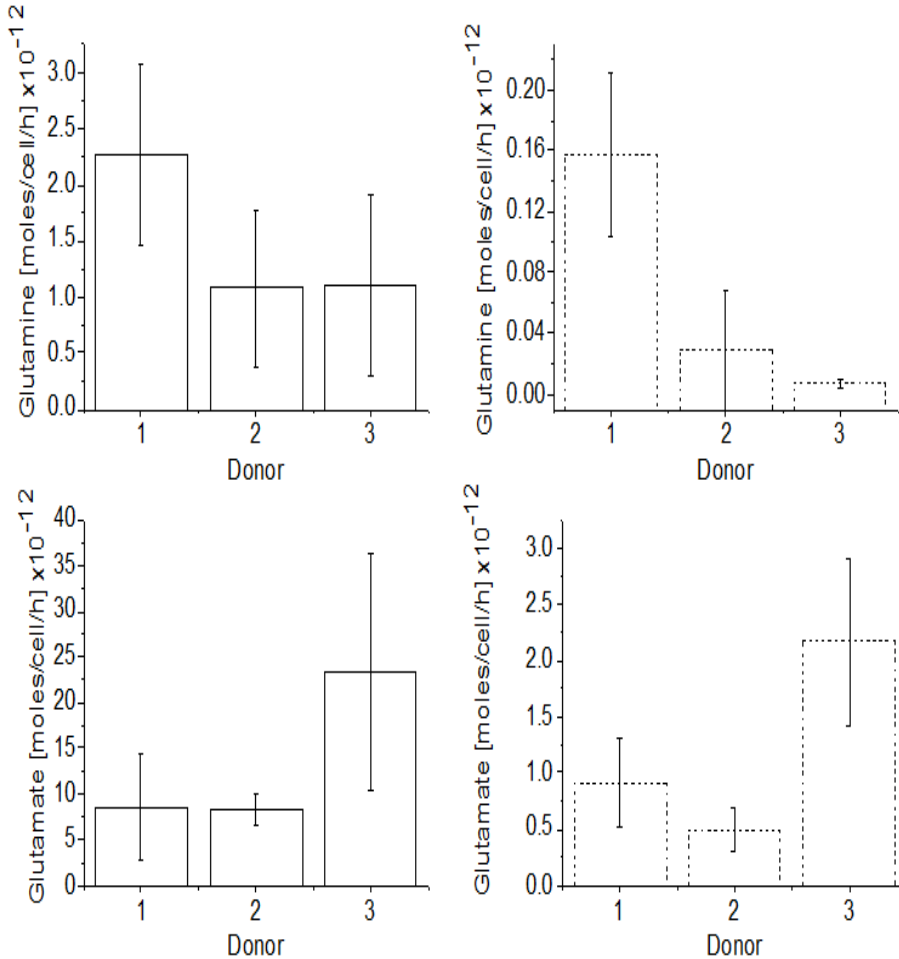


Figure 7 Estimated specific glutamine q_q (Top) and glutamate q_e (Bottom) production rates and their 95 % confidence intervals for the three donors. q_q and q_e when seeding at 100 cells/cm² (—, left) and 1000 cells/cm² (---, right). The scale on the y-axis varies depending on the seeding density.

Figure 7 and table 4 show the specific production rates of glutamine (q_q) and glutamate (q_e) when seeding at 100 and 1000 cells/cm² for three donors. The 95 % confidence intervals show that the production values for glutamine and glutamate were significantly higher at 100 cells/cm². Furthermore, production values for glutamine and glutamate varied within donors at both cell seeding densities.

2D Kinetics of hMSCs

Table 4. Specific production rates of glutamine (q_q) and glutamate (q_e) when seeding at 100 cells/cm² and 1000 cells/cm² for the three donors.

Donor	$q_q \times 10^{-12}$ 100 cells/cm ²	$q_q \times 10^{-12}$ 1000 cells/cm ²	$q_e \times 10^{-12}$ 100 cells/cm ²	$q_e \times 10^{-12}$ 1000 cells/cm ²
1	2.27 +/- 0.803	0.157 +/- 0.054	8.45 +/- 5.78	0.9 +/- 0.397
2	1.08 +/- 0.7	0.0284 +/- 0.0394	8.34 +/- 1.73	0.487 +/- 0.195
3	1.11 +/- 0.81	0.00704 +/- 0.0028	23.4 +/- 12.9	2.17 +/- 0.743

Discussion

The mathematical model equations (1) through (4) can be used to analyse quantitatively hMSCs growth and metabolites profiles (i.e. glucose, lactate, glutamine and glutamate) in time in a T-flask. To our best knowledge, currently there are no mathematical models used to understand hMSCs cell growth and metabolic activity in a T-flask.

1. Cell growth

In a typical batch process the number of living cells varies with time. After a lag phase, with only a small increase of cell numbers, a period of rapid growth ensues [24]. It is a challenge to evaluate the extent of the lag phase from hMSCs cultured *in vitro* because of two reasons: Firstly, cells in an hMSCs population are at different stages of the cell cycle and secondly, the error from cell counting methods is large. In addition, mathematical modelling needs expressions that account for the lag phase as a period where growth rates are approximately zero, in this work, μ is not equal to zero. Thus, we use initial phase as a more generic term to describe the region where a small increase of cell numbers is seen. Additionally, we defined the region where growth numbers increased drastically as the exponential phase.

The growth model presented by Mohler *et al.*, (2008) on microcarrier cultures shows that anchorage dependent cells have a lag phase mainly determined by the attachment process [8]; here, it was assumed that the initial phase is determined by levels of growth factors [25] and nutrients. Furthermore, the mathematical model results identified differences in the initial-phase duration depending on the seeding density. Mathematical modelling results confirmed that at the lower cell seeding densities, hMSCs present a longer initial phase and slower growth rates [15-19]. Gregory *et al.*, (2003) showed that the mechanism controlling growth rates and phases depends on the levels of secreted factors such as dickkopf-1 (Dkk-1), an

inhibitor of the canonical Wnt signalling pathway [25].

Distinctively, the viable cell number data did not suggest that a stationary phase followed. Cell cultures close to confluency (> 130 h at 100 cells/cm² and > 220 h at 1000 cells/cm²) showed cell aggregates. This suggested multilayer growth and showed cell number data with larger standard deviations. Due to these results, the mathematical modelling analysis focused on the initial and exponential phases.

In this work, we define the growth rate in equation (2). This definition showed discrepancies of mathematical modelling and experimental hMSCs numbers during the exponential phase. The growth rate could also be defined as a function of both glucose and glutamine as assumed in mathematical models of MDCK cells [8], CHO and HEK-293 cells [7], among others. However, extension of equation (2) with this assumption did not affect the fit of the mathematical model of viable hMSCs. To define the growth process, an alternative option is to assume a zero-order expression for growth in that case equation (1) is replaced by $dX_v/dt = k$. Although the zero-order expression gives a somewhat better correlation for viable cell numbers; the mathematical model results for the other variables (glucose, lactate, glutamine and glutamate, which are linked with the biomass in equation 4) were deteriorated.

Another assumption would be to consider a changing growth rate. Lemon *et al.*, (2007) showed that under the assumption of a changing growth rate in time dependant upon the amount of extra cellular matrix (ECM) present, and the competition for space, the total cell volume fraction model fit was acceptable; whereas the undifferentiated cell volume fraction model fit was poorer [11]. In addition, an empirical mathematical model for density-dependant growth of anchorage-dependent mammalian cells [21], based on a tuneable constant, showed good results with experimental data. However, the biological significance of a tuneable constant to define the growth rate needs further assessment with respect to metabolism. Literature and growth rate assumptions in this work suggest that hMSCs growth-rate-limiting metabolites are not yet clearly identified.

The analysis leads us to conclude that the growth rate needs to be addressed experimentally in future studies by investigating both rate-limiting substrates and rate-limiting concentrations in order to obtain a clearer understanding on the mechanisms involved in hMSCs growth *in vitro*.

2. Glucose and lactate metabolism

$Y_{1/g}$ showed glucose catabolism through anaerobic glycolysis as has been shown by hMSCs in other two-dimensional and three-dimensional culture systems [10, 23].

The mathematical modelling results confirm that hMSCs use glucose by anaerobic glycolysis independently of the donor or cell seeding density as shown by a value around two of the lactate to glucose stoichiometric ratio $Y_{l/g}$ with the exception of donor 2 at 100 cells/cm² (Table 3). Furthermore, at 100 cells/cm², both q_g and q_l are higher than the respective values at 1000 cells/cm² with the exception of donor 1 at 100 cells/cm² (Fig. 5).

Slower growth rates and higher metabolite rates when seeding at 100 cells/cm² are counterintuitive. An interpretation of this result could be that contact inhibition, defined as the ability of a cell to deplete the medium around itself of extracellular mitogens, thereby depriving its neighbours [26], gradually causes the differences in metabolic rates during the exponential phase in hMSCs cultures. Thus, the less readily available substrates are, the lower metabolic rate of consumption and production are when seeding at 1000 cells/cm². The higher availability of nutrients around a cell could also explain the higher fold increase of cells (Table 1) when seeding at 100 cells/cm² as also observed by Sekiya *et al.* (2002). The quantitative effect of contact inhibition on hMSCs could be useful in understanding hMSCs growth and designing two-dimensional and three-dimensional expansion systems.

Glucose and lactate mathematical model fits were acceptable regardless of the seeding density. This indicates that either, mechanisms expressed on equation (4) are representative for both substrates' kinetics or that the concentrations do not change as drastically for the mathematical model to deviate. More insight into glucose and lactate kinetics can be obtained from longer culture runs where hMSCs numbers can be analysed with respect to metabolite depletion. In continuous cultures, evaluation of metabolites should be pursued with respect to rate limiting concentrations and the maintenance coefficients.

3. *Glutamine and glutamate metabolism*

Glutamine serves as an essential metabolic precursor in nucleotide, glucose and amino-sugar biosynthesis, glutathione homeostasis and protein synthesis [27]. The growth of proliferating cells such as fibroblasts, lymphocytes and enterocytes relies heavily on glutamine as an oxidative energy source [28]. However, most tissue culture media contain large amounts of glucose, and consequently the addition of L-glutamine may not be necessary for many cell lines [29].

In hMSCs cultivation, glutamine decreases mostly due to spontaneous degradation. In addition, the estimated specific glutamine reaction rate resulted in production of glutamine instead of consumption by hMSCs. This, however, does not mean that hMSCs do not consume any glutamine at all; it means that the net effect for the

investigated period can best be described by glutamine production by hMSCs. One possibility is that glutamate production at the beginning of culture is the result of glutamine consumed significantly during the initial phase, but produced thereafter. The results suggest that there is little contribution of glutamine to the production of lactate as reflected by the ratio $Y_{l/g}$ and glutamine dynamics q_q (Except for donor 1 when seeded at 100 cells/cm²). In future studies, glutamine metabolism in hMSCs cultures should become clearer by obtaining experimental data of, for example, hMSCs growth in glutamine-free medium.

At 100 cells/cm², both q_q and q_e were higher than the respective values at 1000 cells/cm² with the exception of donor 1 (Fig. 7, table 4). This suggested a higher metabolic rate for these amino acids when seeding at 100 cells/cm². As described in the sub-section above, we speculate that this result is related to the gradual onset of contact inhibition and identifiable via the ten-fold seeding density difference.

The glutamine and glutamate mathematical models showed that amino acid metabolism needs to be studied in far more detail. The mathematical model suggests that production of glutamine and glutamate fluctuate during the culture period. This suggests faster reaction kinetics than glucose kinetics and metabolic shifts that could be important for understanding hMSCs growth *in vitro*.

During cultivation, glutamate production occurred possibly due to its role as an intermediate in not only glutamine, but also proline, histidine and arginine metabolism [13]. After initial glutamate production, measurements showed that changes in amino acid metabolism could not be described with the mathematical model assumptions on equation (4). It is known that hMSCs gene expression varies from proliferation on day two to development on day seven in culture [30]. In addition, evidence suggests that glutamate is a signalling molecule in many tissues: Central nervous system, spleen, bone, pancreas, lung, heart, liver, kidney, stomach, intestine and testis [31]. Therefore, we think that glutamine and glutamate kinetics shifts could be linked to hMSCs change of phenotype in culture. Since kinetic mathematical models require information from the stoichiometry of the reactions [32], more quantitative amino acid data are needed to explore the mechanisms involved in hMSCs growth and amino acid metabolism.

4. Mathematical model

The mathematical model was based on mass balances and produces the course of the cell number and concentrations as a function in time. The estimation of biomass and amino acid metabolism was not optimal. However, the fit or lack thereof of the mathematical model allowed us to identify growth and metabolism characteristics

not identified before. To cope with systematic deviations, an extension of the mathematical model could be considered. Extension of the mathematical model, however, implies the introduction of extra parameters. This in turn results in larger confidence intervals and less meaningful parameters. Due to the challenge ahead of using or developing a systems approach to understand hMSCs biology, we extended the model as much as the experimental data allowed. Herewith we agree with the iterative nature of mathematical modelling as stated by MacArtur and Oreffo (2005).

Conclusions

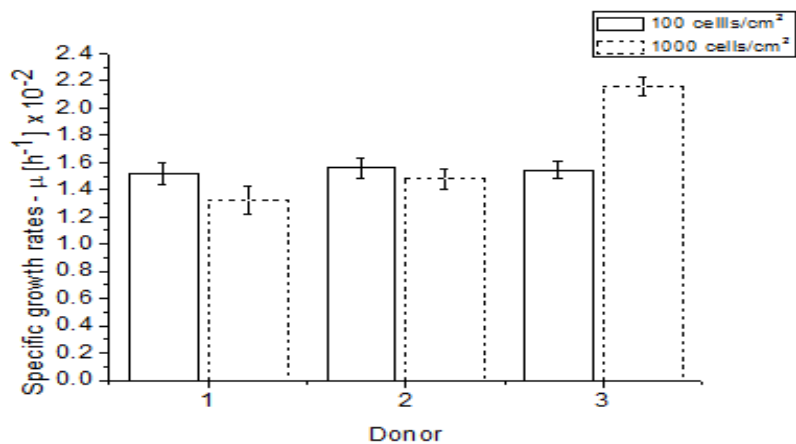
We have used a mathematical model to quantitatively investigate mechanisms for hMSCs growth and metabolism in a T-25 flask when seeding at 100 and 1000 cells/cm². With the mathematical model, growth rates were estimated for three donors; however, the mathematical modelling results showed that rate-limiting substrates and concentrations need to be addressed in order to obtain a clearer understanding on the mechanisms involved in hMSCs growth *in vitro*. On the other hand, glucose and lactate mathematical model results showed consistent results in the three donors, suggesting anaerobic glycolysis and a higher rate of reaction at 100 cells/cm². Furthermore, glutamine could be produced instead of consumed by hMSCs during part of the culture period. Glutamine and glutamate rates of production were higher at 100 cells/cm². Higher metabolic rates could be induced by a lower contact inhibition effect when seeding at 100 cells/cm² than when seeding at 1000 cells/cm². Furthermore, glutamine and glutamate kinetics were partially described and significant metabolic shifts were identified. Data on other amino acids is necessary to investigate these metabolic shifts. This work is an example of the use of mathematical models for investigating the mechanisms behind hMSCs growth and metabolism.

References

1. MacArthur, B.D. and R.O.C. Oreffo, Bridging the Gap. *Nature*. 433: p. 19, 2005.
2. Prockop, D., Marrow Stromal Cells as Stem Cells for Nonhematopoietic Tissues. *Science*. (276): p. 71 - 74, 1997.
3. Pittenger, M., A. Mackay, S. Beck, R. Jaiswal, R. Douglas, J. Mosca, M. Moorman, D. Simonetti, S. Craig, and D. Marshak, Multilineage Potential of Adult Human Mesenchymal Stem Cells *Science*. (284): p. 143 - 147, 1999.
4. Caplan, A. and S. Bruder, Mesenchymal Stem Cells: Building Blocks for Molecular medicine in the 21st Century. *trends. Mol. Med.* (7): p. 259 - 264, 2001.
5. Braccini, A., D. Wendt, J. Farhadi, S. Schaeren, M. Heberer, and I. Martin, The Osteogenicity of Implanted Engineered Bone Constructs is related to the Density of Clonogenic Bone Marrow Stromal Cells. *Journal of Tissue Engineering and Regenerative Medicine*. 1(1): p. 60 - 65, 2007.
6. Schop, D., F.W. Janssen, E. Borgart, J.D.d. Bruijn, and R.v. Dijkhuizen-Radersma, Expansion of Mesenchymal Stem Cells Using a Microcarrier Based Cultivation System: Growth and Metabolism. *Journal of Tissue Engineering and Regenerative Medicine*. 2(2 - 3): p. 126 - 35, 2008.
7. Kontoravdi, C., D. Wong, C. Lam, Y.Y. lee, M.G.S. Yap, E.N. Pistikopoulos, and A. Mantalaris, Modeling Amino Acid Metabolism in Mammalian Cells Toward the Development of a Model Library. *Biotechnol. Prog.* 23(6): p. 1261 - 9, 2007.
8. Mohler, L., A. Bock, and U. Reichl, Segregated Mathematical Model for Growth of Anchorage-dependant MDCK Cells in Microcarrier Culture *Biotechnol. Prog.* 24(1): p. 110-119, 2008.
9. Sidoli, F.R., A. Mantalaris, and S.P. Asprey, Modelling of Mammalian Cells and Cell Culture Processes. *Cytotechnology*. (44): p. 27 - 46, 2004.
10. Zhao, F., P. Pathi, W. Grayson, Q. Xing, B.R. Locke, and T. Ma, Effects of oxygen transport on 3-D human mesenchymal stem cell metabolic activity in perfusion and static cultures: Experiments and mathematical model. *Biotechnol. Prog.* 21: p. 1269-1280, 2005.
11. Lemon, G., S.L. Walters, F.R.A.J. Rose, and J.R. King, Mathematical modelling of human mesenchymal stem cell proliferation and differentiation inside artificial porous scaffolds. *Journal of Theoretical Biology*. (249): p. 543 - 553, 2007.
12. Rich, P., The Molecular Machinery of Keilin's Respiratory Chain. *Biochemical Society Transactions*. 31(6): p. 1095 - 1105, 2003.
13. Stryer, L., Amino acid degradation and the urea cycle. *Biochemistry*. New York. W.H. Freeman and Company. 629 - 652, 1995.
14. Glacken, M., Catabolic control of Mammalian Cell Culture *Biotechnology*. 6: p. 1041 - 1050, 1988.
15. Colter, D.C., R. Class, C.M. DiGirolamo, and D.J. Prockop, Rapid Expansion of Recycling Stem Cells in Cultures of Plastic -adherent Cells from Human Bone

- Marrow PNAS. 97(7): p. 3113 - 3218, 2000.
16. Colter, D.C., I. Sekiya, and D.J. Prockop, Identification of a Subpopulation of Rapidly Self-renewing and Multipotential adult Stem Cells in Colonies of Human Marrow Stromal Cells PNAS. 98(14): p. 7841 - 7845, 2001.
 17. Sekiya, I., B.L. Larson, J.R. Smith, R. Pochampally, J.-G. Cui, and D.J. Prockop, Expansion of Human Adult Stem Cells from Bone Marrow Stroma: Conditions that Maximize the Yields of Early Progenitors and Evaluate their Quality. *Stem Cells*. 20: p. 530 - 541, 2002.
 18. Sotiropoulou, P.A., S.A. Perez, M. Salagianni, C.N. Baxevanis, and M. Papamichail, Characterisation of the Optimal Culture Conditions for Clinical Scale Production of Human Mesenchymal Stem Cells. *Stem Cells*. 24: p. 462 - 471, 2006.
 19. Both, S.K., A.J.C.v.d. Muijsenberg, C.A.v. Blitterswijk, J.d. Boer, and J.D.d. Bruijn, A Rapid and Efficient Method for Expansion of Human Mesenchymal Stem Cells *Tissue Engineering*. 13(1): p. 3 - 9, 2007.
 20. Tritsch, G.L. and G.E. Moore, Spontaneous decomposition of glutamine in cell culture media. *Experimental Cell Research*. (28): p. 360-364, 1962.
 21. Frame, K.K. and W.S. Hu, A Model for Density-Dependent Growth of Anchorage Dependent Mammalian-Cells. *Biotechnology and Bioengineering*. 32(8): p. 1061 - 1066, 1988.
 22. Cruz, H.J., J.L. Moreira, and M.J. Carrondo, Metabolic Shifts by Nutrient Manipulation in Continuous Cultures of BHK Cells. *Biotechnol. and Bioeng.* 66(2): p. 104 - 113, 1999.
 23. Schop, D., F. Janssen, L.v. Rijn, H. Fernandes, J.d. Bruijn, and R.v. Dijkhuizen-Radersma, Growth, Metabolism and Growth Inhibitors of Mesenchymal Stem Cells. Publication in preparation.
 24. Bailey, J.E. and D.F. Ollis, Kinetics of substrate utilization, product formation, and biomass production in cell cultures. *Biochemical Engineering Fundamentals*. MacGraw-Hill Book Company. 984, 1986.
 25. Gregory, C.A., H. Singh, A.S. Perry, and D.J. Prockopp, The Wnt Signalling Inhibitor Dickkopf-1 is required for Reentry into the Cell Cycle of Human Adult stem Cells from Bone Marrow. *The Journal of Biological Chemistry*. 278(30): p. 28067 - 28078, 2003.
 26. Alberts, B., A. Johnson, J. Lewis, M. Raff, K. Roberts, and P. Walter. *Molecular Biology of the Cell*. New York. Garland Science. 1268, 2008.
 27. Neu, J., V. Shenoy, and R. Chakrabarti, Glutamine Nutrition and Metabolism: Where do We Go from Here? *FASEB J*. 10: p. 829 - 837, 1996.
 28. Bode, B.P., Recent Molecular Advances in Mammalian Glutamine Transport. *Journal of Nutrition*. 131(9S): p. 2475 - 85, 2001.
 29. Masters, J.R. and G.N. Stacey, Changing medium and passaging cell lines *Nature Protocols*. 2(9): p. 2276-2284, 2007.

30. Larson, B.L., J. Ylostalo, and D.J. Prockop, Human multipotent stromal cells undergo sharp transition from division to development in culture. *Stem Cells*. 26(1): p. 193-201, 2008.
31. Skerry, T.M. and P.G. Genever, Glutamate signalling in non-neuronal tissues. *Trends in Pharmacological Sciences*. 22(4): p. 174-181, 2001.
32. Dunn, I.J., E. Heinzle, J. Ingham, and J.E. Prenosil, *Modelling Principles. Biological Reaction Engineering: Dynamic modelling fundamentals with simulation examples* Weinheim. Wiley-VCH. 9 - 53, 2003.



Erratum: Figure 2 Bar plot shows for the three donors the estimated specific growth rates and their 95 % confidence interval when seeding at 100 cells/cm² (—) or at 1000 cells/cm² (---).

Chapter 2

Patterns of Amino Acid Metabolism by Proliferating Human Mesenchymal Stem Cells

Gustavo A. Higuera¹, Deborah Schop², Riemke van Dijkhuizen-Radersma^{2,3,a}, Madelon Bracke², Dirk Martens⁴, Joost D.de Bruijn^{2,3,5}, Marcel Karperien¹, Anton van Boxtel⁶, and Clemens A. van Blitterswijk¹

¹Department of Tissue Regeneration, Institute for Biomedical Technology, University of Twente, Enschede, The Netherlands.

²Xpand Biotechnology BV, Bilthoven, The Netherlands

³Progentix Orthobiology BV, Bilthoven, The Netherlands

⁴Bioprocess Engineering Group, Department of Agrotechnology and Food Sciences, Wageningen University, The Netherlands.

⁵Queen Mary University of London, UK

⁶Systems and Control Group, Wageningen University, Wageningen, The Netherlands.

^aCurrent address: Genmab BV, Utrecht, The Netherlands

Abstract

Kinetics provides a biophysical context to understand the behaviour of human mesenchymal stem cells (hMSCs) in different environments. hMSCs proliferation is necessary to implement stem-cell based clinical applications. Consumption and production by hMSCs of extracellular components, such as, amino acids remains largely unexplored. Which amino acids are consumed or produced by hMSCs is not clear. This is important to control and understand hMSCs behavior *in vitro*. Here, amino acid metabolism by hMSCs was studied. 20 amino acids were measured and analyzed with a growth and metabolism kinetics model. First, hMSCs cultured on tissue culture plastic showed that 16 out of 20 amino acids had a strong consumption or production behavior. We hypothesized that some amino acids would present a similar metabolic pattern in other culture conditions. Remarkably, hMSCs cultured on microcarriers in a stirring vessel bioreactor showed that 19 amino acids had a consumption or production behaviour. Despite differences in both culture conditions with respect to shear stress, cell-attachment material, seeding density and donor variation, we concluded that both conditions shared 14 amino acids with similar kinetic patterns. Of this 14, 11 were consumed and 3 were produced by hMSCs in both static and dynamic conditions, thus revealing a common amino acid metabolic pathway for proliferating hMSCs. In addition, 6 amino acids showed trends sensitive to culture conditions. In static cultures, the most and the least consumed amino acids

were leucine and methionine, respectively. In dynamic culture, the most and least consumed amino acids were isoleucine and histidine, respectively. The most and least produced amino acids in both static and dynamic conditions were ornithine and glycine, respectively. These results show that there is an amino acid fingerprint of proliferating hMSCs. This can determine the components and quantities required for designing a medium without serum additives. It is also a foundation for future metabolic flux analysis and energy management by hMSCs. These can stimulate the discovery of basic knowledge and medical applications of stem cells.

Introduction

Human mesenchymal stem cells (hMSCs) proliferation *in vitro* is necessary since these cells are present in low numbers in the body [1]. Consequently, proliferation has been the focus of many studies in tissue culture plastic [2-4] and in bioreactors [5-8]. Stem cells from the bone marrow are used in gene, cell, and tissue therapies [9-12] because of their potential to differentiate into multiple cell lineages and form bone, cartilage, muscle, fat, ligament and tendon tissues [13-16]. Yet, little is known about how hMSCs use resources such as amino acids [17] and extracellular compounds [18] during proliferation.

Basic understanding of amino acid metabolism has been crucial in achieving successful and robust proliferation of cell cultures [19-22]. Because amino acids are fundamental factors in nutrition, DNA synthesis and protein production [23], amino acid metabolism has been essential to robustly produce vaccines and antibodies [20, 21, 24]. In stem cell research, it can be vital to understand how phenotype changes and differentiation occur [25, 26]. In addition, it can rationalize the design of medium compositions [19] and explore the production of complex molecules, such as extracellular matrix components.

We hypothesized that there could be amino acids that have similar consumption/production kinetics independently of culture conditions, thus of importance in stem cell nutrition and physiology. This hypothesis was tested by culturing human mesenchymal stem cells (hMSCs) on tissue culture plastic (static condition); and on micro-carriers in a stirring vessel bioreactor [27] (dynamic condition). In both static and dynamic conditions, 20 amino acids were measured in time. A growth and metabolism kinetics model [24, 28] was used to analyze amino acid data of different human donors in both proliferation systems. Surprisingly, out of the 20 amino acids measured, hMSCs consumed 11 amino acids and produced 3 amino acids consistently in both static and dynamic conditions.

Materials and Methods

Isolation and cryopreservation of hMSCs

Isolation and cryopreservation of hMSCs were performed as described previously [29]. After informed consent and approval by the medical ethical committee, we obtained hMSCs from the acetabulum of 5 human donors who were undergoing total hip replacement surgery. Gender and donor age were as follows: Donor 1: Female, 81 years. Donor 2: Male, 65 years. Donor 3: Female, 76 years. Donor 4: Female, 68 years. Donor 5: Female, 38 years. The human MSCs population was isolated from the aspirates via adhesion selection. Cells were cultured up to passage 1 and cryopreserved. Experiments were performed according to protocols previously described for tissue culture plastic (Static) [29] or microcarriers in a stirring vessel bioreactor (Dynamic) [8]. Culture medium was prepared according to static or dynamic conditions as follows:

Static: The α MEM proliferation medium contained minimal essential medium (GIBCO, Carlsbad, CA), 10% fetal bovine serum of a selected batch (FBS lot:4SB0010; Biowhittaker), 1ng/ml basic fibroblast growth factor (Instruchemie, Delfzijl, The Netherlands), penicillin G (100 Units/ml, Invitrogen), 0.2mM l-ascorbic-acid-2-phosphate (Sigma, St Louis, MO), streptomycin (100 μ g/ml, Invitrogen), and 2mM l-glutamine (Sigma, Zwijndrecht, The Netherlands).

Dynamic: Culture medium used consisted of α -MEM (Invitrogen, Breda, The Netherlands) supplemented with 15% FBS (FBS, Cambrex, Verviers, Belgium), 100 U/ml penicillin, 100 μ g/ml streptomycin, 2 mM L-glutamine (Invitrogen), 0.2 mM L-ascorbic acid-2-phosphate, 1 ng/ml bFGF (AbD Serotec, Oxford, UK), and 10 nM dexamethasone (Sigma).

Proliferation

Static: Donors 1 to 3 were cultured. Proliferation of hMSCs was performed on tissue culture plastic (T-Flasks, Nunc, Denmark) in a standard incubator with controlled temperature (37°C) and humidified atmosphere with 5% CO₂. Cryopreserved hMSCs were thawed, counted, and plated—passage 2—at 100 cells/cm² in α MEM proliferation media in tissue culture flasks (T-flasks). α MEM proliferation medium was not refreshed to maintain a batch culture configuration. Every day, three replicates were sacrificed to obtain cell numbers and the conditioned medium.

Dynamic: Donors 4 and 5 were cultured. Proliferation of human mesenchymal stem cells hMSCs was performed in 1-liter round-bottomed stirred vessel bioreactors (Applikon Biotechnology BV, Schiedam, The Netherlands) on Cytodex type 1

microcarriers (GE Healthcare, Diegem, Belgium) at a density of 20 cm²/ml (4.5 g/l) [8]. During cultivation, the following conditions were regulated with an ez-Control (Applikon Biotechnology):

- Temperature controlled at 37°C.
- Agitation speed controlled at 50 rpm during seeding and at 70-60 rpm during expansion using a marine impeller.
- pH regulated at 7.3 using 0.25 M NaOH and CO₂ gas.
- Dissolved oxygen concentration (DO) controlled at 4% O₂ saturation by adjusting the oxygen fraction (using N₂ and/or air gasses) blown over the surface of the cultures.

The hMSCs were seeded on the microcarriers at 3000 cells/cm² in 400 ml proliferation medium without FBS [8]. The suspension was stirred at 50 rpm for 4 hours. After the seeding period, the medium was refreshed for 50% and FBS was added to obtain a final concentration of 15% FBS. During 7 days of cell expansion, the culture was stirred at 70 rpm. Daily samples were taken for cell analysis and medium analysis. Because the medium level decreased over time due to sampling, the stirring rate was decreased stepwise to 60 rpm to maintain a homogeneous microcarrier suspension with comparable shear forces. Two separate experiments were performed (n=2) for each of the donors cultured in the bioreactor system.

Cell numbers

Static: To harvest cells, the T-flasks were washed with PBS (Sigma) and hMSCs were enzymatically detached from T-flasks with 0.25% trypsin/EDTA. From the cell suspension, 200 µl were diluted in 10 ml of Isoton II diluent (Beckman Coulter, Fullerton, CA) and three drops of Zap-OGlobin II lytic reagent (Beckman Coulter) were added. The solutions were incubated for 30 min to maximize the effect of the lytic reagent, and subsequently, the nuclei of cells were counted in a particle count and size analyzer (Z2, Beckman Coulter). The size range of counted nuclei was set to between 6 to 10.5 µm according to the 95 % confidence interval of hMSCs nuclei size.

Dynamic: Sampling of microcarriers was performed during the bioreactor runs. From these samples, viable cell numbers were measured using the CellTiter-Glo assay (Promega), which is based on metabolic activity of the cell. To visualize the cell load and cell distribution on the microcarriers, cells were stained with 1% 3-(4,5-dimethylthiazol-2-yl)-2,5-diphenyltetrazolium bromide (MTT) solution (Merck, Schiphol-Rijk, The Netherlands).

Metabolites and volume

Glucose and lactate were measured in a Vitros DT60 II chemistry system (Ortho-Clinical Diagnostics). Daily measurements were performed for every donor from

independent medium samples in both static and dynamic cultures.

Static: The medium evaporated at rate of 2.1×10^{-3} ml/h ($\pm 2.1 \times 10^{-4}$, n = 3) in incubators at 37 Celsius with 60% relative humidity. Concentrations measured were normalized to the volume changes.

Dynamic: Daily, 10-20 ml microcarrier-cell and medium samples were taken aseptically from the cell cultures in the stirred vessels. This resulted in the working volume changing from 400 ml to 300 ml during culture.

Amino acid analysis

Free amino acid concentrations in the medium samples were determined by HPLC chromatography and performed by Ansynth Service B.V. (Roosendaal, The Netherlands).

Static: From each donor, three T-flasks were sacrificed to obtain medium samples every day. Medium samples were filtered (0.2 μ m pore size, Millipore, The Netherlands). Each amino acid measurement is representative of mixing medium samples from 3 T-flasks. Immediately afterwards, vials were stored at -80 °C.

Dynamic: Medium samples from each bioreactor were filtered and stored at -80°C.

Estimation of degradation kinetics.

Degradation experiments included medium incubated without cells in static and dynamic culture. Medium samples were obtained and metabolites and amino acids were measured with their respective methods. First order degradation kinetics were assumed during analysis. Amino acids with significant degradation are shown on Table 1.

Table 1 Amino acids with significant degradation rates in static and dynamic cultures.

	[h ⁻¹]	Static			Dynamic		
		x 10 ⁻³ (n=10)	SD x 10 ⁻³	r ²	x 10 ⁻³ (n=7)	SD x 10 ⁻³	r ²
Arginine	k _r	1.20	0.7	0.80	2.60	1.30	0.83
Aspartate	k _d	1.10	0.7	0.74	2.10	1.00	0.83
Asparagine	k _n	1.30	0.6	0.86	1.80	1.30	0.71
Glutamine	k _q	3.30	0.7	0.96	3.00	1.20	0.86
Ornithine	K _o	5.70	1.80	0.89	7.30	3.60	0.79

Statistical Analysis

Each data point of cell numbers, glucose and lactate concentrations was obtained from three replicates (3 T-Flasks/Donor and 3 donors) or two parallel runs (2 stirring vessels and two donors). Error bars in graphs with experimental data represent the standard deviation of measurements. Analysis of growth and metabolism kinetics was performed and evaluated on the basis of 95% confidence intervals with the growth and kinetics model found below.

Growth and Metabolism Kinetics Model Description

To determine amino acid used by hMSCs, static and dynamic culture were described with the mass balances of the variables measured. Cell numbers, metabolites, and amino acid data were analyzed with the sets of differential equations described below.

Static experiments:

$$\frac{dX_v}{dt} = \mu \cdot X_v \quad (1)$$

Where, $\mu = \mu_v - \mu_d$

Eq. (1) describes the change of viable cells in time in T-flasks, where X_v [Total] is the viable cell number, μ [h⁻¹] is the specific growth rate, μ_v [h⁻¹] is the specific growth rate of viable cells and μ_d [h⁻¹] is the death rate of viable cells. μ_v and μ_d cannot be estimated as independent variable and therefore μ was estimated and used to predict viable cell numbers.

$$\frac{dX_m}{dt} = q_m \cdot X_v - k_{dm} \cdot X_m \quad (2)$$

Eq. (2) presents the change of amino acids, glucose and lactate in time, where X_m is in moles of m and the subscript m refers to metabolites or amino acids, q_m

refers to the specific consumption/production rate [moles/cell/h]. q_m is constant and is negative for consumed molecules and positive for produced molecules, k_{dm} represents the first order spontaneous degradation constant which is dependent on the amount of compound X_m .

Dynamic experiments:

During the dynamic experiments the volume of the reactor changes due to sampling. The changing volume is given by:

$$\frac{dV}{dt} = -B \quad (3)$$

with V as the changing bioreactor volume in time and B is the bleed due to sampling of the bioreactor [ml/h]. $B=0.56$ ml/h from medium sampling.

$$\frac{dX_v}{dt} = \left(\mu - \frac{B}{V}\right) \cdot X_v \quad (4)$$

Eq. (4) describes the change of viable cells in time in the bioreactor.

$$\frac{dX_m}{dt} = q_m \cdot X_v - \left(k_{dm} + \frac{B}{V}\right) \cdot X_m \quad (5)$$

Eq. (5) describes the change of amino acids, glucose and lactate in the bioreactor.

Parameter estimation

The metabolite concentrations depend both on production/consumption and degradation. By using the kinetics model equations 1 through 5 the contributions consumption/production and degradation to the metabolite concentrations can be separated. The ordinary differential equations (ODEs) 1 through 5 were solved with a standard differential equation solver in Matlab (ode45 in version 7.0.4 release 2007a; Mathworks, Natick, MA) on a windows-based system. The initial values for solving the differential equations were set to the experimentally determined seeding densities and amounts of measured molecules in fresh α MEM proliferation medium from three samples. Growth and metabolism kinetics parameters were obtained by nonlinear least squares regression which minimizes the sum of the quadratic error over an experiment (Matlab function `nlfit`). The 95 % confidence intervals for the parameters were calculated (Matlab function `nlparci`).

Extended Kalman Filter

Cell proliferation can be defined by a constant specific growth rate (Eq 1).

However, cells may proliferate with changing specific growth rates over time. If cells have such behavior, then the uptake and release of metabolites follows the proliferation pattern. Therefore, a methodology that elucidates varying specific growth rates and consequently changing metabolism was considered. To reveal varying specific growth rates the Extended Kalman Filter was adopted from previous studies [30, 31] to estimate cell numbers and specific growth rates (Eq. 6 and 7).

$$\frac{dX_v}{dt} = \mu \cdot X_v + w_{X_v} \quad (6)$$

Equation (6) describes the change of the total number of viable cells with time in a differential equation form and includes both cell growth ($\mu \cdot X_v$) and its covariance w_{X_v} , where μ is the specific growth rate [h⁻¹] and X_v is the cell number [total] both changing in time.

$$\frac{d\mu}{dt} = 0 + w_{\mu} \quad (7)$$

Eq. 7 is defined as the change of μ in time, where w_{μ} is the covariance of μ .

Eq. 6 and 7 were updated from *a priori* to *a posteriori* estimate with the equations composing the extended kalman filter (EKF) on Fig. 1. Tuning of the EKF was performed by minimization of the squared sum of experimental minus predicted cell number data. After obtaining fit for cell numbers with Eqs. 6 and 7, amino acid rates were estimated with Eq. 2.

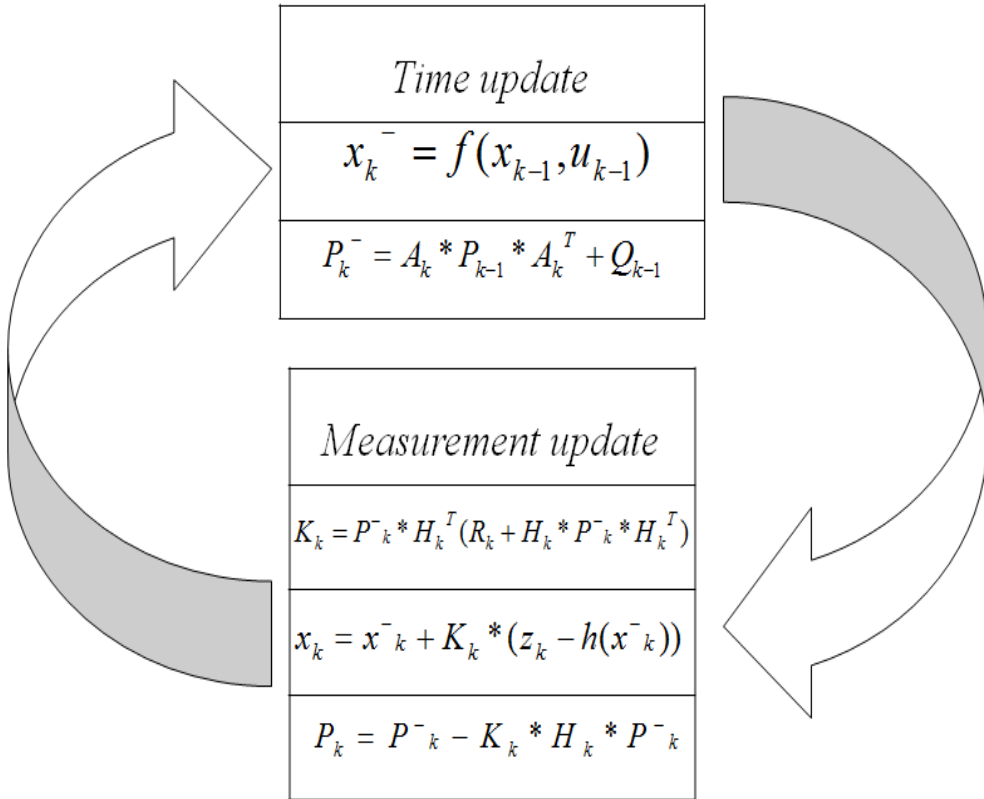


Figure 1 Extended Kalman Filter representation.

Results

Growth and kinetics in Static Culture

Proliferation studies in static cultures have already provided a broad biological understanding of hMSCs activity *in vitro* [2, 25, 26]. Therefore, this study considered growth and amino acid metabolism in static conditions. In the analysis, two options were considered. The first one is with a **constant** specific growth rate. Thus, cell numbers were analysed with growth model equation 1 (Fig. 2A). The fit was acceptable, but between 96-192 hours the cell numbers were underestimated.

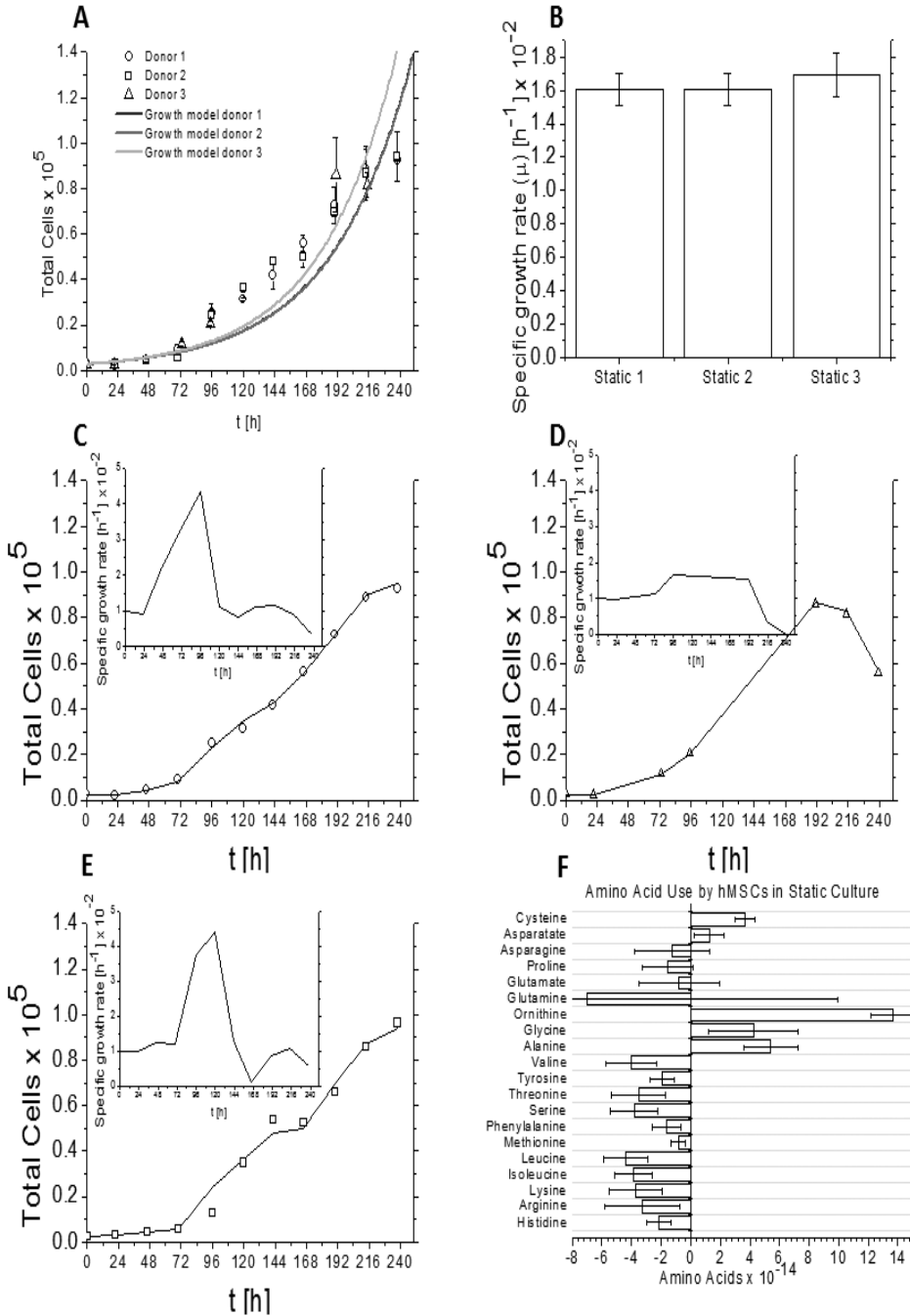


Figure 2 **A**: Cell numbers and growth model fit (—). **B**: Bar plot of specific growth rates of cells in static culture. **C D E**: Total cell numbers for three donors (○ - C, □ - D and △ - E) and EKF (—) result. Embedded within each fit, μ and Eq. 3 prediction for each donor (C – E). **F**: Amino acid use by hMSCs in static culture. Mean and error bars for each amino acid are representative of 3 donors.

Therefore, option two a **varying** specific growth rate in time was considered to obtain a better fit for cell numbers and a realistic representation of the growth phases (Lag, exponential, plateau). The cell number fit improved in the data of the three hMSCs donors (Fig. 2C-D). However, analysis of all metabolic data in time with the varying specific growth rate did not result in more accurate fits, better correlation, or more accurate amino acid metabolic rates (Table 2). Out of 23 rates estimated from data for three human donors, only 4 estimates improved significantly due to a varying specific growth rates. Therefore, the presented data analysis is based on constant specific growth rates, which were estimated for each donor (Fig. 2B, table 3). Specific growth rates corresponded to the magnitude of values found in literature [28, 32].

Table 2 Amino Acid Rates with Constant and Varying Specific Growth Rates: Standard error of estimates (SEE) of fits and statistical significance for data of three hMSCs donors.

	Static 1			Static 2			Static 3								
	constant μ variable μ			constant μ variable μ			constant μ variable μ								
	SEE1	SEE2	SEE1 < SEE2 p < 0,05 variable μ	SEE1	SEE2	SEE1 < SEE2 p < 0,05 variable μ	SEE1	SEE2	SEE1 < SEE2 p < 0,05 variable μ						
Glucose	4.14E-07	3.21E-07	1	TRUE	3.13E-07	2.10E-07	1	TRUE	6.38E-07	1.06E-06	0	1	FALSE		
Lactate	2.77E-07	1.40E-07	1	TRUE	2.41E-07	1.20E-07	1	TRUE	1.41E-06	7.19E-07	1	1	TRUE		
Glutamine	8.98E-07	9.02E-07	0	FALSE	3.94E-07	4.19E-07	0	FALSE	5.68E-07	5.81E-07	0	0	FALSE		
Glutamate	1.76E-07	1.79E-07	0	FALSE	1.27E-07	1.30E-07	0	FALSE	1.95E-07	1.99E-07	0	0	FALSE		
Histidine	5.66E-08	5.50E-08	1	FALSE	2.91E-08	3.28E-08	0	FALSE	7.54E-08	7.53E-08	1	0	FALSE		
Proline	1.10E-07	1.10E-07	0	FALSE	8.37E-08	8.62E-08	0	FALSE	1.50E-07	1.55E-07	0	0	FALSE		
Arginine	1.39E-07	1.38E-07	1	FALSE	9.87E-08	1.04E-07	0	FALSE	1.91E-07	1.94E-07	0	0	FALSE		
Lysine	1.18E-07	1.16E-07	1	FALSE	6.94E-08	7.47E-08	0	FALSE	1.38E-07	1.43E-07	0	0	FALSE		
Alanine	1.32E-07	1.33E-07	0	FALSE	1.74E-07	1.07E-07	1	TRUE	1.36E-07	1.27E-07	1	1	TRUE		
Asparagine	8.94E-08	9.07E-08	0	FALSE	6.40E-08	6.34E-08	1	FALSE	9.76E-08	1.01E-07	0	0	FALSE		
Aspartate	8.11E-08	8.18E-08	0	FALSE	8.34E-08	8.25E-08	1	FALSE	7.22E-08	6.94E-08	1	0	FALSE		
Cysteine	7.92E-08	3.57E-08	1	TRUE	9.96E-08	5.04E-08	1	TRUE	1.14E-07	7.04E-08	1	1	TRUE		
Glycine	2.04E-07	2.03E-07	1	FALSE	1.29E-07	1.31E-07	0	FALSE	2.45E-07	2.51E-07	0	0	FALSE		
Isoleucine	1.14E-07	1.11E-07	1	FALSE	7.44E-08	8.01E-08	0	FALSE	1.11E-07	1.16E-07	0	0	FALSE		
Leucine	1.22E-07	1.19E-07	1	FALSE	8.02E-08	8.57E-08	0	FALSE	1.18E-07	1.24E-07	0	1	FALSE		
Methionine	2.96E-08	2.92E-08	1	FALSE	1.92E-08	2.04E-08	0	FALSE	2.85E-08	2.91E-08	0	0	FALSE		
Phenylalanine	5.90E-08	5.83E-08	1	FALSE	4.26E-08	4.48E-08	0	FALSE	6.71E-08	7.00E-08	0	0	FALSE		
Serine	7.65E-08	7.40E-08	1	FALSE	3.23E-08	3.78E-08	0	FALSE	7.64E-08	8.43E-08	0	1	FALSE		
Threonine	1.26E-07	1.24E-07	1	FALSE	7.28E-08	7.95E-08	0	FALSE	1.42E-07	1.47E-07	0	0	FALSE		
Tyrosine	5.96E-08	5.83E-08	1	FALSE	5.70E-08	5.83E-08	0	FALSE	9.17E-08	9.25E-08	0	0	FALSE		
Valine	1.24E-07	1.21E-07	1	FALSE	6.16E-08	6.89E-08	0	FALSE	1.32E-07	1.37E-07	0	0	FALSE		
Ornithine	1.65E-07	4.65E-08	1	TRUE	1.95E-07	2.26E-08	1	TRUE	1.64E-07	3.31E-08	1	1	TRUE		
Average	1.66E-07	1.48E-07	16	4	4	1.16E-07	9.59E-08	7	16	5	2.25E-07	2.08E-07	6	7	4

With the specific growth rates estimated for each donor, the kinetics model was used to analyze glucose and lactate data in static conditions. Glucose and lactate in static conditions were used to test the growth and kinetics model. Glucose and lactate showed consumption and production trends, respectively. The kinetics model equation 2 was used to estimate the glucose and lactate reaction rates (Table 3), which were similar to values found in literature [28, 32].

Table 3 Specific growth rates and glucose and lactate metabolic rates in static (3 donors) and dynamic (2 donors) cultures.

		Static							Dynamic				
		1	SD	2	SD	3	SD	Mean (n=3)	1	SD	2	SD	Mean (n=2)
Cells	μ [h ⁻¹] x 10 ⁻²	1.61	0.09	1.61	0.09	1.48	0.26	1.56	1.09	0.19	1.17	0.14	1.13
Glucose	q_{gluc} [moles/cell/h] x10 ⁻¹⁴	-64.50	9.74	-74.93	7.42	-93.73	15.49	-77.72	-58.09	2.26	-64.50	4.87	-61.30
Lactate	q_{lac} [moles/cell/h] x10 ⁻¹⁴	103.22	6.51	110.23	5.71	209.11	34.26	140.85	142.79	6.90	115.00	6.60	128.90

The growth and kinetics model equations 1 and 2 were then used to estimate the production/consumption rates of amino acid data obtained from hMSCs in static conditions. Fig. 2D shows the mean production rates of 3 donors in static culture as presented on Table 4. This showed that alanine, aspartate, cysteine, glycine and ornithine were produced by all hMSCs donors in static conditions (Fig. 2D). Similarly, arginine, histidine, isoleucine, leucine, lysine, methionine, phenylalanine, serine, threonine, tyrosine and valine were consumed by all hMSCs donors in static conditions (Fig. 2D). In addition, asparagine, glutamate, glutamine and proline did not show a definite trend (Fig. 2D).

Table 4 Amino Acid Metabolic Rates in Static Cultures.

	[moles/cell/h] x10 ⁻¹⁴	Consumption							
		1	SD	2	SD	3	SD	Mean (n=3)	SD
Histidine	q_h	-1.19	1.33	-2.45	0.69	-2.72	1.83	-2.12	0.82
Arginine	q_r	-0.49	3.47	-3.91	2.48	-5.48	4.91	-3.30	2.55
Lysine	q_k	-1.65	2.78	-4.61	1.64	-4.90	3.34	-3.72	1.80
Isoleucine	q_i	-2.38	2.67	-4.59	0.18	-4.62	2.70	-3.86	1.29
Leucine	q_l	-2.69	2.88	-4.95	1.90	-5.53	2.85	-4.39	1.50
Methionine	q_m	-0.33	0.70	-0.87	0.45	-1.32	0.69	-0.84	0.49
Phenylalanine	q_f	-0.56	1.39	-2.07	1.01	-2.35	1.63	-1.66	0.96
Serine	q_s	-2.13	1.80	-4.00	0.76	-5.36	1.85	-3.83	1.62
Threonine	q_t	-1.47	2.96	-4.22	1.72	-4.91	3.44	-3.53	1.82
Tyrosine	q_y	-0.99	1.40	-2.29	1.35	-2.57	2.22	-1.95	0.84
Valine	q_v	-2.03	2.91	-4.94	1.46	-5.08	3.20	-4.02	1.72
		Production							
Alanine	q_a	7.53	3.12	4.53	4.12	4.20	3.29	5.42	1.84
Glycine	q_g	0.75	4.80	5.60	3.06	6.35	5.93	4.24	3.04
Ornithine	q_o	15.03	5.13	13.83	6.11	12.06	5.24	13.64	1.49
		Indefinite							
Glutamine	q_q	7.81	25.05	-25.54	11.05	-3.38	16.27	-7.04	16.97
Glutamate	q_e	2.26	4.14	-3.02	3.00	-1.64	4.74	-0.80	2.73
Proline	q_p	0.24	2.58	-1.81	1.98	-3.15	3.63	-1.57	1.71
Asparagine	q_n	1.42	2.26	-3.59	1.63	-1.69	2.54	-1.29	2.53
Asparatate	q_d	2.41	2.03	0.78	2.10	0.52	1.86	1.24	1.02
Cysteine	q_c	4.44	1.86	3.40	2.36	3.15	2.77	3.66	0.69

Alanine is shown here as the representative produced amino acid by hMSCs in static culture (Fig. 3A-B). There was a strong production trend in all donors, despite a poor fit with alanine data as reflected in its standard deviation. In addition, histidine is shown as the representative consumed amino acid by hMSCs in static culture (Fig. 3C – D). Histidine data and kinetics model fit were acceptable. In static cultures, the most and least produced (moles/cell/h) amino acids were ornithine and glycine, respectively. The most and least consumed (moles/cell/h) amino acids were leucine and methionine, respectively.

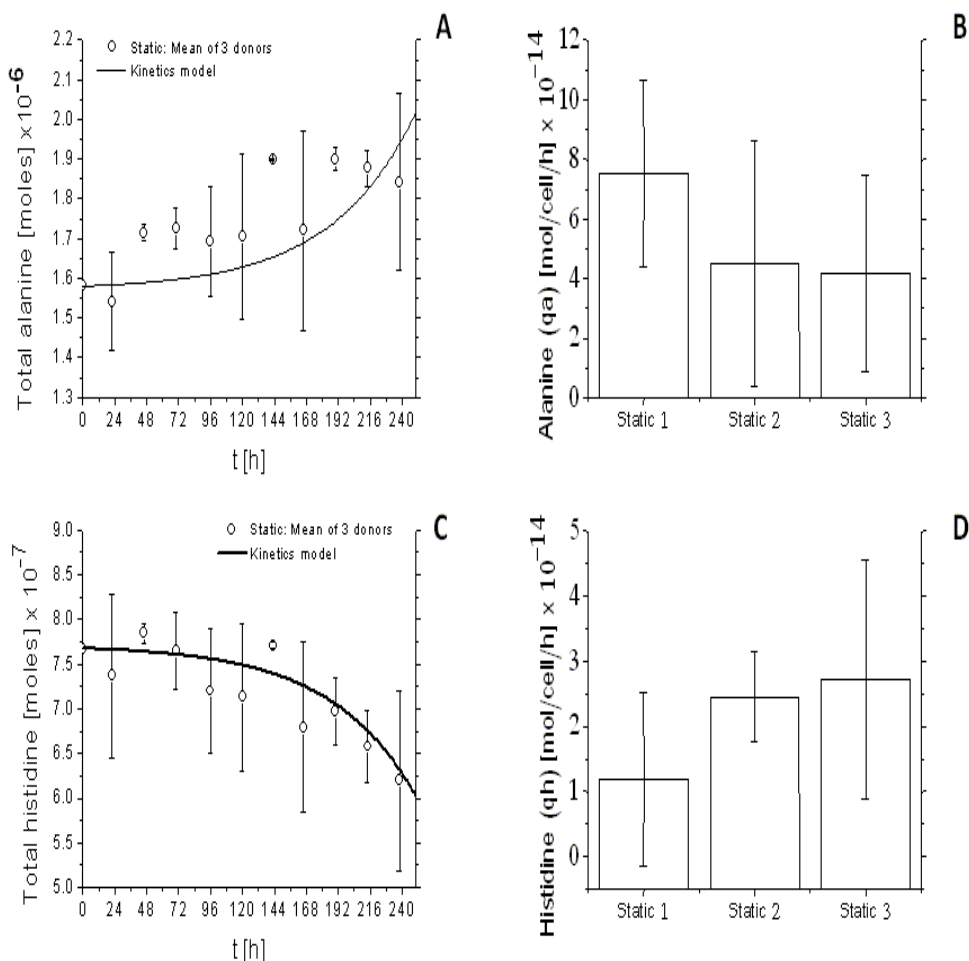


Figure 3 **A**: Alanine represents the produced amino acids in static cultures. Alanine data (○) and kinetics model (—) **B**: Bar plot of alanine production rates in static culture . **C**: Histidine represents the consumed amino acids in static cultures. Histidine data (○) and kinetic model fit (—). **D**: Bar plot of Histidine consumption rates.

In individual donors, it was observed that the large standard deviations in experimental data (Fig. 3) caused large standard deviations in consumption/production rates in static conditions (Table 4). Therefore, consumption and production trends in static conditions were deduced from the average production/consumption rates of three donors (Fig. 2F).

Growth and kinetics in Dynamic Culture

hMSCs proliferation studies involve now the use of bioreactors, where hMSCs proliferate under closely monitored and controlled environmental and operating conditions [6]. There were significant differences between static and dynamic culture

with respect to shear stress, cell-attachment material, seeding density and donor variation. Either one of these factors could have an effect on hMSCs proliferation [28, 33, 34]. Thus, it is not possible to determine the factor that causes differences from hMSCs proliferation in dynamic vs. static culture. With these differences in mind, we did however expect that some amino acids would be used similarly by proliferating hMSCs in static or dynamic conditions. Therefore, we explored this further by culturing hMSCs on micro-carriers (Fig. 4A) in a stirring vessel [27].

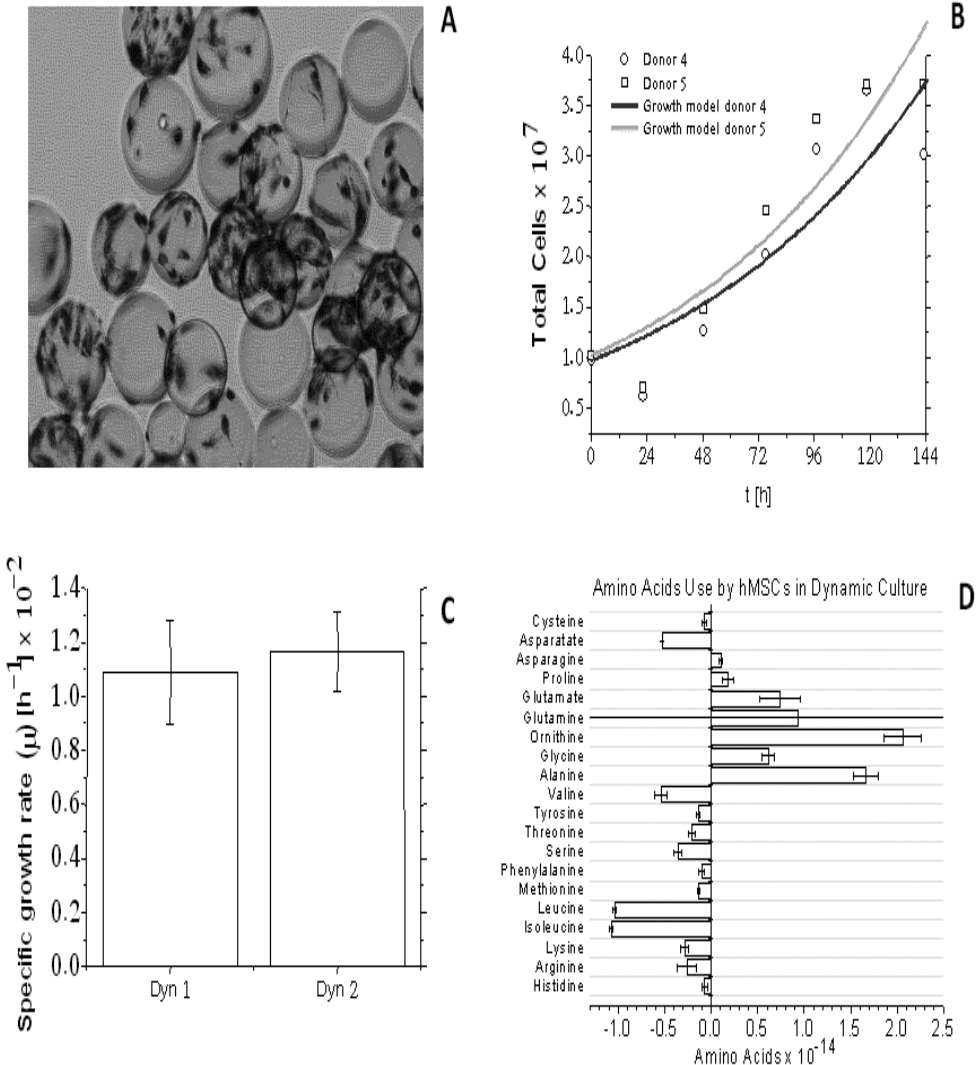


Figure 4 **A**: Cell load on the microcarriers after 6 days of culture. Stained with MTT, original magnification 40x. **B**: Cell numbers and growth model fit (–) in dynamic culture. **C**: Bar plot of specific growth rates of cells in dynamic culture. **D**: Amino acid use by hMSCs in dynamic culture. Mean and error bars for each amino acid are representative of 2 donors.

First, cell numbers were analysed with growth model equation 4 (Fig. 4B). The cell numbers and kinetics model fit was suboptimal. The fit for the complete culture period produced the estimated specific growth rate (μ) for each hMSCs donor in dynamic conditions (Fig. 4C, table 5). With the specific growth rates estimated for each donor, the kinetics model (Eqs. 4 and 5) was used to analyze metabolic data in dynamic conditions. Specific growth rates, glucose consumption and lactate production (Table 3) rates corresponded to the magnitude of values found in literature [27] for micro-carrier cultivation of hMSCs. As has also been previously found, specific growth rates were significantly lower in dynamic than in static culture of hMSCs [27].

The growth and kinetics model equations 4 and 5 were then used to estimate the production/consumption rates of amino acid data obtained from hMSCs in dynamic conditions. Figure 4D shows the mean consumption/production rates of 2 donors in dynamic culture as presented on table 5. This showed that alanine, asparagine, glycine, glutamate, ornithine, and proline were produced by hMSCs donors in dynamic conditions. Similarly, arginine, aspartate, cysteine, histidine, isoleucine, leucine, lysine, methionine, phenylalanine, serine, threonine, tyrosine, and valine were consumed by hMSCs donors in dynamic conditions. Surprisingly, only glutamine did not show a definite trend (Fig. 4D). It is also important to note that amino acid consumption and production rates were lower, though not significantly, in dynamic cultures (Fig 4D, table 5) than in static cultures.

Table 5 Amino Acid Metabolic Rates in Dynamic Cultures.

	Consumption					
	1	SD	2	SD	Mean (n=2)	SD
Histidine	-0.09	0.12	-0.05	0.20	-0.07	0.03
Arginine	-0.18	0.43	-0.33	0.39	-0.26	0.10
Lysine	-0.25	0.27	-0.32	0.21	-0.28	0.04
Isoleucine	-1.07	0.30	-1.09	0.25	-1.08	0.02
Leucine	-1.03	0.29	-1.06	0.24	-1.04	0.02
Methionine	-0.12	0.05	-0.15	0.05	-0.14	0.02
Phenylalanine	-0.08	0.14	-0.12	0.12	-0.10	0.03
Serine	-0.33	0.20	-0.39	0.10	-0.36	0.04
Threonine	-0.18	0.22	-0.24	0.18	-0.21	0.04
Tyrosine	-0.12	0.14	-0.15	0.13	-0.14	0.02
Valine	-0.49	0.23	-0.59	0.18	-0.54	0.07
	Production					
Alanine	1.76	0.45	1.57	0.44	1.66	0.13
Glycine	0.66	0.30	0.57	0.24	0.61	0.07
Ornithine	2.21	0.40	1.92	0.41	2.06	0.20
	Indefinite					
Glutamine	-2.63	2.09	4.50	1.74	0.93	5.04
Glutamate	0.90	0.64	0.58	1.86	0.74	0.22
Proline	0.23	0.19	0.14	0.18	0.18	0.06
Asparagine	0.09	0.20	0.12	0.16	0.10	0.02
Asparatate	-0.53	0.14	-0.52	0.12	-0.52	0.00
Cysteine	-0.09	0.07	-0.06	0.09	-0.07	0.03

Alanine is shown as the representative produced amino acid by hMSCs in dynamic culture (Fig. 5A - B). There was a strong production trend in all donors, despite a poor fit with alanine data as reflected on its standard deviations. In addition, histidine is shown as the representative consumed amino acid by hMSCs in dynamic culture (Fig. 5C - D). Histidine data and kinetics model fit were acceptable. In dynamic cultures, the most and least produced (moles/cell/h) amino acids were ornithine and glycine, respectively (Table 5). The most and least consumed amino acids were isoleucine and histidine, respectively (Table 5).

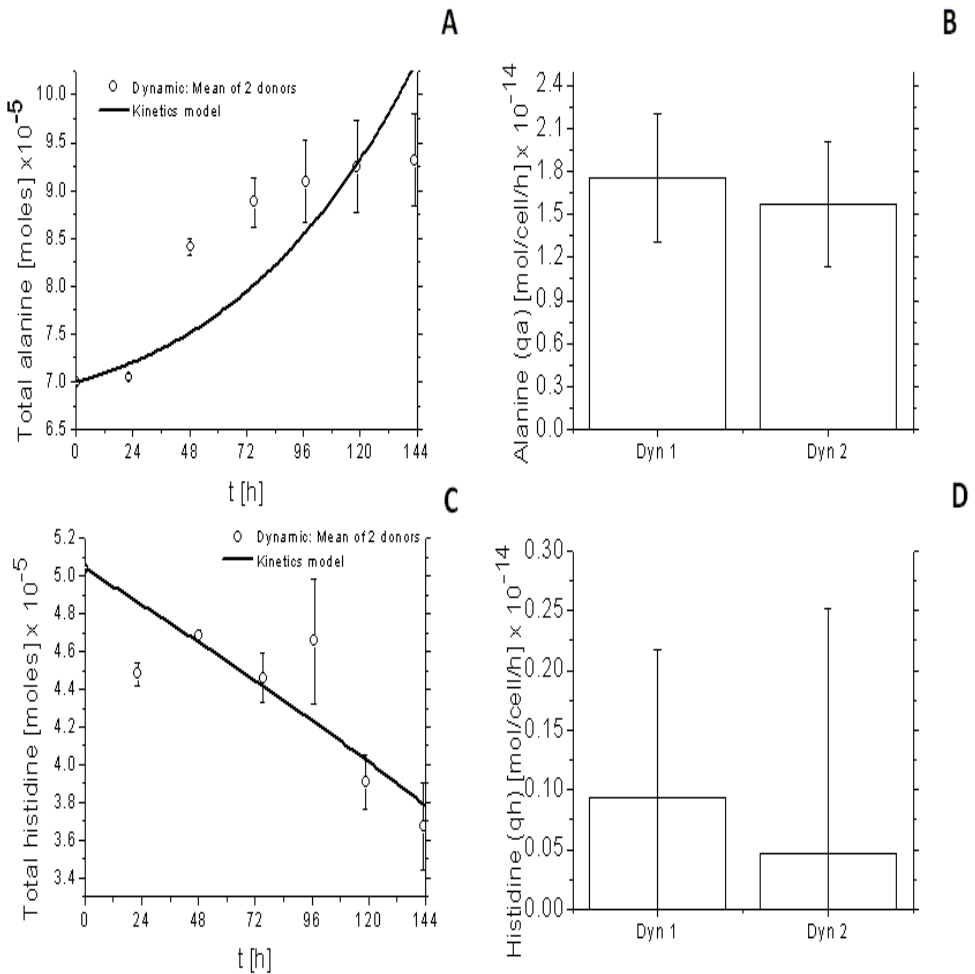


Figure 5 **A**: Produced amino acids by hMSCs in dynamic culture are represented by alanine. Alanine data and kinetic model fit (—). **B**: Bar plot of alanine consumption rates. **C**: Consumed amino acids by hMSCs in dynamic culture are represented by histidine. Histidine data and kinetic model fit (—). **D**: Bar plot of histidine consumption rates.

In individual donors, it was observed that the large standard deviations in experimental data (Fig. 5) caused large standard deviations in consumption/production rates in dynamic conditions (Table 5). Therefore, consumption and production trends in dynamic conditions were obtained from the average production/consumption rates of three donors (Fig. 5D).

Discussion

Despite the differences in static and dynamic culture (Shear stress, cell-attachment material, seeding density and donor variation), the number of amino acids that have similar kinetics show that there are fundamental patterns of amino acid metabolism by proliferating hMSCs. Arginine, histidine, lysine, isoleucine, leucine, methionine, phenylalanine, serine, threonine tyrosine, and valine were consumed by hMSCs in both static and dynamic cultures (Fig. 2F and 4D). In general, consumption of amino acids was higher in static culture, though not significantly, when compared to dynamic culture.

Specific growth rates were significantly higher for donors in static culture, which has been previously observed in other studies [27, 28]. A number of factors could account for these differences. For example, shear stress [33] can have a significant effect on proliferation through the formation of turbulent flow [35, 36]. In addition, micro-carrier and tissue culture plastic also present important surface differences [34] to account for different specific growth rates between static and dynamic cultures.

It was observed that the noise in cell numbers accounted in part for the large standard deviations in consumption/production rates in individual donors (Tables 4 and 5). Specially, for amino acids that showed a strong spontaneous degradation rate aspartate, asparagine, and glutamine in static and dynamic cultures (Table 1) In the consumed amino acids group, no amino acid was depleted during the static or dynamic culture period. The consumption of those amino acids is explained by their behaviour in other proliferative cells. Isoleucine, leucine, serine, and valine are amino acids that can be converted to derivates of the Krebs cycle, indirect to the generation of energy, and directly associated with protein biosynthesis [37]. In addition, arginine, and histidine, can be converted to glutamate for energy generation. Leucine [38], methionine [39], and threonine [40] have also been shown to be vital for cell and tissue development, where the amount of consumption could depend on the differentiation lineage that hMSCs follow. Consequently, consumption of these 11 amino acids by hMSCs could be essential, not only for hMSCs proliferation, but also in differentiation.

In the produced amino acids group, production by hMSCs was higher in static conditions (Fig. 2F and 4D), though only significantly for ornithine. Amino acids flux through metabolic pathways is a balance, which is highly dependent on concentrations [41]. For example production of alanine has been known to occur when there is excess of carbon sources in culture media [42]. In addition, glycine is a by-product of serine metabolism, therefore glycine could be the result of serine consumption

[37]. Lastly, ornithine is the in-between product from arginine to glutamate [43]. Therefore, production of amino acids is the result of high concentrations of carbon and energy sources, which in hMSCs culture renders ornithine alanine, and glycine consumption unnecessary.

While some amino acids kinetics were similar in static and dynamic culture, other amino acids, namely proline, cysteine, and glutamate showed opposite trends. Aspartate and cysteine were produced by hMSCs in static culture (Fig. 2F, table 4) and consumed by hMSCs in dynamic cultures (Fig. 4D, table 5). Also, asparagine, proline, and glutamate (Fig. 4D, Table 5) were produced by hMSCs in dynamic culture. Considering the attachment surface and shear stress differences in static and dynamic cultures, these amino acids could indicate the activation of mechanosensitive pathways [44]. In addition, the sensitivity and importance of amino acids in protein production could also indicate the components and reaction rates of trophic factor [45] production by hMSCs.

Conclusions

This study showed amino acid metabolic patterns by proliferating hMSCs on both tissue culture plastic and stirring vessel bioreactor cultures. The results showed that 11 amino acids were consumed and 3 were produced in both culture conditions. Also, these data showed that 6 amino acids had trends sensitive to culture conditions. Amino acid kinetics provide a pathway-driven context to explore and expand the knowledge of stem cell biology.

References

1. Aubin, J.E., *Bone stem cells*. Journal of Cellular Biochemistry, 1998: p. 73-82.
2. Sekiya, I., et al., *Expansion of Human Adult Stem Cells from Bone Marrow Stroma: Conditions that Maximize the Yields of Early Progenitors and Evaluate their Quality*. Stem Cells, 2002. **20**: p. 530 - 541.
3. Colter, D.C., et al., *Rapid Expansion of Recycling Stem Cells in Cultures of Plastic-adherent Cells from Human Bone Marrow* PNAS, 2000. **97**(7): p. 3113 -3218.
4. Colter, D.C., I. Sekiya, and D.J. Prockop, *Identification of a Subpopulation of Rapidly Self-renewing and Multipotential adult Stem Cells in Colonies of Human Marrow Stromal Cells* PNAS, 2001. **98**(14): p. 7841 - 7845.
5. Frauenschuh, S., et al., *A microcarrier-based cultivation system for expansion of primary mesenchymal stem cells*. Biotechnology Progress, 2007. **23**(1): p. 187-193.
6. Martin, I., D. Wendt, and M. Heberer, *The role of bioreactors in tissue engineering*. Trends in Biotechnology, 2004. **22**(2): p. 80-86.
7. Yang, Y., F.M.V. Rossi, and E.E. Putnins, *Ex vivo expansion of rat bone marrow mesenchymal stromal cells on microcarrier beads in spin culture*. Biomaterials, 2007. **28**(20): p. 3110-3120.
8. Schop, D., et al., *Expansion of Mesenchymal Stem Cells Using a Microcarrier Based Cultivation System: Growth and Metabolism*. Journal of Tissue Engineering and Regenerative Medicine, 2008. **2**(2 - 3): p. 126 - 35.
9. Prockop, D.J., *Marrow Stromal Cells For Nonhematopoietic Tissues*. Science, 1997. **276**: p. 71-74.
10. Owen, M. and A.J. Friedenstein, *Stromal Stem-Cells - Marrow-Derived Osteogenic Precursors*. Ciba Foundation Symposia, 1988. **136**: p. 42-60.
11. Caplan, A.I., *Mesenchymal stem cells and gene therapy*. Clinical Orthopaedics and Related Research, 2000(379): p. S67-S70.
12. Piersma, A.H., et al., *Characterization of Fibroblastic Stromal Cells from Murine Bone-Marrow*. Experimental Hematology, 1985. **13**(4): p. 237-243.
13. Jaiswal, N., et al., *Osteogenic differentiation of purified, culture-expanded human mesenchymal stem cells in vitro*. Journal of Cellular Biochemistry, 1997. **64**(2): p. 295-312.
14. Johnstone, B., et al., *In vitro chondrogenesis of bone marrow-derived mesenchymal progenitor cells*. Experimental Cell Research, 1998. **238**(1): p. 265-272.
15. Wakitani, S., T. Saito, and A.I. Caplan, *Myogenic Cells Derived from Rat Bone Marrow Mesenchymal Stem-Cells Exposed to 5-Azacytidine*. Muscle & Nerve, 1995. **18**(12): p. 1417-1426.
16. Pittenger, M.F., et al., *Multilineage potential of adult human mesenchymal stem cells*. Science, 1999. **284**(5411): p. 143-147.
17. Choi, K.M., et al., *Effect of essential and nonessential amino acid compositions on the in vitro behavior of human mesenchymal stem cells*. Korean Journal of Chemical Engineering, 2007. **24**(6): p. 1058-1063.
18. Caplan, A., *Why are MSCs therapeutic? New data: new insight*. Journal of Pathology, 2009. **217**(2): p. 318-324.
19. Doverskog, M., L. Ohman, and L. Haggstrom, *Regulation of proliferation and*

- metabolism in serum-free cultures of Spodoptera frugiperda (Sf9) cells.* Abstracts of Papers of the American Chemical Society, 1997. **213**: p. 153-BIOT.
20. Duval, D., et al., *Factors Controlling Cell-Proliferation and Antibody-Production in Mouse Hybridoma Cells .I. Influence of the Amino-Acid Supply.* Biotechnology and Bioengineering, 1991. **38**(6): p. 561-570.
 21. Sanfeliu, A., et al., *Analysis of nutritional factors and physical conditions affecting growth and monoclonal antibody production of the hybridoma KB-26.5 cell line.* Biotechnology Progress, 1996. **12**(2): p. 209-216.
 22. Simpson, N.H., et al., *In hybridoma cultures, deprivation of any single amino acid leads to apoptotic death, which is suppressed by the expression of the bcl-2 gene.* Biotechnology and Bioengineering, 1998. **59**(1): p. 90-98.
 23. Alberts, B., et al., *Molecular Biology of the Cell.* 5th ed. 2008, New York: Garland Science. 1268.
 24. Kontoravdi, C., et al., *Modeling Amino Acid Metabolism in Mammalian Cells Toward the Development of a Model Library.* Biotechnol. Prog., 2007. **23**(6): p. 1261 - 9.
 25. Larson, B.L., J. Ylostalo, and D.J. Prockop, *Human multipotent stromal cells undergo sharp transition from division to development in culture.* Stem Cells, 2008. **26**(1): p. 193-201.
 26. Gregory, C.A., et al., *How Wnt signaling affects bone repair by mesenchymal stem cells from the bone marrow.* Stem Cell Biology: Development and Plasticity, 2005. **1049**: p. 97-106.
 27. Schop, D., et al., *Expansion of human mesenchymal stromal cells on microcarriers: growth and metabolism.* J Tissue Eng Regen Med, 2010. **4**(2): p. 131-40.
 28. Higuera, G., et al., *Quantifying In Vitro Growth and Metabolism Kinetics of Human Mesenchymal Stem Cells Using a Mathematical Model.* Tissue Engineering Part A, 2009. **15**(9): p. 2653-2663.
 29. Both, S.K., et al., *A Rapid and Efficient Method for Expansion of Human Mesenchymal Stem Cells* Tissue Engineering, 2007. **13**(1): p. 3 - 9.
 30. Neeleman, R. and A.J.B.v. Boxtel, *Estimation of specific growth rate from cell density measurements.* Bioprocess and Biosystems Engineering, 2001. **24**(3): p. 179-185.
 31. Soons, Z.I.T.A., et al., *Observer design and tuning for biomass growth and Kla using online and offline measurements.* Journal of Process Control, 2008. **18**(7-8): p. 621-631.
 32. Schop, D., et al., *Growth, Metabolism and Growth Inhibitors of Mesenchymal Stem Cells.* Tissue Engineering: Part A, 2009. **15**.
 33. Zhao, F., R. Chella, and T. Ma, *Effects of shear stress on 3-D human mesenchymal stem cell construct development in a perfusion bioreactor system: Experiments and hydrodynamic modeling.* Biotechnol Bioeng, 2007. **96**(3): p. 584-95.
 34. Wei, J., et al., *Comparison of physical, chemical and cellular responses to nano- and micro-sized calcium silicate/poly(epsilon-caprolactone) bioactive composites.* J R Soc Interface, 2008. **5**(23): p. 617-30.
 35. 'tRiet, K.v. and J. Tramper, *Basic Bioreactor Design.* First ed. 1991, New York, Basel: Marcel Dekker, Inc. 465.
 36. Meinel, L., et al., *Bone tissue engineering using human mesenchymal stem cells:*

- effects of scaffold material and medium flow.* Ann Biomed Eng, 2004. **32**(1): p. 112-22.
37. Nelson, D. and M. Cox, *Lehninger Principles of Biochemistry*. Vol. 3. 2000, New York: Worth publishers.
38. Zhang, P.C., et al., *The GCN2 eIF2 alpha kinase is required for adaptation to amino acid deprivation in mice.* Molecular and Cellular Biology, 2002. **22**(19): p. 6681-6688.
39. Rees, W.D., *Manipulating the sulfur amino acid content of the early diet and its implications for long-term health.* Proceedings of the Nutrition Society, 2002. **61**(1): p. 71-77.
40. Wang, J., et al., *Dependence of Mouse Embryonic Stem Cells on Threonine Catabolism.* Science, 2009. **325**(5939): p. 435-439.
41. Bendall, S.C., et al., *Prevention of amino acid conversion in SILAC experiments with embryonic stem cells.* Molecular & Cellular Proteomics, 2008. **7**(9): p. 1587-1597.
42. Drews, M., et al., *Pathways of glutamine metabolism in Spodoptera frugiperda (Sf9) insect cells: evidence for the presence of the nitrogen assimilation system, and a metabolic switch by H-1/N-15 NMR.* Journal of Biotechnology, 2000. **78**(1): p. 23-37.
43. Tritsch, G.L. and G.E. Moore, *Spontaneous decomposition of glutamine in cell culture media.* Experimental Cell Research, 1962(28): p. 360-364.
44. Reilly, G.C. and A.J. Engler, *Intrinsic extracellular matrix properties regulate stem cell differentiation.* J Biomech, 2010. **43**(1): p. 55-62.
45. Caplan, A. and J. Dennis, *Mesenchymal stem cells as trophic mediators.* J Cell Biochem, 2006(98): p. 1076.



II

3D Kinetics of hMSCs

Chapter 3

Darcian permeability constant as indicator for shear stresses in regular scaffold systems for tissue engineering

Petra Vossenber^{1,2} Gustavo A. Higuera², Gerard van Straten¹, Clemens A. van Blitterswijk², and Anton van Boxtel¹

¹Systems and Control Group, Wageningen University, Wageningen, The Netherlands.

²Department of Tissue Regeneration, Institute for Biomedical Technology, University of Twente, Enschede, The Netherlands.

Abstract

The shear stresses in printed scaffold systems for tissue engineering depend on the flow properties and void volume in the scaffold. In this work, Computational Fluid Dynamics (CFD) is used to simulate flow fields within porous scaffolds used for cell growth. From these models the shear stresses acting on the scaffold fibres are calculated. The results led to the conclusion that the Darcian (k_1) permeability constant is a good predictor for the shear stresses in scaffold systems for tissue engineering. This permeability constant is easy to calculate from the distance between and thickness of the fibres used in a 3D printed scaffold. As a consequence computational effort and specialists for CFD can be circumvented by using this permeability constant to predict the shear stresses. If the permeability constant is below a critical value, cell growth within the specific scaffold design may cause a significant increase in shear stress. Such a design should therefore be avoided when the shear stress experienced by the cells should remain in the same order of magnitude.

Introduction

Tissue engineering applies the principles of biology and engineering to the development of functional substitutes for damaged tissue such as skin, cartilage or bone [5]. The core materials used in tissue engineering are different types of cells, for example fibroblasts, chondrocytes or mesenchymal stem cells (MSCs).

To establish a tissue culture, expansion and differentiation of cells is needed. This expansion and differentiation should preferably occur in a physiological environment which is closer to the cells' native environment. To achieve this, bioreactor systems

may be used. One way to culture cells *in vitro* is in a perfusion bioreactor housing a three-dimensional (3D) scaffold. Other options include two-dimensional (2D) polystyrene tissue culture flasks, spinner flasks, where the cells are usually grown on microcarriers, and hollow-fibre reactors, where the cells are attached to the outside of the fibres[10].

In a perfusion system, the cells may be attached to printed scaffolds (see Fig. 1 as an example), which can be fabricated using 3D printing technology consisting of fibres of the copolymers polyethylene oxide terephthalate (PEOT) and polybutylene terephthalate (PBT) with polyethylene glycol (PEG) starting blocks [7]. Many other types of scaffold are nowadays available with varying architectures, composite materials and surface chemistries. Scaffolds provide a large surface area that facilitates the attachment, survival, migration, proliferation and differentiation of cells [8]. Furthermore, the scaffold contains void spaces to allow mass transport to take place through convection and diffusion [4]. The advantage of printed scaffolds is that they have a formally designed regular structure, which is reproducible. This offers the potential for greater control and a better prediction of the fluid flow within the scaffold compared to random structures. [8] A possibility could therefore be to use the regular 3D printed scaffolds for the culture of undifferentiated MSCs, chondrocytes or endothelial cells and investigate the effect of fluid flow on the growth of the different cell types. If this concept is understood, a next step could be to cause specific cell differentiation of the MSCs as a result of a difference in fluid flow.

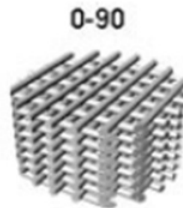


Figure 1 Scaffold architecture with perpendicular fibres [7].

The flow of medium through the scaffold is necessary to provide the cells with nutrients and oxygen and flush out the metabolic products. The success of cell attachment to the scaffold depends on the flow regime. High flows cause high shear stress [6] and prevent attachment of cells to the scaffold surface, already attached cells may be damaged or hindered in proliferation. Shear stress is also considered as an important parameter for *in vivo* systems. Wang and Tarbell (2000) found by experiments for smooth muscle cells that with increasing shear stress the production of prostaglandins increased. The results of Wang and Tarbell (2000) indicate that the blood flow rate plays a role in the signal communication system from the blood

vessels to the smooth muscle cells.

When designing a scaffold, the shear stress that acts on the fibres of the scaffold on which the cells grow must therefore be considered as a design parameter. Shear stress is proportional to the velocity gradient and is a function of design parameters such as fibre diameter and distance between the fibre centres and operational variables such as fluid velocity.

Martin *et al.* (2004) argue for the use computational techniques to predict the effect of flow conditions in bioreactors used for tissue engineering. Boschetti *et al.* (2006) apply Computational Fluid Dynamics (CFD) calculations to a 3D-scaffold structure. Their work shows that the porosity, i.e. the void volume in the scaffold, is an important variable that affects the shear stress in scaffold systems. A conclusion from their work could be that prediction of the shear stress can only be obtained from CFD calculations. However, if we realize that the pressure drop caused by fluid-wall interaction in a structure is proportional to permeability of the structure, then it is also an option to link the shear stress to permeability constants. Wang and Tarbell (2000) use the permeability constant from Darcy's law to derive the average shear stress from experiments on a collagen gel. The permeability constant was determined using the viscosity of the perfusing medium, the measured volumetric flow rate, the cross-sectional area and the imposed pressure drop over the length of the reactor.

In this work the shear stress in a regular printed scaffold is calculated with CFD. CFD calculations demonstrated, just as in the work of Boschetti *et al.* (2006) that the shear stress varies with the porosity of the scaffold. The Darcian permeability constant in the Forchheimer equation showed good results as predictor of shear stress and was independent of scaffold parameters like porosity. With these findings the shear stress in scaffolds can directly be predicted from the Darcian permeability constant without doing extensive CFD calculations.

Actual measurement of shear stress in the dimensions of scaffolds used for cell growth is not yet possible. The only experimental option is to investigate the cells' phenotype in response to shear stress. The focus of this work, however, is on finding a relationship between scaffold design and shear stress. To obtain a visual indication on how and where cells grow on a regular 3D printed scaffold, goat mesenchymal stem cells (gMSCs) were cultivated in a dynamic perfusion system.

Methods

CFD-calculations

In the fluid domain, the Navier-Stokes equation for incompressible fluid dynamics was solved. The equation is as follows:

$$\rho \frac{\partial u}{\partial t} - \eta \nabla^2 u + \rho(u \cdot \nabla)u + \nabla p = F \quad (1)$$

where ρ is the fluid density (kg m^{-3}), u is the velocity field (m s^{-1}), t is the time (s), η is the dynamic viscosity of the fluid ($\text{kg m}^{-1} \text{s}^{-1}$), ∇ is the del operator, p is the pressure (Pa) and F represents other forces (gravity or centrifugal force) (in this case $F=0$).

The steady state equation was applied because the cell cultivation in a perfusion system is mainly in steady state. Furthermore, when the system is disturbed, it will restore itself quickly.

Assuming the fibres of the scaffold and the wall of the bioreactor to be rigid and impermeable, no-slip boundary conditions were applied to the surfaces of the fibres and the wall of the bioreactor. The culture medium flows in the positive z-direction. At $z=0$, the boundary condition was set to a specific inlet velocity with only a z-component. The boundary condition at the outlet was set to normal flow/pressure with null pressure.

For laminar flow, the wall shear stress is defined by the normal velocity gradient at the wall as:

$$\tau_w = \eta \frac{\partial v}{\partial n} \quad (2)$$

where τ_w is the wall shear stress (Pa), η is the dynamic viscosity of the fluid ($\text{kg m}^{-1} \text{s}^{-1}$), v is the fluid velocity (m s^{-1}) and n is the x-, y- and z-direction (m).

CFD models of the fluid flow through different scaffold designs were set-up and solved in the modelling package COMSOL Multiphysics 3.3. The computations were carried out on a PC with 10 Gb of RAM. The solver GMRES, which is an iterative solver, was used to simulate the fluid flow through the different scaffold designs. A predefined mesh size, called 'fine', was used to divide the fluid domain into elements. The maximum element size scaling factor for this predefined mesh was 0.8, the element growth rate 1.45, the mesh curvature factor 0.5, the mesh curvature cut-off 0.02 and the resolution of narrow regions 0.6.

In 3D the total wall shear stress is calculated based on the shear stress acting in the x-, y- and z-direction using Pythagoras' theorem. CFD calculations with COMSOL allow the export of shear stress values in the x-, y- and z-direction at points along the edges which make up the scaffold model. Data from COMSOL was exported to calculate the average and maximum shear stress found for specific scaffold designs. The average shear stress is an indication of the amount of shear stress that most cells will likely experience within the scaffold system. The maximum shear stress is an indication of the extremities of the scaffold system with respect to the shear stress. Some cells may experience these extremities within the scaffold system.

Porosity and Permeability Constants

One way to characterise a scaffold design is in terms of porosity (ϵ) [1], whereby the porosity is defined as the percentage of void volume within the total volume of the scaffold. For a scaffold section, for which the width of the section equals the length and two fibres are present per layer, the porosity is given by:

$$\epsilon = \left(1 - \frac{2\pi r^2 n_l}{wh} \right) 100 \tag{3}$$

where r is the fibre radius (m), w is the width of scaffold section (m), n_l is the number of fibre layers and h is the height of scaffold section (m).

Permeability is a measure of the ability of a porous medium to transmit fluids through its interconnected pores or channels. Two permeability parameters, known as the Darcian, k_1 , and the non-Darcian, k_2 , permeability constants, can be found in the Forchheimer equation [2]. The Darcian permeability constant is related to the pure laminar flow properties while the non-Darcian permeability constant represents deviations from laminar flow. The Forchheimer equation states that for an incompressible fluid, the pressure drop through a rigid and homogeneous porous medium is given by:

$$\frac{\Delta P}{L} = \frac{\eta}{k_1} v + \frac{\rho}{k_2} v^2 \tag{4}$$

where ΔP is the pressure drop (Pa), L is the path length (m), η is the dynamic viscosity of the fluid ($\text{kg m}^{-1} \text{s}^{-1}$), k_1 is the Darcian permeability constant (m^2), v is the fluid velocity (m s^{-1}) and k_2 is the non-Darcian permeability constant (m).

Ergun proposed empirical expressions to describe the two permeability parameters for packed columns made of grains [2] [9]. These expressions are:

$$k_1 = \frac{\varepsilon^3 d^2}{150(1-\varepsilon)^2} \quad (5)$$

$$k_2 = \frac{\varepsilon^3 d}{1.75(1-\varepsilon)} \quad (6)$$

where ε is the porosity (as defined by equation 3) and d is the mean particle diameter of the medium in the packed column (m).

In scaffolds the flow is around fibres instead of around grains that make up a packed bed. This means that to evaluate k_1 and k_2 the mean particle diameter of the grains (d) has to be replaced by a structural property of the scaffold. Here d is defined as the diameter of the scaffold fibres as representation of the effective scale of the microstructure.

If the fluid velocity through the scaffold is taken to be $100 \mu\text{m s}^{-1}$ and the fibre radius $75 \mu\text{m}$, a Reynolds number equal to 7.5×10^{-3} results. Turbulent flow occurs for a Reynolds number larger than 1. This leads to the conclusion that while k_1 will be relevant in the transmittance of fluid through a scaffold and with a velocity of these dimensions, k_2 will not be.

Cell cultivation

Janssen *et al.* developed a perfusion bioreactor system capable of producing clinically relevant volumes of tissue-engineered bone on macro porous biphasic calcium phosphate scaffolds [3]. This system was used for the cultivation of gMSCs on regular 3D printed scaffolds, consisting of fibres of the copolymers PEOT and PBT with PEG starting blocks and fabricated as described by Moroni *et al.* (2006). The k_1 value in the system was $2,28 \times 10^{-10} \text{ m}^2$. 10 million gMSCs were used to dynamically seed a scaffold for 4 hours with a superficial velocity of $100 \mu\text{m s}^{-1}$. During cultivation medium was pumped through the scaffold with the same superficial velocity as was used during seeding. The medium (300 ml) was refreshed every 3 days.

After 14 days of cultivation the scaffold was removed from the system and fixed in 1,5% glutaraldehyde, 0,14 M cacodylic buffer, pH 7,2-7,4 adjusted with 1 M hydrochloric acid (HCl). The fixed scaffold was placed in phosphate buffered saline (PBS) to cut into smaller sections. The sections were dehydrated and subsequently dried with a CO_2 critical point dryer, CPD 030 (Balzers). The sections were coated with gold using a sputter coater, 108Auto (Cressington) before examining them using a scanning electron microscope (SEM), XL 30 SEM FEG (Philips) at 10 kV.

Results and Discussion

CFD-calculations

In Figure 2A the shear stress acting on the side edge of a fibre present in two layers at different heights in a scaffold is given. The scaffold consists of five crossing fibres. Figure 2B is a schematic drawing of the fibre and cross-fibres for which the shear stress values are displayed in Figure 2A. The maxima of the curves in Figure 2A are the shear stress values found within the pores of the scaffold. The minima are the shear stress values found where two fibres cross perpendicularly. The values left in the graph concern the shear stress at positions along the fibre close to the wall and the other values the shear stress at positions towards the centre of the scaffold. The results indicate that the “wall” effect concerns only a small part of the fibre. Along the rest of the fibre, a repetitious shear stress pattern can be observed. This conclusion is also valid for scaffolds with other fibre diameters and distances between the fibres.

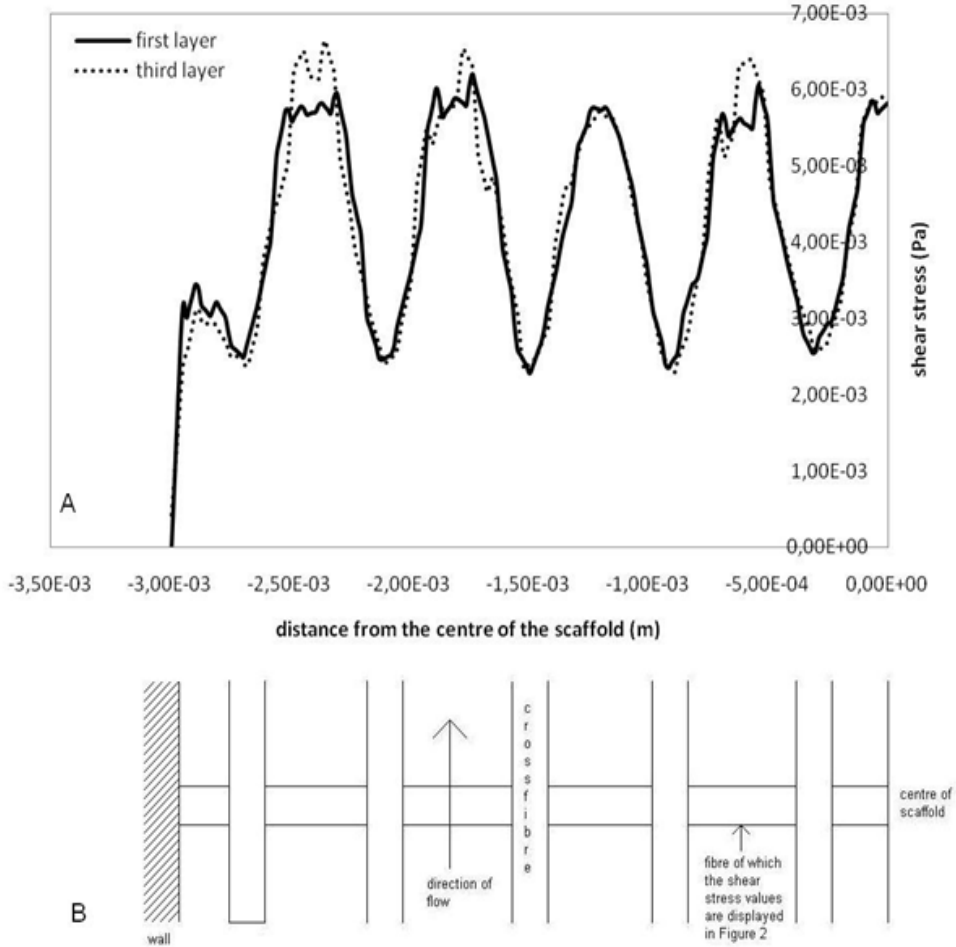


Figure 2 Shear stress acting on the side edge of fibres present in two layers at different heights in a scaffold. **A:** Shear stress values at the fibres. **B:** Position of cross-fibres and wall in the system. The scaffold consists of five crossing fibres. Inlet velocity=100 $\mu\text{m s}^{-1}$. Radius of fibres=130 μm . Distance between the centres of the fibres=600 μm .

Scaffolds used for tissue engineering concern over twenty crossing fibres in each layer. For such systems the “wall” effect is negligible. Therefore the shear stress is well represented by a section of the scaffold as given in Fig. 3. In Figure 3 a small section of the scaffold is shown. The width and length of the section are equal to twice the distance between the centres of the fibres. The boundary conditions applied to the four sides are lip/symmetry.

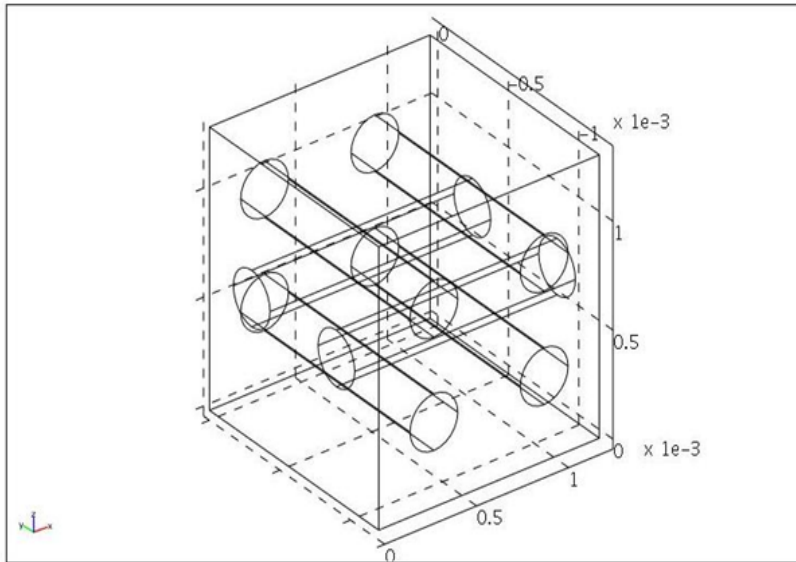


Figure 3 A small section of a scaffold containing three layers of fibres at 90° , length and width of section = 1,2 mm, height of section = 1,3 mm, radius of fibres = 130 μm , distance between centre of fibres = 600 μm .

Using this approach, it is possible to simulate the fluid dynamics within scaffolds that consist of thinner fibres, more layers of fibres and smaller distances between the fibre centres than the scaffold used for the calculations of which the outcomes are displayed in Figure 2A. The velocity profile within a scaffold section consisting of 32 layers of fibres, with a fibre radius of 75 μm and a distance between the fibre centres of 300 μm can be seen in Figure 4A. Figures 4B and 4C are close-ups for the velocity profile in between to crossing fibres and at a crossing fibre.

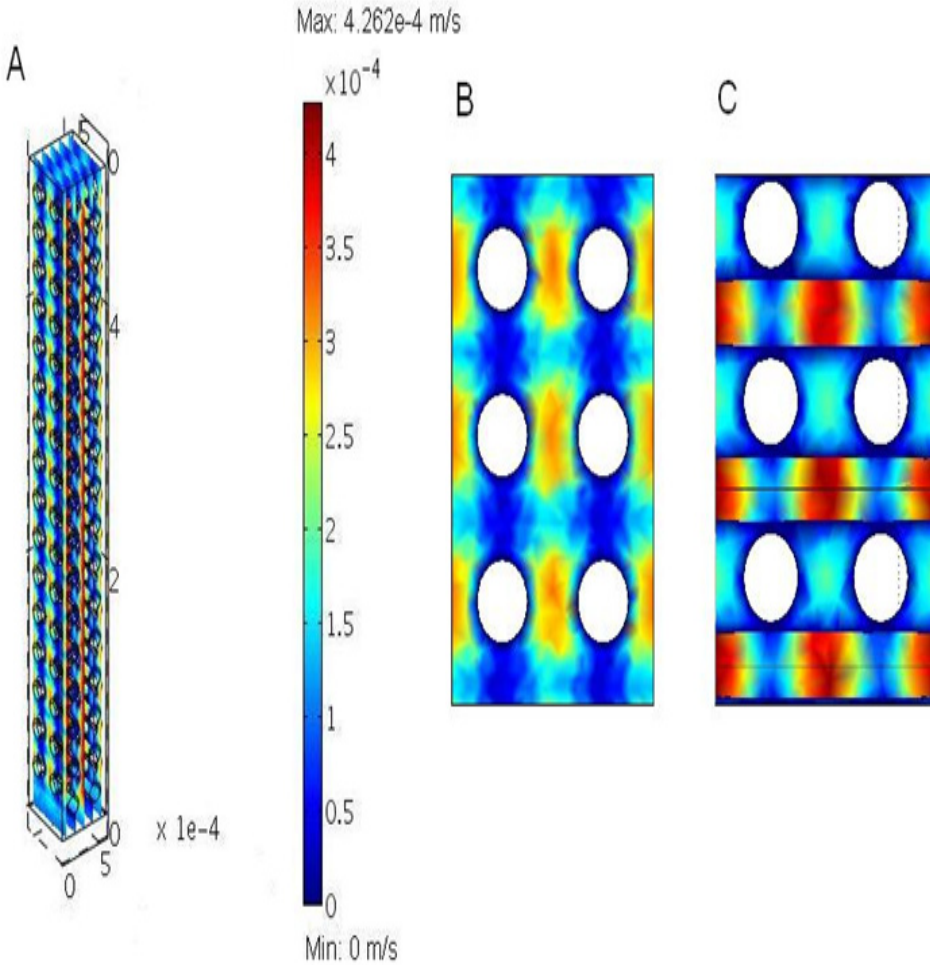


Figure 4 Velocity profile of the fluid within a porous scaffold consisting of 32 layers of fibres, radius of fibres= $75 \mu\text{m}$, distance between fibre centres= $300 \mu\text{m}$. Inlet velocity= $100 \mu\text{m s}^{-1}$. **A:** velocity profile within complete scaffold. **B:** Close-up of the flow profile in the middle between the crossing fibres. **C:** Close-up of the profile at a crossing fibre.

Porosity and Permeability Constants

As seen in Figure 5 the average and maximum total shear stress increases with decreasing porosity. These results are in line with the findings of Boschetti *et al.* (2006) and were expected as with decreasing porosity there is less space for the fluid to flow causing steeper velocity gradients. Hence higher shear stresses will act on the surfaces of the scaffold fibres.

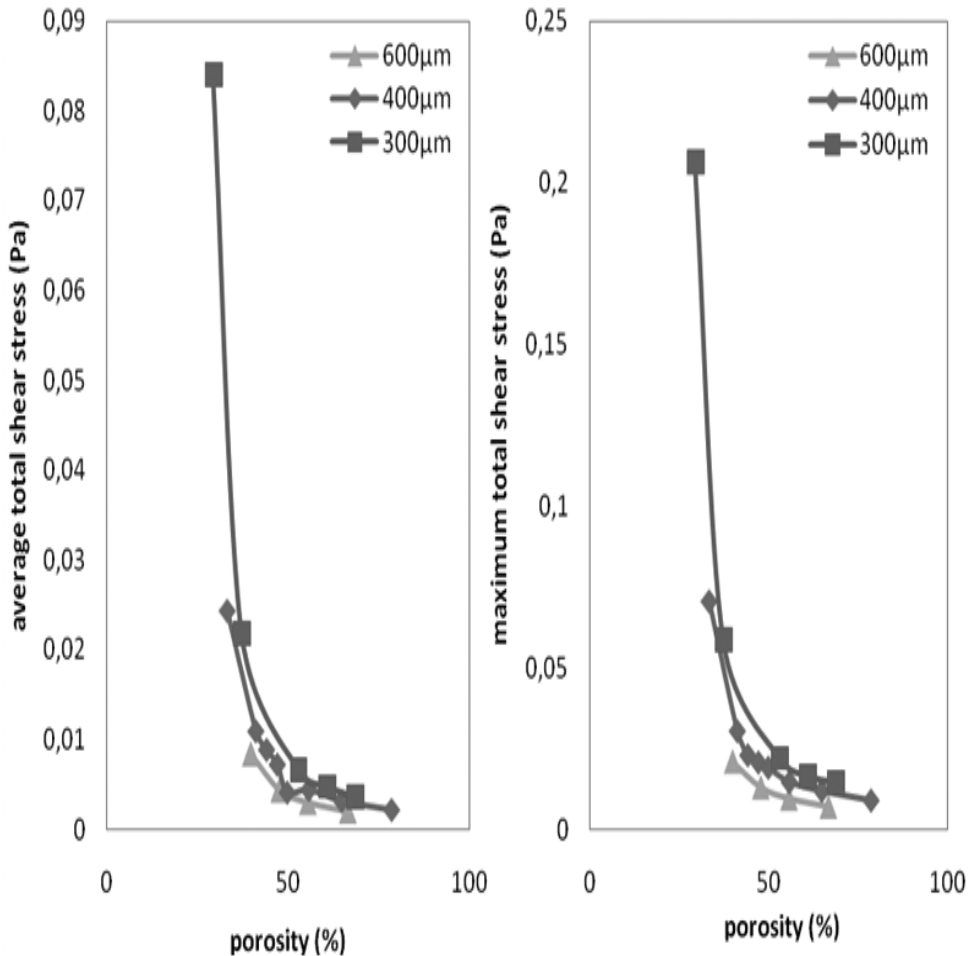


Figure 5 Average and maximum total shear stress as a function of relative porosity at varying distances between the centres of the fibres. Inlet velocity=100 $\mu\text{m s}^{-1}$.

In the studied range, the maximum total shear stress is between 2.5 and 4.1 times larger than the average total shear stress. The difference between the maximum and average total shear stress increases with decreasing porosity. Below 50% porosity and certainly below 40% porosity, the total shear stress starts to rise significantly.

The relationship between the average and maximum total shear stress and porosity depends on the distance between the centres of the fibres. This means that porosity alone is not a sufficient indicator for characterising the shear stress within the scaffold. Another scaffold characteristic is therefore necessary. Ideally, this scaffold characteristic should allow the estimation of the average and maximum shear stresses found within the scaffold design without having to carry out CFD calculations.

When the average and maximum shear stresses are plotted against the Darcian (k_f) permeability constant, the dependence of the average and maximum shear stress on the distance between the centres of the fibres becomes minimal (Fig. 6). k_f can thus be used as a scaffold characteristic to estimate the average and maximum shear stress acting on the fibres of a scaffold without having to carry out CFD calculations. The permeability constant allows the quick assessment of the effect of scaffold design on the shear stresses acting on the fibres of the scaffold. The Figure shows that the maximum and average shear stresses are nearly constant for high values of k_f . For low values the scaffold design is very shear sensitive, which can be useful when designing scaffolds for experiments where shear stress wants to be actively induced.

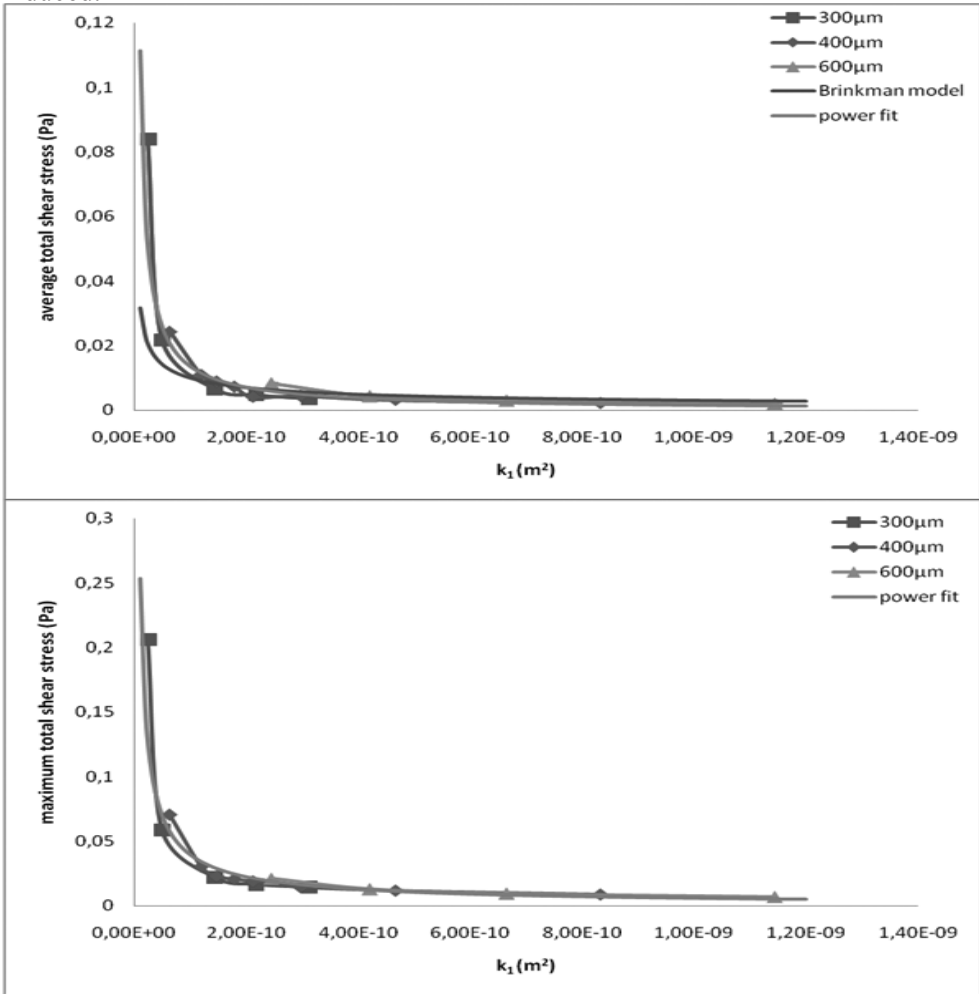


Figure 6 Average and maximum total shear stress as a function of the Darcian permeability constant, k_f , at varying distances between the centres of the fibres. Inlet velocity=100 $\mu m s^{-1}$. The average total shear stress graph includes a fit based on the Brinkman model at zero

cell concentration. Both the average and maximum total shear stress graphs include a power function fit of the computed data.

Below a Darcian (k_1) permeability constant of about $1 \times 10^{-10} \text{ m}^2$, small changes in porosity or changes in the shortest distance between the fibres have a large effect on the average total shear stress. These values for the k_1 can thus be seen as critical values for an inlet velocity of $100 \mu\text{m s}^{-1}$.

Wang and Tarbell (1995) use the Brinkman model to calculate the average wall shear stress on smooth muscle cells located in an artery wall. The muscle cells are modelled as a periodic array of cylindrical objects. They express the average shear stress as a function of the cell concentration (C), the Darcian permeability constant (k_1), the fluid velocity (v) and the dynamic viscosity of the fluid (η):

$$\tau_w = \frac{B\eta v}{\sqrt{k_1}} \tag{7}$$

where the constant B is a function of the cell volume (C) in a volume element:

$$B = \frac{4}{\pi} \frac{1 - 0.319285C^2 - 0.043690C^4}{\sqrt{(1 - C - 0.305828C^4)(1 + C - 0.305828C^4)}} \tag{8}$$

At a cell concentration of zero, B becomes equal to $4/\pi$. A plot of the Brinkman model at zero cell concentration can be seen in Figure 6. We can see that at high values of k_1 the Brinkman model predicts the computed average shear stress data. At low values of k_1 the Brinkman model at zero cell concentration starts to deviate.

In our work instead of the cell concentration, the porosity of the scaffold (ϵ) is used. ϵ is a function of the fibre diameter and the distance between the centres of the fibres. With $\epsilon=1-C$, the Darcian permeability constant defined in equation 5 becomes:

$$k_1 = \frac{(1 - C)^3 d^2}{150C^2} \tag{9}$$

The expression shows that two different scaffold structures with the same value for C or ϵ can have different values for k_1 . Therefore plotting the average shear stress against the Darcian permeability constant will yield different lines for the shear stress depending on the fibre diameter and the distance between the centres of the fibres. However, in Figure 6 we see only small variations between the lines. The reason for this result might be complexity of the scaffold structure with crossing

fibres compared to the system considered by Wang and Tarbell (1995) with parallel fibres. In addition, Swartz and Fleury (2007) suggest that differences arise between the solution from the Navier-Stokes equation, as used in our work, and the Brinkman model, as used by Wang and Tarbell (1995), because the Navier-Stokes equation takes into account the exact location and dimensions of the fibres.

The average (τ_{wavg}) and maximum (τ_{wmax}) shear stress data in Figure 6 were fitted with the following power functions:

$$\tau_{wavg} = 9.82 \times 10^{-12} k_f^{-9.14 \times 10^{-1}} \tag{10}$$

$$\tau_{wmax} = 3.36 \times 10^{-10} k_f^{-8.07 \times 10^{-1}} \tag{11}$$

Equations 10 and 11 could be used by scaffold designers to quickly have an indication of what average and maximum shear stress values one can expect in a specific scaffold design.

The local shear stress is also linked to the permeability constant k_f . Figure 7 shows the local shear stress acting on the side edge of a fibre, which is crossed by two other fibres at 2×10^{-4} and 6×10^{-4} m, for varying k_f values. As was seen in Figure 6 the shear stress decreases for increasing k_f values. The large difference in shear stresses for a k_f value of 1.20×10^{-10} and 6.35×10^{-11} m² could also be observed in Figure 6. As was mentioned above, k_f values below 1×10^{-10} m² are critical values as small changes in the scaffold dimensions (i.e. a small increase in the diameter of the fibre due to cell growth) will have a large effect on the shear stress.

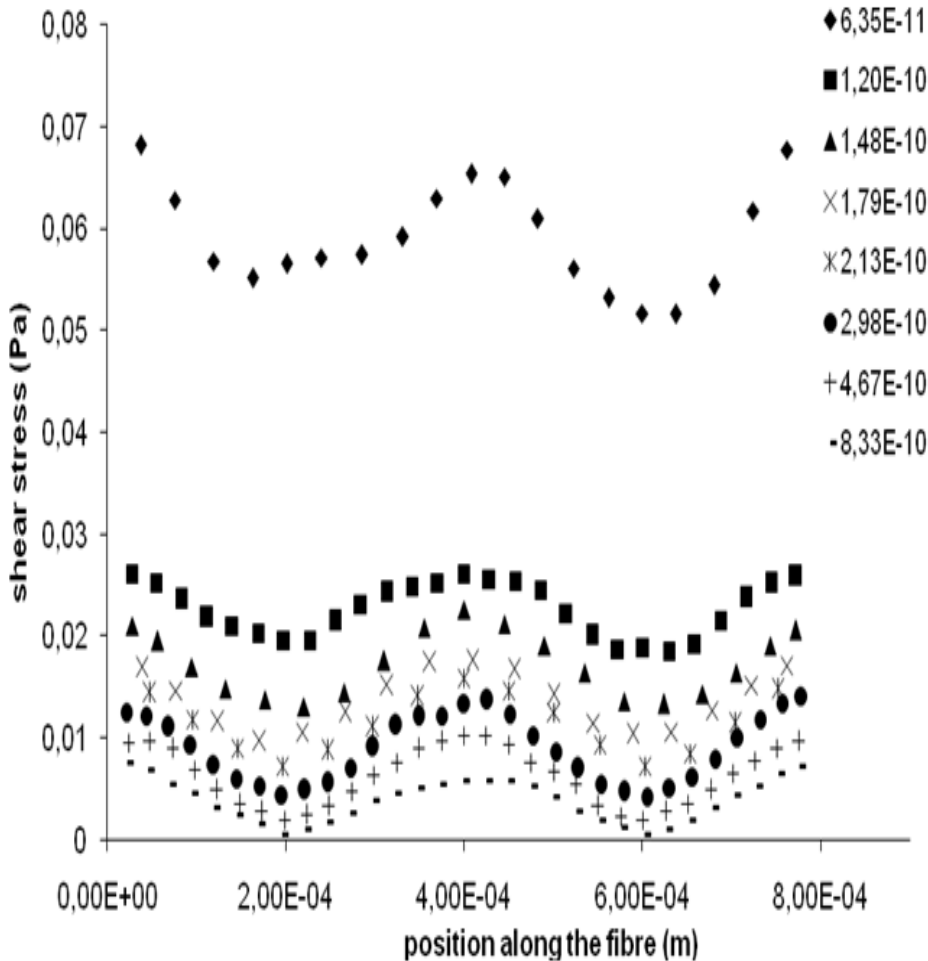


Figure 7 Shear stress acting on the side edge of a fibre, which is crossed by two other fibres at 2×10^{-4} and 6×10^{-4} m, for varying k_f values. Distance between the centres of the fibres = $400 \mu\text{m}$. Inlet velocity = $100 \mu\text{m s}^{-1}$.

The shear stress is related to the linear flow velocity within the scaffold. The graph of average total shear stress as a function of the Darcian (k_f) permeability constant therefore depends on the inlet velocity. In Figure 8 the effect of varying linear inlet velocity on the average and maximum total shear stress is shown. The graphs display the average and maximum total shear stress set out against k_f for two different linear inlet velocities.

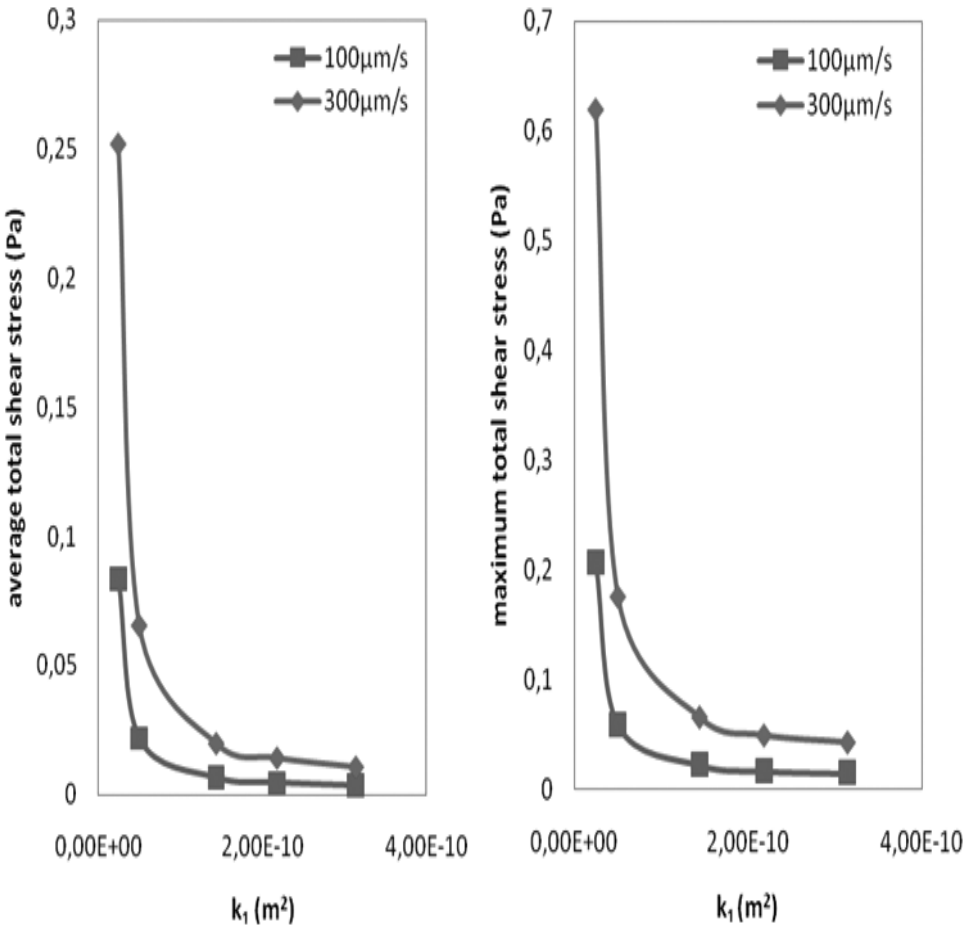


Figure 8 Effect of a difference in linear inlet velocity on the average and maximum total shear stress. The average total shear stress is displayed as a function the Darcian permeability constant, k_1 , at a distance of 300 μm between the centres of the fibres. Inlet velocities= 100 and 300 $\mu\text{m s}^{-1}$.

As the inlet velocity is changed from 100 $\mu\text{m s}^{-1}$ to 300 $\mu\text{m s}^{-1}$ the average and maximum total shear stresses are also tripled. This result which correspond with the work of Wang and Tarbel (1995) indicates that the flow is in the laminar region (as was expected based on the low Reynolds number), where the wall shear stress is directly proportional to the normal velocity gradient at the wall. This leads to the conclusion that as long as the flow is laminar the average and maximum total shear stress can be calculated for different inlet velocities from the shear stress found for an inlet velocity of 100 $\mu\text{m s}^{-1}$.

Cell cultivation

Figure 9 shows a SEM photograph of gMSCs and extracellular matrix (ECM) attached to a printed scaffold. It can be seen that cell growth and ECM deposition results in a slight increased fibre diameter and decreased porosity. The Darcian permeability constant will therefore decrease. When a scaffold design is made whereby the permeability constant is around or below the critical value, cell growth within the scaffold may cause a significant increase in shear stress. Such a design should therefore be avoided when the shear stress experienced by the cells should remain in the same order of magnitude.

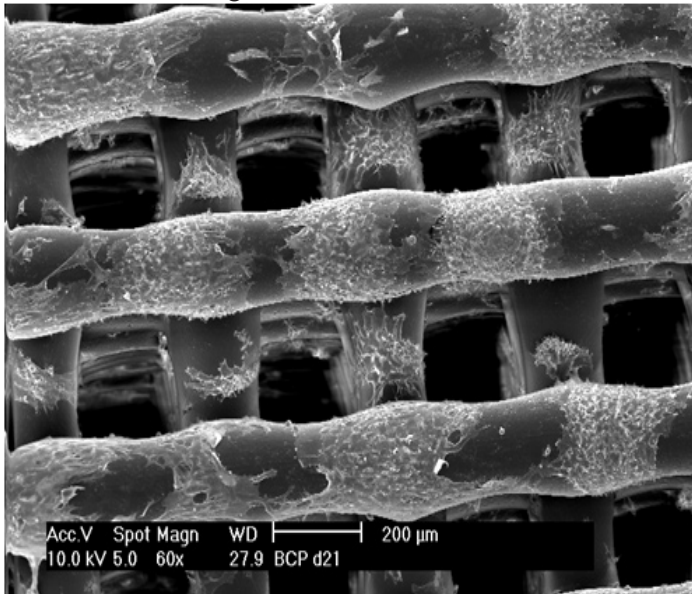


Figure 9 Scanning electron microscope (SEM) photograph of goat mesenchymal stem cells (gMSCs) and extracellular matrix (ECM) attached to printed scaffolds, consisting of fibres of the copolymers polyethylene oxide terephthalate (PEOT) and polybutylene terephthalate (PBT) with polyethylene glycol (PEG) starting blocks. The k_f value in this system was $2,28 \times 10^{-10} \text{ m}^2$, photograph was taken after 14 days of cultivation with a superficial medium flow velocity of $100 \text{ } \mu\text{m s}^{-1}$.

Figure 9 also gives a visual indication that cells grow the best around the crossings of the fibres where the shear stress is the lowest. Cell growth may occasionally take place from one fibre to the next. The shear stress experienced by these cells were not incorporated in the CFD calculations as the largest amount of cells cover the fibres and lead to an increase in fibre diameter. In addition, non-smooth cell coverage of the scaffold may increase the friction factor between the fluid and the scaffold. The effect of non-smooth deposition is difficult to predict as there are so many possible options for coverage.

Conclusions

Shear stress is an important variable for *in vivo* systems and *in vitro* cultivation of cells in bioreactors. Too high shear stress prevents attachment of the cells to the scaffold structures, may damage cells and hinder proliferation. Modern computational techniques as Computational Fluid Dynamics (CFD) allow the calculation of the shear stress in different scaffolds. However, the CFD calculation request for a high computational capacity and specialists to translate the scaffold structure into a CFD computer program.

By performing CFD calculations on printed scaffolds, this work demonstrates that CFD calculations can be circumvented in the future by using the Darcian (k_f) permeability constant as indicator for shear stresses. Calculation of this constant from equations 3, 5, 10 and 11 allows a quick assessment of the effect of scaffold design on the average and maximum shear stress acting on the fibres of a printed scaffold. If the permeability constant is below a critical value, the shear stress will be too high for effective cultivation. Moreover, with cell growth at the fibres of the scaffold the permeability of the scaffold can decrease and may result in a significant increase in shear stress if the permeability constant is around the critical value. Such a design should therefore be avoided when the shear stress experienced by the cells should remain in the same order of magnitude.

We expect that the Darcian permeability constant can play a similar role in estimating the shear stress in other scaffold structures and also for characterizing irregular systems. However, these applications must be validated.

References

1. Boschetti, F., Raimondi, M. T., Migliavacca, F. and Dubini, G. (2006). "Prediction of the micro-fluid dynamic environment imposed to three-dimensional engineered cell systems in bioreactors." *Journal of Biomechanics* 39: 418-425.
2. Innocentini, M. D. M., Salvini, V. R., Macedo, A. and Pandolfelli, V. C. (1999). "Prediction of Ceramic Foams Permeability Using Ergun's Equation." *Materials Research* 2: 283-289.
3. Janssen, F. W., Oostra, J., Oorschot, A. v. and Blitterswijk, C. A. v. (2006). "A perfusion bioreactor system capable of producing clinically relevant volumes of tissue-engineered bone: In vivo bone formation showing proof of concept." *Biomaterials* 27: 315-323.
4. Karande, T. S., Ong, J. L. and Mauli-Agrawal, C. (2004). "Diffusion in Musculoskeletal Tissue Engineering Scaffolds: Design Issues Related to Porosity, Permeability, Architecture, and Nutrient Mixing." *Annals of Biomedical Engineering* 32(12): 1728-1743.
5. Langer, R. and Vacanti, J. P. (1993). "Tissue engineering." *Science* 260(5110): 920-926.
6. Martin, Y. and Vermette, P. (2005). "Bioreactors for tissue mass culture: Design, characterization, and recent advances." *Biomaterials* 26: 7481-7503.
7. Moroni, L., Poort, G., Keulen, F. v., Wijn, J. R. d. and Blitterswijk, C. A. v. (2006). "Dynamic mechanical properties of 3D fiber-deposited PEOT/PBT scaffolds: An experimental and numerical analysis." *Journal of Biomedical Materials Research Part A* 78A(3): 605-614.
8. Muschler, G. F., Nakamoto, C. and Griffith, L. G. (2004). "Engineering Principles of Clinical Cell-Based Tissue Engineering." *The Journal of Bone and Joint Surgery* 86(7): 1541-1558.
9. Nield, D. A. and Bejan, A. (2006). *Convection in Porous Media*, Springer New York.
10. Pörtner, R., Nagel-Heyer, S., Goepfert, C., Adamietz, P. and Meenen, N. M. (2005). "Bioreactor Design for Tissue Engineering." *Journal of Bioscience and Bioengineering* 100(3): 235-245.
11. Swartz, M. A. and Fleury, M. E. (2007). "Interstitial Flow and Its Effects in Soft Tissues." *Annual Review of Biomedical Engineering* 9: 229-256.
12. Wang, D. M. and Tarbell, J. M. (1995). "Modeling Interstitial Flow in an Artery Wall Allows Estimation of Wall Shear Stress on Smooth Muscle Cells." *Journal of Biomechanical Engineering* 117: 358-363.
13. Wang, S. and Tarbell, J. M. (2000). "Effect of Fluid Flow on Smooth Muscle Cells in a 3-Dimensional Collagen Gel Model." *Arteriosclerosis, Thrombosis, and Vascular Biology* 20: 2220-2225.

Chapter 4

Concentration Gradients Correlate With Three-dimensional Proliferation and Migration Patterns of Human Mesenchymal Stem cells

Gustavo Higuera¹, Nils Aufferman¹, Roman Truckenmueller¹, TWGM Spitters¹, Hugo Fernandes¹, Maryana Escalante², Reinout Stoop³, Jan de Boer¹, Vinod Subramaniam², Marcel Karperien¹, Lorenzo Moroni¹, Anton van Boxtel⁴, and Clemens A. van Blitterswijk¹.

¹Department of Tissue Regeneration, Institute for Biomedical Technology, University of Twente, Enschede, The Netherlands.

²Biophysical Engineering Group, Mesa+ Institute for Nanotechnology, University of Twente, Enschede, The Netherlands.

³TNO KvL BioSciences, Leiden, The Netherlands.

⁴Systems and Control Group, Wageningen University, Wageningen, The Netherlands.

Abstract

Concentration gradients are the most widespread physical phenomena found in developing and adult tissues. Therefore, cells are intrinsically adapted to gradients and use them to maintain or change their phenotypes. In this study, we investigated the effect of concentration gradients on tissue formation *in vitro* with human mesenchymal stem cells (hMSCs). Using mathematical modeling, 3D fiber deposition and bioreactor technology, we have demonstrated a strong correlation between concentration gradients and hMSCs proliferation and migration patterns. Chemotaxis guides hMSCs migration towards regions of high concentration of molecules. Kinetics, death, and cell cycle regulators showed that there was a remarkable adaptability by hMSCs to concentration gradients as defined by nutrient availability. Despite steep gradients in 3D scaffolds, hMSCs proliferated while avoiding significant death. Furthermore, cell migration into millimeter-size circular patterns in the scaffold's pores was supported by ECM organization that did not express collagen or sulphated glucosaminoglycans. Thus, form resulted from hMSCs proliferation. In addition, kinetic analysis showed that higher concentrations of nutrients control the rates of proliferation and do not induce differentiation markers. These data strongly suggests that nutrient availability has a morphogenetic effect that causes hMSCs proliferation and migration patterns. This can be relevant to up-scale tissue and organ regeneration strategies driven by stem cells.

Introduction

Gradients are common phenomena in nature. Concentration gradients are physical phenomena that occur when the distribution of molecules in space is not homogeneous as determined by diffusion and/or convection principles [1, 2]. In biological systems, concentration gradients occur over short (nanometers) and large distances (micrometers and millimeters), defining the cell and tissue milieu. Concentration gradients have been shown to regulate pattern formation during tissue development [3, 4] and induce concentration-dependant behaviour in adult tissues [5-10].

To study the role of gradients, concentration gradients are mimicked to recreate their spatial and temporal characteristics [6]. In this manner, nutrient gradients have been shown to control chondrocytes' kinetics in engineered cartilage [10]. In addition, oxygen roles in the regulation of tissues [7] have been elucidated for cardiac [5] and cartilage [8] tissues. Growth factor gradients have also recreated the complexity of osteochondral tissues [9]. In developing tissues, concentration gradients have other fundamental roles. Molecules produced by cells can induce migration of other cells further away by creating a concentration gradient [11]. Molecules that constitute these gradients are known as morphogens [12]. Cell migration can have a preferred direction in relation to a concentration gradient, which is known as chemotaxis [3]. Due to the various responses to concentration gradients reported for cells of adult and developing tissues, we set out to investigate the effect of concentration gradients on human mesenchymal stem cell (hMSCs) activity.

hMSCs have an inherent sensitivity to physical phenomena [13-16]. The responses of hMSCs to different oxygen tensions [17, 18] and to concentrations of trophic factors [19] have hinted at a controlled response of these cells to concentration gradients. To explore this in an experimental mass transport context, we used 2D surfaces, 3D fiber-deposited (3DF) scaffolds, and a perfusion bioreactor to vary the concentration-gradient profiles during culture of hMSCs. In addition, glucose was used to model concentration gradients and experimentally evaluate their effects on hMSCs proliferation and differentiation.

Here, we show that regions of higher nutrient concentrations can initiate the 3D spatial organization of hMSCs. These data suggest that concentration gradients can awaken the dormant developmental machinery of stem cells to generate 3D patterns of millimetre-size.

Materials and Methods

For disc and scaffold fabrication, poly(ethylene oxide terephthalate)-poly(butylene terephthalate) (PEOT/PBT, PolyVation, Groningen, The Netherlands) of the

300PEOT55PBT45 composition was used. According to its nomenclature aPEOT-bPBTc, (a) the molecular weight of starting poly(ethylene glycol) PEG blocks was 300 g/mol and (b and c) the weight percentage ratio PEOT/PBT was 55/45 [20].

Fabrication of the two-dimensional discs

2D substrates of 300PEOT55PBT45 were prepared by a hot-embossed compression molding technique. A stainless steel mold with circular features through holes of 2.2 cm in diameter was placed in between two silicon wafers that served as support and defined the molded surface for the hot embossing process. Granules of 300PEOT55PBT45 were placed inside the mold in sufficient quantity to fill up the mold cavities upon melting of the polymer. The process is depicted on Fig. 4B.

The silicon support was cleaned by immersion in piranha solution (3:1 concentrated H_2SO_4 / 33% aqueous H_2O_2) for 15 min, rinsed copiously with water and dried in a stream of N_2 . Subsequently, they were functionalized with 1H,1H,2H,2H-perfluorodecyltrichlorosilane (ABCRCR), deposited in gas phase that served as anti-adhesion layer to facilitate the polymer-support separation. For the hot embossing processing, a temperature controlled hydraulic press equipped with a water cooling system (Fontune Holland, the Netherlands) was used. The 300PEOT55PBT45 was placed in the aperture of the mold on top of the silicon support, the system was heated up to a temperature of 180 °C and then 10 bars were applied. After 5 minutes the system was cooled down to 60 °C and the pressure was released. The stack was removed from the press, the mold and the supports were manually separated, and later the polymer was released from the mold.

Fabrication of the three-dimensional scaffold

3D scaffolds were fabricated with a Bioplotter device (Envisiontec GmbH, Germany), which is an XYZ plotter previously described by Landers *et al.* (2000) [21]. In this study, the scaffold fabrication process is similar to that performed by Moroni *et al.* (2005) [20]. Briefly, cylindrical block models were CAD-designed with Rhinoceros software (Delft, The Netherlands) and loaded on the Bioplotter CAM software (PrimCAM, Einsiedeln, Switzerland). In addition, polymer granules were loaded in a stainless steel syringe and heated at 200° C in a thermal cartridge unit mounted on the mobile X-arm of the apparatus. A nitrogen pressure of 4 Bar was applied to the syringe when the polymer melted. Nitrogen was used in order to minimize the copolymer oxidation. The combination of software and physical set-up resulted in the extrusion of melted 300PEOT55PBT45 in the form of fibers deposited layer-by-layer onto a stage.

The fiber diameter was controlled with stainless steel Luer Lock hypodermic

needles (Unimed, Lausanne, Switzerland) with internal diameter (ID) of 250 μm . This needle diameter was chosen because experimentally it showed a good compromise in terms of feasible scaffold porosities and fabrication time as previous studies have shown [22]. The fiber spacing, layer thickness, and fiber deposition speed were inputs in the CAM software. Three cylindrical block models were printed: (A) 9.4 mm diameter \times 1 mm height and (B) 8 mm diameter \times 3 mm height. Design A was used in kinetics studies and to make pore architectures with a 45° angle of successive layers. Design B was used in bioreactor experiments. The fiber spacing was 0.65 mm and 1 mm for designs A and B, respectively. The layer thickness was 0.15 mm and the fiber deposition speed was 320 mm/min for all designs.

The deposition speed was increased in steps of 5% every 20 min to adjust for the change in polymer viscosity due to degradation. Scaffold architecture included deposition of fibers in each layer at 90° angles of the successive layers for kinetics and bioreactor experiments.

Scaffold characterization

Microcomputed tomography (μCT , eXplore Locus SP μCT scanner, GE, Brussels, Belgium) at 14 μm resolution were used to characterize 2D and 3D scaffolds. Volume, porosity, and surface area of 2D and 3D scaffolds were determined with Microview software (Open source) as performed before [23]. Briefly, the threshold was adjusted to differentiate on the grayscale image between polymer voxels and pore voxels (One voxel was a 23 \times 23 \times 23 μm volume-element). The fraction of pore voxels within a scaffold determined its porosity. The pore size was determined by filling pore voxels with overlapping spheres [24]. The average size of a sphere occupying the pore voxel determined the average pore size. The boundaries between pore and polymer voxels determine the specific surface area.

Isolation, culture and cryopreservation of hMSCs

We isolated, cultured, and cryopreserved human mesenchymal stem cells (hMSCs) as described by Both *et al*[25]. We obtained hMSCs from donors who were undergoing total hip replacement surgery and gave informed consent for bone marrow biopsy, approved by the local medical ethical committee. Mono-nucleated cells were counted in the aspirate and plated at a density of 500,000 cells/cm² in T-flasks (Nunc, Thermo Fischer Scientific, Roskilde, Denmark).

After addition of α -minimal essential medium (αMEM) proliferation medium, cells were cultured for four to five days. The αMEM proliferation medium contained minimal essential medium (GIBCO, Carlsbad, CA); 10 % fetal bovine serum of a selected batch (FBS; Biowhittaker, lot:8SB0002; Loza, Verviers, Belgium); 0.2mM

l-ascorbic-acid-2-phosphate (Sigma, St. Louis, MO); penicillin G (100 Units/ml, Invitrogen, Carlsbad, CA); streptomycin (100 µg/ml, Invitrogen); 2mM l-glutamine (Sigma) and 1ng/ml basic fibroblast growth factor (Instruchemie, Delfzijl, The Netherlands). Cells were cultured in incubator at 37 °C in a humidified atmosphere of 5% carbon dioxide.

After the four to five day culture period, non-adherent cells and α MEM proliferation medium were discarded. Adherent cells were thoroughly washed twice with PBS phosphate-buffered-saline (PBS, Sigma) and α MEM proliferation medium was refreshed. We proliferated adherent cells for two passages and cryopreserved them. The passage number was defined by every harvest with 0.25% trypsin/EDTA (GIBCO).

hMSCs expansion

Cryopreserved cells were thawed and hMSCs - passage 2 - were recounted and plated at 1,000 cells/cm² in 300 cm² T-flasks (T-300 flasks) in α MEM proliferation media. hMSCs were cultured in for one week with one refreshment of α MEM proliferation media.

Scaffold sterilization and conditioning for hMSCs culture

2D and 3D scaffolds were sterilized with 70% Ethanol solution for 15 min. After, scaffolds were washed and incubated at room temperature for two hours with sterile PBS. We repeated this washing step three times. Then, 2D and 3D scaffolds were incubated in α MEM proliferation media overnight at standard culture conditions before seeding.

Dynamic seeding of 2D and 3D scaffolds

Once hMSCs were semi confluent during expansion, hMSCs were harvested with 0.25% trypsin/EDTA. From the cell suspension, 200 µl were diluted in 10 ml of Isoton II diluent (Beckman Coulter, Fullerton, CA) and three drops of Zap-OGlobin II lytic reagent (Beckman Coulter) were added. The solutions were incubated for 30 min to maximize the effect of the lytic reagent, and subsequently, the nuclei of cells were counted in a particle count and size analyzer (Z2, Beckman Coulter). The size range of counted nuclei was set to between 6 to 10.5 µm according to the 95 % confidence interval of hMSCs nuclei size. After cell counting, a volume from the cell suspension equivalent to 2×10^5 hMSCs - passage 3 - were seeded per scaffold on six-well non-tissue-culture treated plates (10 cm² per well, Nunc). Bioreactor culture and static control required seeding 1.5×10^6 hMSCs.

To induce homogeneous seeding, the six-well plates were placed on a rocking

bed (Heidolph Instruments, Schwabach, Germany) at 30 RPM for four hours in standard culture conditions. After seeding, well plates were removed from the rocking bed and placed in an incubator or in the perfusion bioreactor.

hMSCs static culture on 2D and 3D scaffolds

Every well on the six well plate contained 2 ml of α MEM proliferation medium, which was refreshed every week. After dynamic seeding and thereafter, every other day, three 2D discs and three 3D scaffolds were removed from culture to obtain viable cell numbers. 2D discs and 3D scaffolds were washed with PBS before any further treatment was performed. In addition, a medium sample was drawn every other day to obtain dead cell numbers and a metabolic profile.

Perfusion Bioreactor Culture

A direct perfusion flow bioreactor configuration was used. The bioreactor was comprised of an inner and outer housings made of polycarbonate (Applikon Biotechnology BV, Schiedam, The Netherlands), where PEOT/PBT 8 mm diameter x 3 mm height cylindrical scaffolds were kept press-fit in the inner housing during cultivation. The bioreactor was connected to 3.2 mm PharMed tubing (Cole-palmer, The Netherlands), which was used throughout the system in a loop composed of: a supply vessel, 0.89 mm microbore tubing (Cole-palmer) used only on a pumphead (Masterflex, the Netherlands), fittings to connect 0.89 mm to 3.2 mm tubing, an oxygenator (explained below), the bioreactor, in-line oxygen and pH microsensors (Presens GmbH, Germany) and back to the supply vessel. One run was defined by four of these systems run in parallel for 8 days with medium refreshments twice a week, where each system contained an 8×3 mm cylindrical scaffold dynamically seeded with 1.5 million cells and connected independently to their own oxygenator, tubing and α MEM proliferation medium supply.

To achieve flows in the range of 0.1 to 1 ml/min, a pump head (Masterflex, The Netherlands) was connected to the pump (Masterflex, The Netherlands), where 0.89 microbore tubing (Cole Palmer) was used. The four bioreactor systems were placed in a temperature-controlled box and kept at 37° C, providing per run, four scaffolds ($n = 4$) with hMSCs for RNA extraction. These incubation units had to be supplied with a gas-controlled atmosphere, therefore, to supply the cells with oxygen and carbon dioxide an oxygenator was built. The oxygenator comprised a closed chamber containing a gas-permeable silicon tube. The gas environment in the chamber was kept at a constant level of 21% O₂ and 5% CO₂ and medium was pumped through the gas-permeable tube at a flow rate of 0.3 ml/min. This system maintained the pH (7.1) at the bioreactor outlet during the culture period.

Chemo-optic flow-through micro oxygen sensors (FTC-PSt-3; Presens GmbH,

Germany) that detect the quenching of luminescence by oxygen and an oxygen meter (Fibox-3; presens GmbH) were used as previously shown [26]. For 100% dissolved oxygen (DO) calibration, gas with the compositions mentioned above was supplied to the medium via the oxygenator. For 0 % DO calibration, nitrogen gas was supplied through the medium via the oxygenator. Flow through cell (FTC-HP8-S, Presens GmbH) connected to pH-1 mini (Presens GmbH) were used to measure the PH of the medium at the outlet of the culture chamber.

Metabolic profile and volume

Medium samples were obtained every other day for every donor from independent wells ($n = 3$). Glucose, lactate, and ammonia were measured in the Vitros DT60 II chemistry system (Ortho-Clinical Diagnostics, Tilburg, The Netherlands). From a starting volume of 2 ml, a volume change of 1.35×10^{-3} ml/h ($R^2 = 0.98$) was measured in six-well plates in a Sanyo incubator at 37 Celsius with 60% relative humidity. Concentrations measured were normalised to the volume changes.

Spontaneous degradation

All spontaneous degradation experiments included medium incubated at standard culture conditions, where metabolites were measured with their respective methods. Lactate-dehydrogenase (LDH) signal for dead cell numbers degraded linearly in time at a rate of 1.3×10^2 ($R^2 = 0.88$) LDH signal/h was measured from three replicates per data point. LDH signals were normalized for every donor to LDH spontaneous degradation before dead cell numbers were calculated.

Sample preparation for biochemical analysis

PEOT/PBT 2D discs and 3D scaffolds were washed with PBS and frozen overnight at -80°C . Before DNA, glucosaminoglycans (GAG), and total collagen quantification: All samples were digested for 16 h at 56°C with 1mg/ml proteinase K (Sigma-Aldrich) in Tris/EDTA buffer (pH 7.6). This solution also contained 18.5 $\mu\text{g/ml}$ iodoacetamide and $\mu\text{g/ml}$ pepstatin A (Sigma-Aldrich).

Viable and dead hMSCs

Viable cell numbers were obtained with Cyquant DNA assay (Invitrogen). Cell numbers were calibrated for every hMSCs donor by measuring the DNA signal ($n = 3$) of six cell numbers from 1×10^4 to 3×10^5 cells. Cell numbers were plotted against DNA amount and analyzed by linear regression to obtain DNA signal/cell number ratio (donor 1: 4.9×10^{-1} , $R^2 = 0.96$; donor 2: 4.2×10^{-1} , $R^2 = 0.91$; and donor 3: 2.6×10^{-1} , $R^2 = 0.94$). DNA from three scaffolds per donor was obtained to obtain each cell number data point. Cell numbers for every donor were obtained by dividing

the signal in time by their respective DNA signal/cell number ratio.

Cell death was quantified with medium analysis of the LDH signal with the Cytotox-one Homogeneous Membrane Integrity Assay (Promega Corporation, Madison, WI). Dead cell numbers were plotted against LDH signal ($n = 3$) for each of five cell numbers from 2×10^3 to 2.5×10^5 cells. The slope estimated from linear regression corresponded to the LDH signal/cell number ratio (donor 1: 1.51×10^{-1} , $R^2 = 0.92$; donor 2: 6.99×10^{-1} , $R^2 = 0.94$; and donor 3: 1.15, $R^2 = 0.92$). From three runs per donor i.e. three wells measured per measurement day, four medium samples per run ($n = 12$) were obtained and its LDH signal measured in time. Dead cell numbers for every donor were obtained by dividing the signal in time by their respective LDH signal/cell ratio.

Glucosaminoglycans (GAGs) and collagen quantification

After sample preparation for biochemical analysis (above), total collagen or content of hydroxyproline was quantified for each 2D and 3D sample. GAGs were quantified on 2D discs and 3D scaffolds with 9-dimethylmethylene blue chloride (DMMB, Sigma-Aldrich) staining in PBE buffer: 14.2 g/l Na_2HPO_4 and 3.72 g/l Na_2EDTA , pH 6.5. A micro plate reader (Bio-TEK instruments) was used to spectrophotometrically determine absorbance at 520 nm. Chondroitin sulfate was used as standard.

For collagen quantification, 35 μl /sample were deposited in a 96 well plate. To each well, 75 μl of Chloramin T were added and placed on a shaker for 20 min at RT. Then, 75 μl of DMBA were mixed for 20 min at 60 °C. after cooling to RT, absorbance at 570 nm was measured.

Chloramine T was composed of: 0.49 g of Chloramine T (Merck, The Netherlands), 3.5 ml of n-propanol, 3,5 ml of RNase-free water, and 28 ml of stockbuffer. Chloramine T was vortexed in the RNase-free water before adding the stockbuffer. The stockbuffer was composed of: 0.24 M of Citric acid (Fluka, The Netherlands), 0.88 M of NaAc.trihydrate (Merck), 0.85 M of NaOH (Merck). The pH of the stockbuffer was adjusted to 6.1 with HAc (Merck). DMBA solution consisted of: 6g of Dimethylaminobenzoaldehyde (Merck), 24.78 ml of n-propanol, 10.02 ml of 60% perchloric acid (Merck).

P21 and p27 qPCR

RNA was isolated with RNeasy mini kit (Qiagen, The Netherlands). SYBR green (Invitrogen) on a Light Cycler (Roche, The Netherlands) were used to perform qPCR, where data were analyzed by using Light Cycler software version 3.5.3. The fit point method was used by setting the noise band to the exponential phase of the reaction,

thereby excluding background fluorescence. Expression of p21 and p27 genes was calculated relative to 18s rRNA levels.

Total RNA was isolated using Trizol according to the manufacturer's protocol. The quality and quantity of RNA was analyzed by gel electrophoresis and spectrophotometry. One microgram of RNA was used for cDNA synthesis using iScript cDNA synthesis kit (BioRad) according to the manufacturer's protocol. PCR was performed on a Light Cycler real time PCR machine (Roche) using SYBR green I master mix (Invitrogen). Data was analyzed using Light Cycler software version 3.5.3, using fit point method by setting the noise band to the exponential phase of the reaction to exclude background fluorescence.

Histological Analysis

Scaffold samples were fixed for 30 min in 1.5 % glutaraldehyde (Merck) in 0.14 M cacodylate buffer (PH = 7.2 – 7.4). then, scaffolds were dehydrated in sequential ethanol series, embedded in glycol-methacrylate (Merck) and cut using a microtome into 5 μm sections. Sections were then stained with Alcian blue (Sigma-Aldrich) to visualize GAGs and counterstained with haematoxylin (Sigma-Aldrich) to visualize the nuclei; sections were also stained with Safranin-O (Sigma-Aldrich) to visualize sulphated GAGs and counterstained with haematoxylin (Sigma-Aldrich) and fast green (Merck) to visualize cell nuclei and cytoplasm, respectively. Mounted slides were examined through light microscopy.

For imaging 3D scaffolds at low resolution, after fixation, scaffolds were stained with 1 % methylene blue (Sigma-Aldrich) to visualize cell membranes on 3D scaffolds through light microscopy.

Click-iT® Edu Alexa Fluor® 488 Imaging Kit (Invitrogen) was used to image the DNA synthesis by proliferating hMSCs in 3D scaffolds. 3D scaffolds with hMSCs were incubated in a 1:1 solution of EDU in proliferation medium at 37 °C for 18 h. Then, samples were fixed in 1% formalin (Sigma-Aldrich) for 30 min and embedded in Tissue-Tek OCT (Qiagen), and placed at – 80 C° overnight. 5 μm sections were then cut with a cryomicrotome. Subsequently, sections were permeabilized and washed with the secondary antibody (horseradish peroxidase conjugated goat-anti-human immunoglobulin antibody, Dako, Denmark). Sections were counterstained with dapi (Invitrogen). We used fluorescent microscopy to visualize EDU (DNA, green) and DAPI (cell nuclei, blue) signals.

Statistical analysis

Statistical significance was set at $p < 0.05$ and processed as described in the mathematical model section. All data points for viable and dead cell numbers, glu-

cosaminoglycans, collagen, glucose, lactate, ammonia are based on replicates for each of three parallel experiments i.e. three scaffolds used for cell number quantification per data point or three medium samples taken from hMSCs cultures per data point. Error bars in graphs with experimental data represent the standard deviation of measurements.

Computational fluid dynamics (CFD)

The diffusion-convection equation was solved as defined by Eq. 1a:

$$\frac{\partial C}{\partial t} = D \cdot \nabla^2 \cdot C - v \cdot \nabla \cdot C \quad (1a)$$

where C is the bulk concentration of glucose (mol/m^3), t is the time (s), D is the diffusion constant of glucose (m^2/s), ∇ is the del operator. When convection is present, v is the velocity field (m/s). In addition, in the boundary condition, the transport of material towards the surface equals to the glucose consumption rate by the cells on the 2D surface or on the surface at the edge of a pore:

$$D \cdot \nabla \cdot C = -R \quad (1b)$$

Where R is the consumption rate of glucose by hMSCs ($\text{moles}/\text{m}^2/\text{s}$). The initial concentration for any place was set to $C(t=0, \dots) = C_0$.

Glucose consumed by hMSCs in four culture conditions was modeled: (1) 2D static, (2) 3D static (3) 3D pore in static culture and (4) 3D pore in the perfusion bioreactor. Walls in different conditions were considered rigid and impermeable. For condition 4, the culture medium flows in the positive z -direction, where at $z = 0$, the boundary condition was set to specific inlet velocity and concentration C_0 with only a z -component.

In all conditions, glucose diffusion constant (D) was $9 \times 10^{-10} \text{ m}^2/\text{s}$ [27]. Initial concentration of glucose ($C_0 = 4 \text{ mmol}/\text{l}$) was obtained from the average bulk concentration of glucose on day 8 for 2D and 3D cultures (Fig. 6C), which was approximately 8×10^{-6} total moles of glucose in a total volume of 2 ml of culture medium or 4 mmol/l.

For conditions 1 and 2, glucose concentrations were proportional to the consumption by hMSCs as estimated from kinetic experiments of cell numbers and glucose metabolism as shown on Fig. 5A, 5B, 6C and 6D. Thus, glucose consumption (q_g) [$\text{moles}/\text{cell}/\text{h}$] in 2D and 3D cultures was multiplied by the respective number of cells on day 8. Since the area of 2D and 3D scaffolds was known (Fig. 4C), glucose

fluxes [mol/m²/s] were obtained for static cultures. Glucose fluxes were equal to: 2.1×10^{-8} in 2D and 7.3×10^{-8} in 3D.

For conditions 3 and 4, the same values for glucose D and $C0$ constants were used as for conditions 1 and 2. Cells were assumed to be on the surface of each of the 4 fibers or sides of a pore with radius 0.4 mm. cell layer was 5 μm in height. The glucose flux or glucose consumption by hMSCs on the surface of the pore walls could not be measured. Thus, this was varied across several magnitudes that increased or decreased the sizes of boundary layers. As a representative value of this trend for conditions 3 and 4, glucose consumption on the walls of the pore was assumed to equal to 1.94×10^{-13} mol/mm³/s. For condition 4, the bottom boundary was defined as the inlet ($v=0.01$ m/s) with the flow used in bioreactor experiments ($F = 0.33\text{ml/min}$).

CFD models of the fluid flow in culture conditions were set-up and solved in the MEMS module (microfluidics – flow with species transport) in Comsol Multiphysics version 3.5a software (Comsol, The Netherlands).

2D Disc and 3D Scaffold Design

The same area in 2D discs and 3D scaffolds was obtained on the assumption that the ratio of the volume of a porous cylinder B (V_B) to the volume of a porous cylinder C (V_C) equals the ratio of the cross sectional area of a porous cylinder B (A_B) to the cross sectional area of a porous cylinder C (A_C), as depicted in Eq. 2.

$$\frac{V_B}{V_C} = \frac{A_B}{A_C} \quad (2)$$

From Eq. 2, we obtained Eq. 3,

$$r_C = r_B \cdot \sqrt{\frac{A_C}{A_B}} \quad (3)$$

where A_B (2.75 cm²) is the area calculated with μCT of a porous scaffold of 0.4 cm radius (r_B). A_C is the target area (3.79 cm²) and r_C its corresponding unknown radius. With Eq. 3, we estimated a radius equal to 0.47 cm in the 3D scaffold. Figure 4C shows the 3D scaffold radius to area relation. On this figure, μCT experimentally confirmed that a r_C of 0.47 cm produced an area equal to 3.8 ± 0.47 cm². All other areas on can be deduced in the same manner. μCT measurements showed that the surface area of 2D discs was equal to 3.87 ± 0.05 cm², thereby making 2D discs and 3D scaffold surface areas comparable.

Kinetics Mathematical model

The principles to model were chosen based on literature on mammalian cell cultures [28-31]. Culture of hMSCs on a 2D surface or a 3D scaffold were considered batch systems, where cells grow on their metabolites. The system can be described with the set of mass balances (Eq. 4 and 5). The viable cell numbers are given by:

$$\frac{dX_v}{dt} = \mu \cdot X_v \quad (4)$$

Where, $\mu = \mu_v - \mu_d$

Eq. (4) describes the change of viable cells in time in 2D surfaces and 3D scaffolds, where X_v [Total] is the viable cell number, μ [h^{-1}] is the specific growth rate, μ_v [h^{-1}] is the specific growth rate of viable cells and μ_d [h^{-1}] is the death rate of viable cells. μ_v and μ_d cannot be estimated as independent variable. Thus μ was estimated and used to predict viable cell numbers.

The mass balances of metabolites are given by:

$$\frac{dX_m}{dt} = q_m \cdot X_v \quad (5)$$

where the subscript m refers to either: glucose (g), glucosaminoglycans (y) and collagen (c). q_m refers to the reaction rate of m per average cell per h, q_m is constant and may be positive or negative (\pm) depending on whether m is produced or consumed, respectively. We assumed that throughout culture glucose would be consumed; while glucosaminoglycans and collagen would be produced.

Mathematical modelling and parameter estimation

The mathematical model (Eq. 4 and 5) comprise a set of ordinary differential equations (ODEs) which were solved with a standard differential equation solver in Matlab (ode45 in version 7.0.4 release 2007a; Mathworks, Natick, MA) on a windows-based system. The initial values for solving the differential equation were set to the seeding density and the experimentally determined composition (glucose, lactate and ammonia) in fresh α MEM proliferation medium from three medium samples. Mathematical model parameter values for the three donors were obtained by nonlinear least squares regression which minimizes the sum of the quadratic error over an experiment (Matlab function `nlinfit`). Next, the 95 % confidence intervals for the parameters were calculated (Matlab function `nlparci`). The experimentally obtained initial values had a low variation and were not considered as parameters to

be included in the nonlinear least squares regression.

Results and Discussion

Proliferation patterns

To address whether concentration gradients can direct patterns of proliferation, 3DF was used to make PEOT/PBT cylindrical scaffolds [20] which provided a well defined 3D structure, fibre, and pore architecture. This allowed us to seed and culture hMSCs in a controlled volume, where hMSCs proliferated. The DNA of proliferating hMSCs showed that in the exterior (Fig. 1A) of the 3D scaffold, there were proliferating hMSCs (Fig. 1B and C) whereas in the interior (Fig. 1A) of the 3D scaffold proliferating hMSCs were not readily identifiable (Fig. 1D and E). This showed that proliferation of hMSCs was not evenly distributed across the 3D scaffold volume with patterns of proliferation occurring spatially.

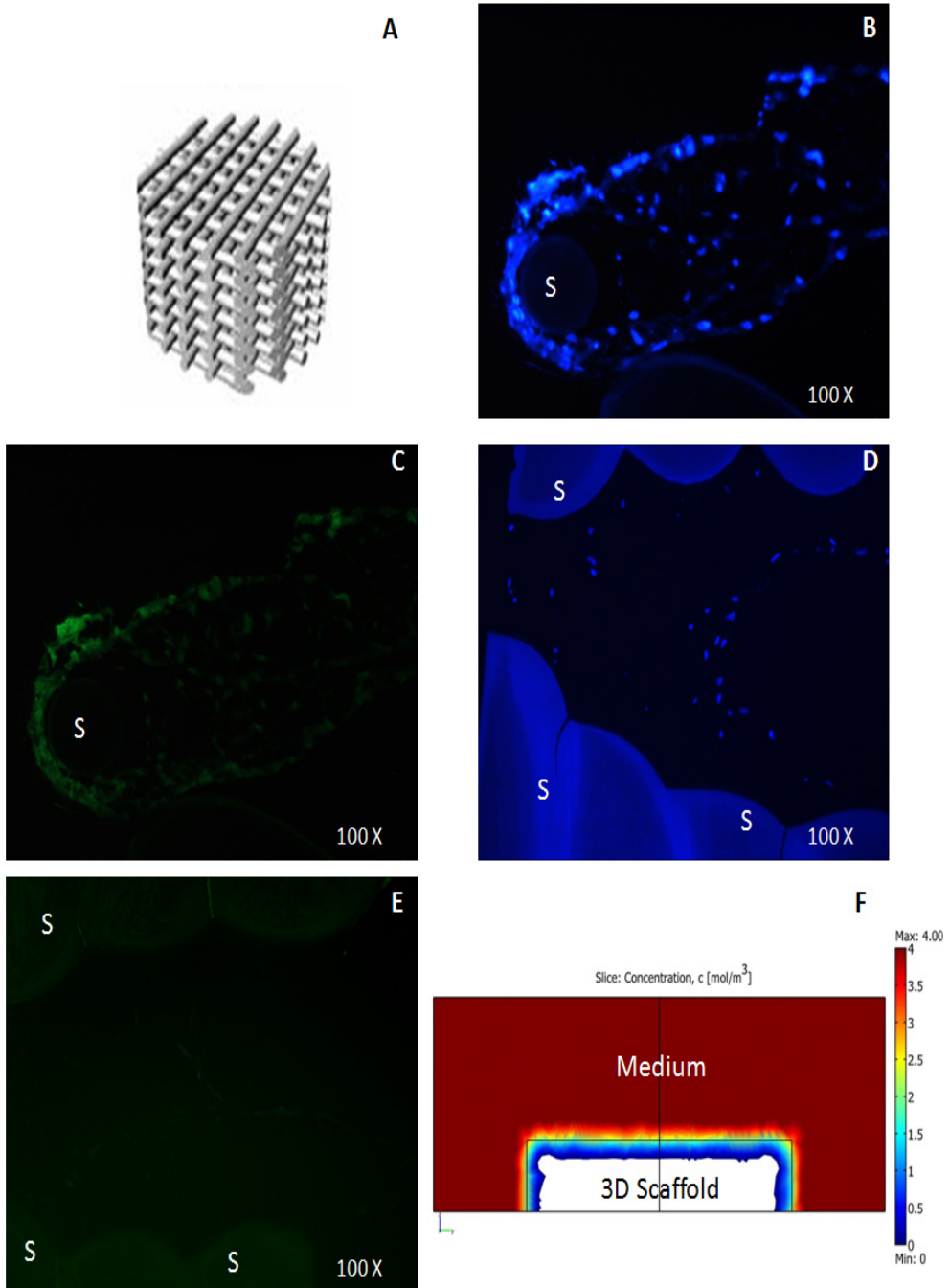


Figure 1 3D scaffold cultured with hMSCs and glucose gradient model for the total scaffold volume. A: 3DF scaffold (S) made of fibers with interconnected pores. Exterior refers to the surface of the 3DF scaffold volume. Interior refers to inside the 3DF scaffold volume. B: Nuclei fluorescently labeled (blue) of hMSCs (Day 8) located in the exterior of the 3DF scaffold. C: DNA fluorescently labeled (green) of proliferating hMSCs (Day 8) located in the exterior

of the 3DF scaffold. **D**: Nuclei fluorescently labeled (blue) of hMSCs (Day 8) located in the interior of the 3DF scaffold. **E**: DNA fluorescently labeled (green) of proliferating hMSCs (Day 8) located in the interior of the 3DF scaffold. **F**: Model of concentration gradient considering glucose diffusion (D) and hMSCs consumption (R) throughout the total volume of the 3D scaffold in static culture (Side view).

Nutrients, growth factors, and mitogens determine whether cells proliferate, undergo quiescence, or die [32]. Thereby, taking glucose as a model molecule with well known reaction rates by hMSCs [33-35], a computational fluid dynamics (CFD) model was made (Eq. 1) to illustrate the concentration gradients due to diffusive transport for the 3D scaffold total volume (Fig. 1F). To increase the fidelity of the CFD model, experiments were performed to measure glucose and hMSCs proliferation in time. This CFD model is representative of glucose reaction rates on day 8 (See M&M) after medium refreshment on day 6 of hMSCs culture. The CFD model showed that regions of high glucose concentration corresponded well with regions where dividing hMSCs were detected (Fig. 1B, C and F). Thus, this showed that in addition to form and mechanical stress [36], regions of high and low molecular concentration could induce proliferation patterns.

Migration patterns

Proliferation patterns were not limited to the outside and inside of the scaffold volume. The rectangular pore geometry of the 3D scaffold showed that hMSCs migrated towards regions of high molecular concentration at the center of the pore (Fig. 2A). Then, cell migration was compared with the CFD model of the glucose gradient inside the rectangular pore (Fig. 2B). This comparison showed that there was a strong correlation between hMSCs migration into the pore and width of the boundary layer (Fig 2B). The CFD model is representative of the glucose gradient formation at the moment before hMSCs migrate. These evidence showed that regions of high nutrient availability corresponded with the direction towards which cells migrated. In this time-dependent process, the region of high nutrient availability in the centre of the 3D pore became smaller as cells surrounded it from all sides in a circular 3D pattern. This circular pattern spanned the XYZ axis of the pore and continued until achieving a confluent pore. This confirmed that with hMSCs form can be a direct resultant and consequence of growth [37].

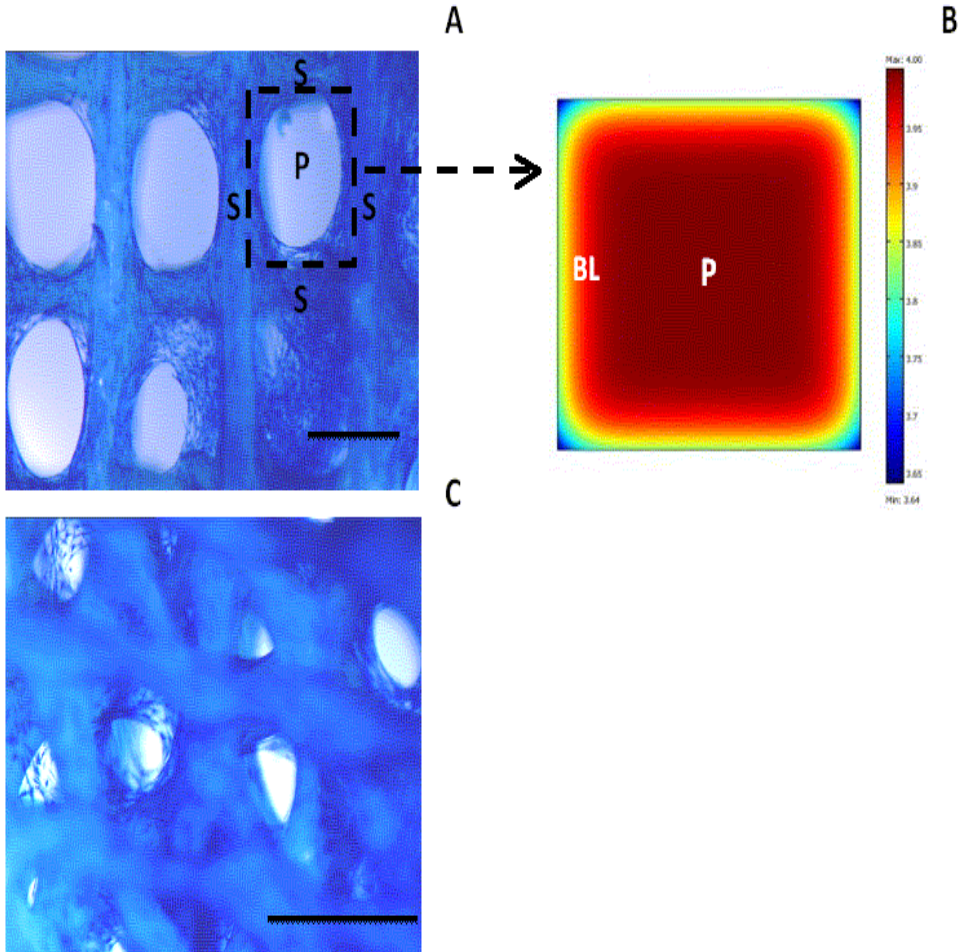


Figure 2 hMSCs migration into the center of pore (P) of the 3D scaffold (S) on day 8 and glucose gradient model **A**: Six pores of a 3D scaffold with hMSCs stained with methylene blue. Scale bar equals 500 μm . **B**: Model of concentration gradient considering glucose diffusion (D) and hMSCs consumption (R) around the 3D scaffold pore (800x800 μm). Boundary layer (BL). Comsol model: Cell layer 5 micron in height and covering the surface. $D = 9 \times 10^{-10} \text{ m}^2/\text{s}$, $R = -3.15 \times 10^{-12} \text{ mol/L/s}$, $C_0 = 4 \text{ mmol/L}$. **C**: hMSCs migrate towards the center of the pore in 3D scaffolds with a 45° pore architecture. Methylene blue stained. Scale bar equals 500 μm .

To determine whether hMSCs organization into the pore was due to pore geometry or high molecular concentrations, hMSCs were cultured in 3D scaffolds with 45° angle pore architecture (Fig. 2C). This pore architecture also showed hMSCs organization into the pore. These showed that cell organization towards the center of the pore was independent of pore-size and architecture.

To determine if hMSCs migration into the rectangular pore could be controlled,

convection in the scaffold was introduced. Convection varies the boundary layer and forces the region of high molecular concentrations closer to the fibers, thereby preventing hMSCs migration. To test this, hMSCs were cultured in a perfusion bioreactor (Fig. 3A) and the glucose gradient in a pore was illustrated with a CFD model (Fig. 3B). Assuming the same glucose consumption by hMSCs in both models with and without convection (Fig. 2B and 3B, respectively), it was determined that there would be a thinner boundary layer under convection (Fig. 3B). Convection did not keep hMSCs from migrating into the pores entirely. Instead, hMSCs migration into the pore appeared slower and more densely packed in the bioreactor than in 3D static culture (Fig. 3C). hMSCs proliferation in the bioreactor was monitored through oxygen tension and pH. Dissolved oxygen (DO) (Fig. 3D) showed oxygen consumption by hMSCs, where a 4-day lag and 3-day proliferation phases could be observed. It is important to note that convection in the bioreactor generated also shear stress. This made difficult to distinguish the effects of molecular concentrations and shear stress on hMSCs. To distinguish between molecular concentrations and shear stress, hMSCs proliferation kinetics were evaluated.

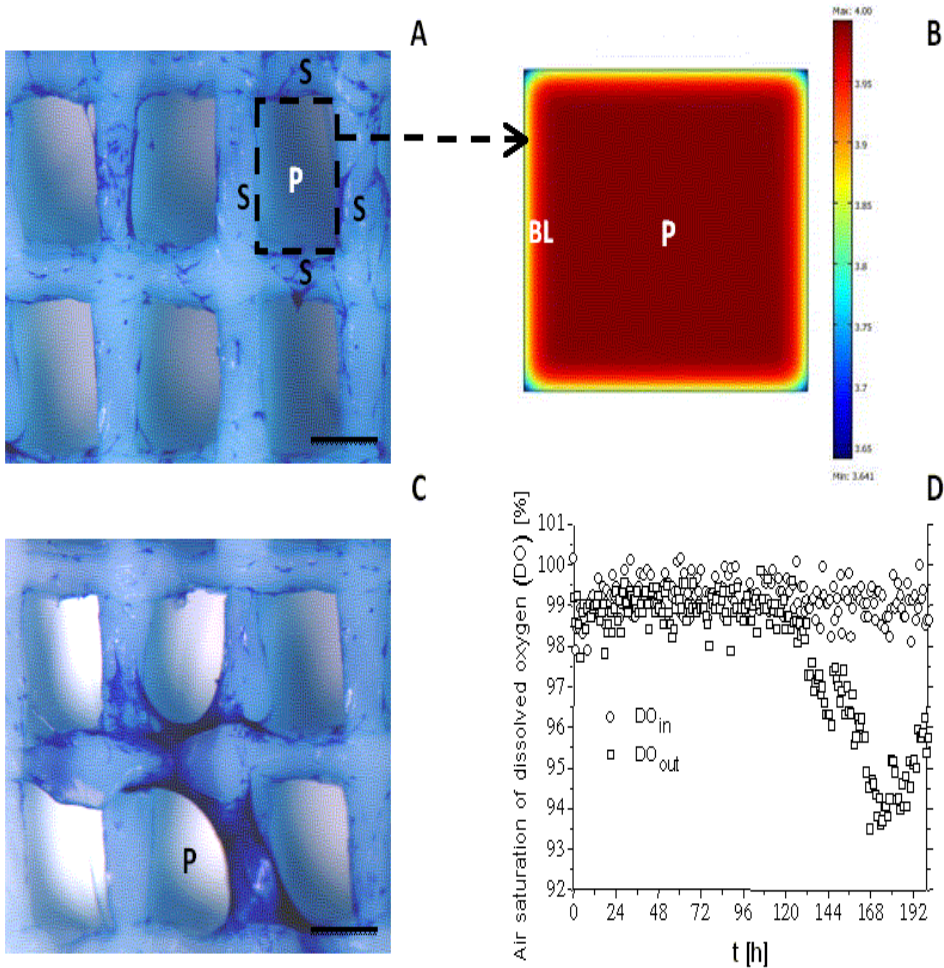


Figure 3 3D scaffolds cultured in a perfusion bioreactor (0.3 ml/min), oxygen tension and glucose gradient model. **A:** 2 days perfusion culture. **B:** Model of concentration gradient considering glucose diffusion (D) and hMSCs consumption (R) around the 3D scaffold pore ($800 \times 800 \mu\text{m}$) with perfusion through the pore. Boundary layer (BL). Comsol model: Cell layer $5 \mu\text{m}$ in height and covering the surface. $D = 9 \times 10^{-10} \text{ m}^2/\text{s}$, $R = -3.15 \times 10^{-12} \text{ mol/L/s}$, $C_0 = 4 \text{ mmol/L}$. **C:** 5 days perfusion culture. hMSCs were stained with methylene blue **D:** Dissolved oxygen during hMSCs culture in the perfusion bioreactor measured at the inlet (DO_{in}) and outlet (DO_{out}) of the culture chamber. Mean of 4 runs.

Kinetics

Concentration gradients occur spatially and in time [1, 2]. and have been shown to influence chondrocytes' kinetics [10]. In addition, oxygen availability has been shown to regulate MSCs proliferation [35]. Thus, kinetics were used to link hMSCs proliferation with molecular concentrations. For this, we designed an experiment

where hMSCs would be cultured statically under both high and low nutrient availability. It was expected that there would be more proliferation under higher nutrient availability. Based on the CFD models of glucose, 2D surfaces (Fig. 4A) have a higher nutrient availability than 3D scaffolds (Fig. 1F). Therefore, hMSCs' kinetics were explored on both 2D surface and 3D scaffolds to induce higher (Fig. 4A) and lower (Fig. 1F) nutrient availability, respectively.

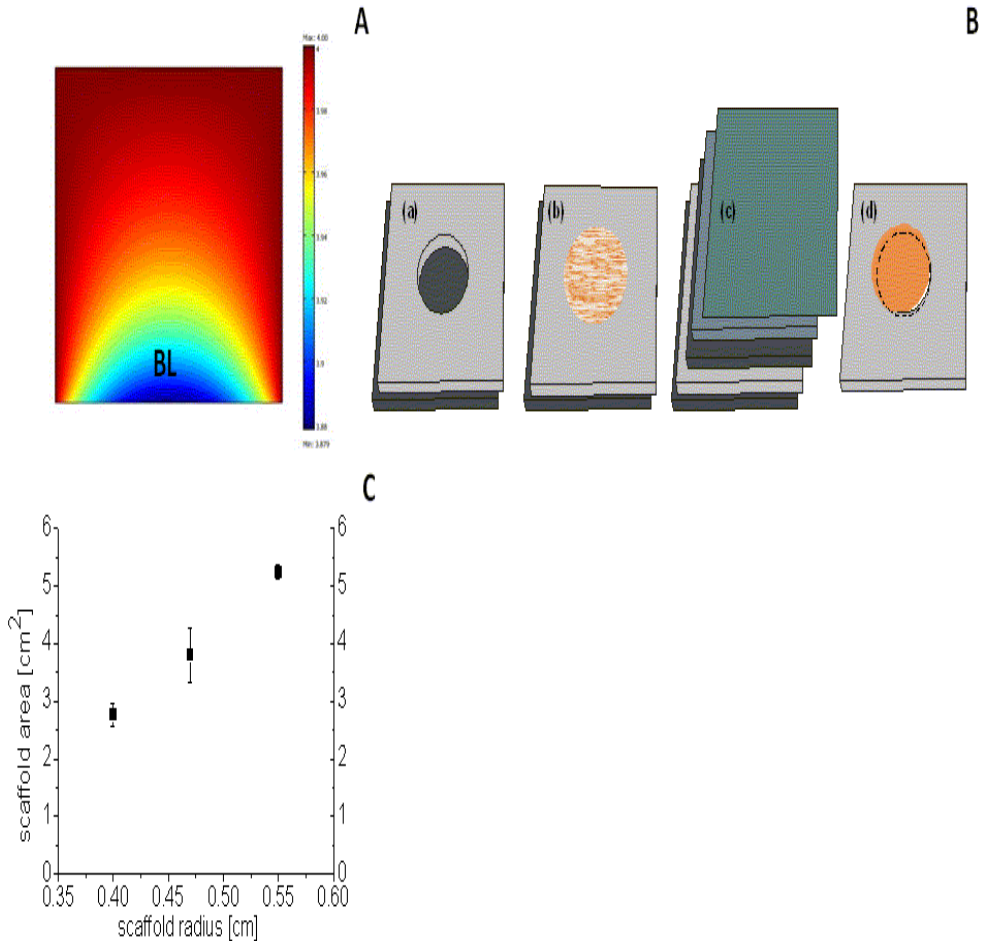


Figure 4 **A**: Model of concentration gradients of glucose on 2D static culture (Side view). Boundary layer (BL). The total vertical distance depicting the concentration gradient was 400 μm. **B**: 2D disc fabrication (a) Stainless steel mold placed onto silicon support , (b) Small fragments of 300PEOT55PBT45 are placed in the cavities of the mould in sufficient quantity to completely fill the cavities once the polymer has been melted, (c) A second silicon wafer is used as support to “sandwich” the mold. It follows the placements of a rubber cushion to uniformly distribute the pressure and an aluminum foil layer to prevent adhesion to the plates of the press. (d) The stack is manually separated and the 2D 300PEOT55PBT45 substrates removed from the mold. **C**: Surface areas vs. radius of 3D scaffolds measured with μCT.

The seeding density (cells/cm²) has known effects on hMSCs' proliferation [38] and differentiation [13]. This was controlled by making 2D surfaces (Fig. 4B) with a comparable attachment-surface area as 3D scaffolds. This was accomplished with μ CT scans of 3D scaffolds. From these scans, it was determined that the attachment area was proportional to the radius of the 3D scaffold (Fig. 4C) according to Eq. 2 and 3. 2D surfaces were made to match the 3D scaffold area while maintaining similar processing parameters as 3D scaffolds (see M&M).

Kinetics experiments included several hMSCs donors seeded on both 2D surfaces and 3D scaffolds. Donor dependency was observed for the seeding density and seeding efficiency (Table 1). In spite of that, for the same donor, hMSCs on both 2D discs and 3D scaffolds started proliferation at a comparable seeding density.

Table 1 Seeding efficiency and seeding density of three hMSCs donors on 2D discs and 3D scaffolds.

Donor	2D		3D	
	Seeding efficiency [%]	Seeding density [cells/cm ²] × 10 ³	Seeding efficiency [%]	Seeding density [cells/cm ²] × 10 ³
1	10.93	5.68	15.91	9.01
2	12.74	6.62	7.97	4.51
3	16.95	8.81	12.84	7.28
Mean	13.54	7.04	12.24	6.93
SD	3.09	1.60	4.01	2.27

Proliferation kinetics were studied in time by measuring cell numbers (Fig. 5A-B) and analyzing the data through mass balances for cell numbers with a proliferation kinetics model (Eq. 4) [33]. Cell numbers were higher on 2D surfaces than on 3D scaffolds (Fig. 5A). The kinetics model fit was poor for 2D surfaces and acceptable for cells on 3D scaffolds. Consequently, large standard deviations were obtained for specific growth rates (Fig. 5B). Despite the fit, average specific growth rates were higher on 2D surfaces (Fig. 5B). These showed that there were more cells and faster proliferation kinetics at higher nutrient availability. Since the viable cell numbers could be underestimated in the event of cell death, cell death was quantified (Fig. 5C). The fraction of dead cells (dead/(dead + viable)) averaged 0.12 ± 0.04 in 2D and 0.16 ± 0.02 in 3D cultures before 300 h. After 300 h, the fraction of dead cells in 3D cultures increased to 0.4 ± 0.06 and remained around 0.12 ± 0.04 in 2D. Consequently, cell death in 3D scaffolds could only account for low cell numbers after 300 h, time upon which high concentrations of ammonia and lactate (Fig. 5D-E) rose to harmful levels to hMSCs [39]. Thus, these data showed two interrelated aspects: One, hMSCs proliferated more actively under higher nutrient availability. Two: hM-

SCs showed a similar amount of death in 2D and 3D cultures for 300 h despite steeper gradients in 3D scaffolds.

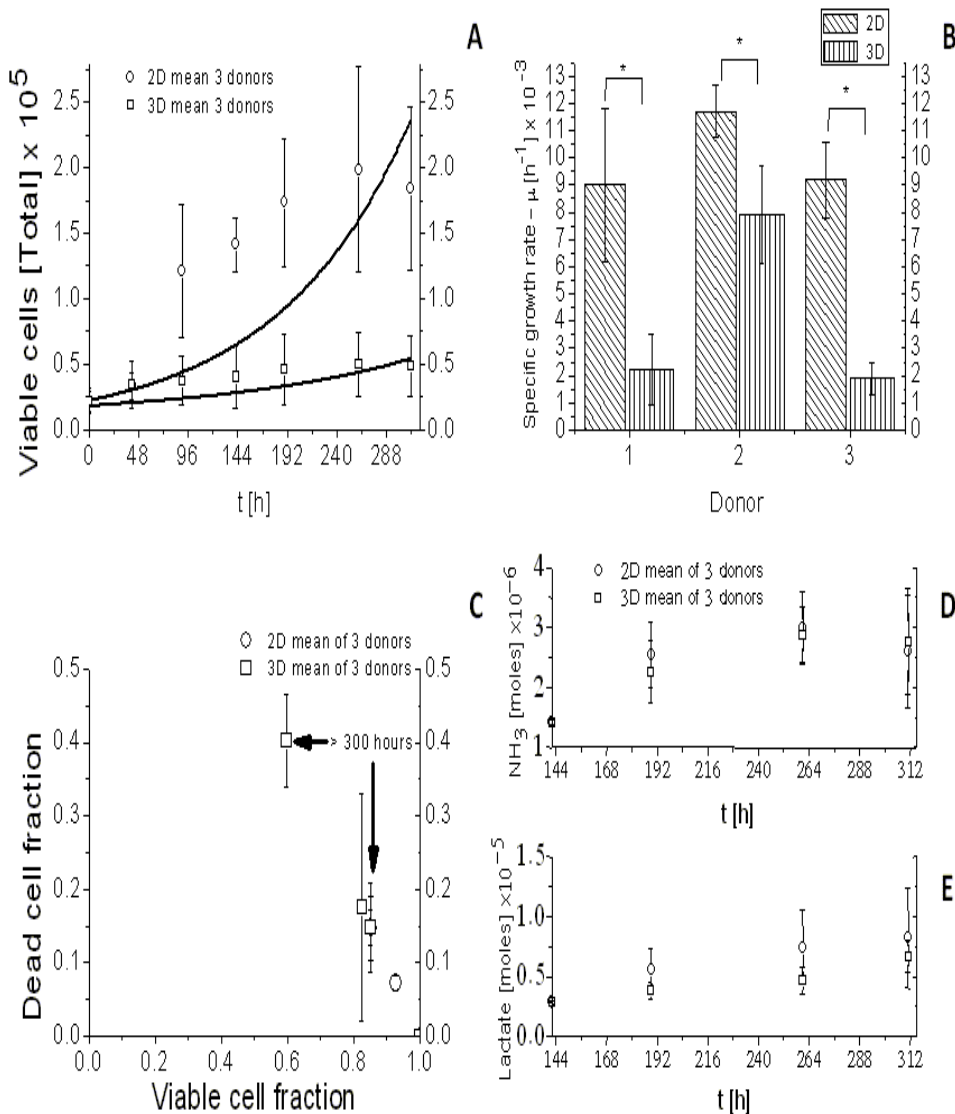


Figure 5 **A**: Viable cell numbers on 2D discs (\circ) and 3D (\square) scaffolds of three hMSCs donors. Kinetics model fit of cell numbers on 2D discs (—) and 3D (—) scaffolds. **B**: Box plot with specific growth rates (μ) of three donors on 2D discs and 3D scaffolds with 95 % confidence interval. **C**: Dead cell vs. viable cell fractions in 2D (\circ) and 3D (\square) cultures. **D**: Ammonia (NH_3) in 2D (\circ) and 3D (\square) cultures after medium refreshment at 140 h. **E**: Lactate in 2D (\circ) and 3D (\square) cultures after medium refreshment at 140 h.

This suggested that control of hMSCs population growth occurs through density-dependent contact inhibition. According to Alberts *et al* (2008), this involves the

depletion of growth factors, mitogens, and nutrients around a cell, by each cell in the population resulting in deprivation to its neighbours [32]. This depletion can block hMSCs entry into the cell cycle [32]. This could explain the slower hMSCs growth rates in 3D scaffolds (Fig. 5B). Therefore, the expressions of p21 and p27 genes were quantified for all cultures because these genes have been shown to be involved in the regulation of proliferation and differentiation in many tissues [40-44]. p21 expression was highest in 3D static, but not significantly different from 2D or 3D bioreactor (Fig. 6A). On the other hand, p27 expression was lowest in 3D static, but only significantly when compared to 2D (Fig. 6B). Increased expression of p27 in differentiated stem cells [40] suggests that hMSCs in 2D surfaces and 3D scaffolds may have differentiated. This could have been stimulated by the higher number of cells in 2D and shear stress [45] in the bioreactor. In addition, p21 and p27 expression could be shadowed by proliferating and non-proliferating populations of hMSCs within the 3D scaffold (Fig. 1).

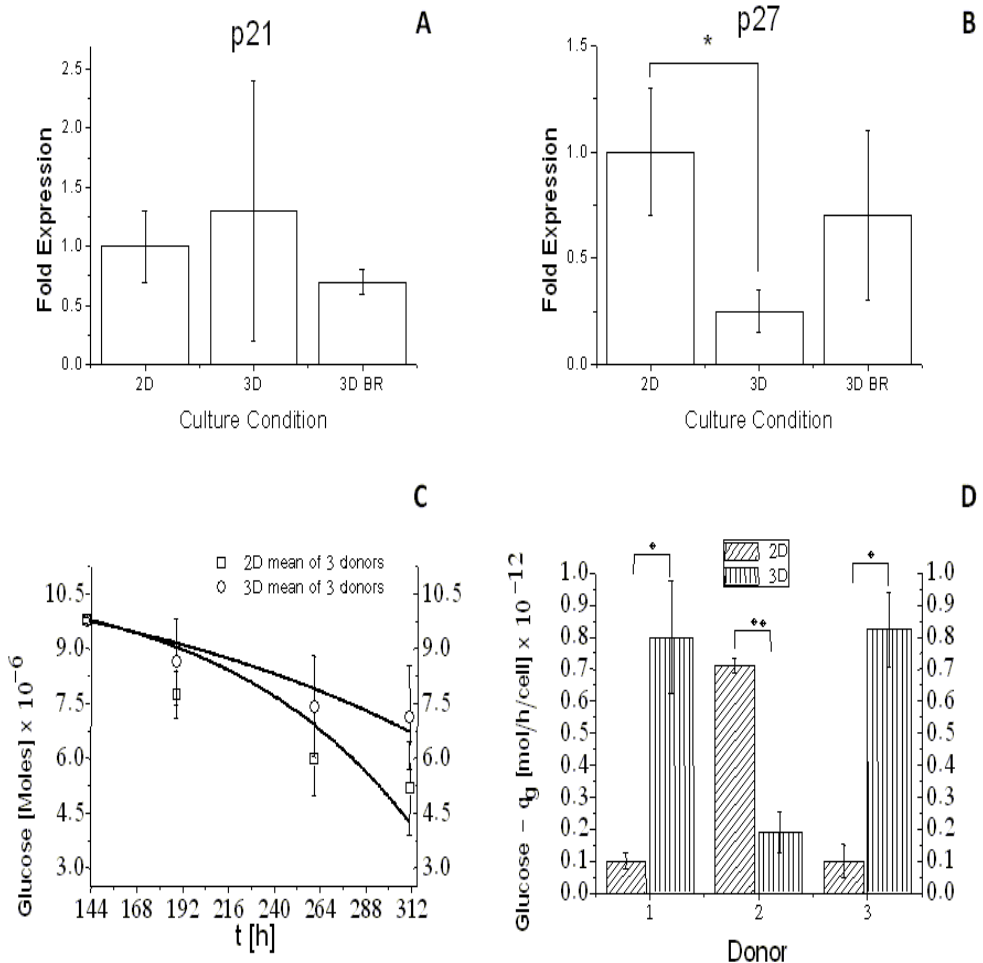


Figure 6 **A**: p21 gene expression in 2D and 3D static and bioreactor (3D BR) cultures. **B**: p27 gene expression in 2D and 3D static and bioreactor (3D BR) cultures. Relative fold expression between three conditions. Representative of 2 donors. Significance was estimated with ANOVA. **C**: Total moles of glucose in 2D (□) and 3D (○) cultures. Kinetics model fit of glucose in 2D (—) and 3D (—) cultures. Glucose concentrations were normalized to a 2 ml culture volume. Initial glucose concentration equals 5 mmol/l. **D**: Box plot of glucose consumption rate (μg) of three donors in 2D discs and 3D scaffolds with 95 % confidence interval.

To understand how hMSCs used their available resources in the presence of concentration gradients, the bulk concentration of glucose was measured in time (Fig. 6C-D) and analyzed with a metabolism kinetics model (Eq. 5) [33]. Due to the higher number of cells on 2D surfaces after medium refreshment (144 h), glucose decreased faster on 2D surfaces than in 3D scaffolds (Fig. 6C). However, the glucose consumption per cell per h (Fig. 6D) showed that there was a significantly

higher consumption in two donors cultured on 3D scaffolds. In addition, there was a significantly higher glucose consumption in one donor on 2D surfaces. This suggested that extra glucose consumption could be used as energy source for extracellular matrix (ECM) production, which appeared to support hMSCs migration into the rectangular pores in 3D scaffolds. Due to their natural importance in the ECM [46, 47], glucosaminoglycans (GAG) and hydroxyproline or total collagen (Fig. 7) were measured in time and analyzed with the kinetics model (Eq. 5). The results indicated that there was not significantly higher GAG or collagen production per cell per h on 2D surfaces or 3D scaffolds (Fig. 7 B and D). In addition, the results showed that GAG could be detected in all hMSCs donors (Fig 7B). On the other hand, collagen could be detected in all 2D samples and in only one donor of the 3D scaffold (Fig. 7D). These evidence suggested that hMSCs did not differentiate on 3D scaffolds. This also suggested that hMSCs migration into the pores was supported by an ECM composed mostly of GAG. Extra glucose consumption in 3D scaffolds was not used to increase cell proliferation or ECM production in 3D scaffolds. Glucose may have been channelled to pathways involved in the non-random organization of hMSCs into patterns throughout the scaffold's interconnected pores.

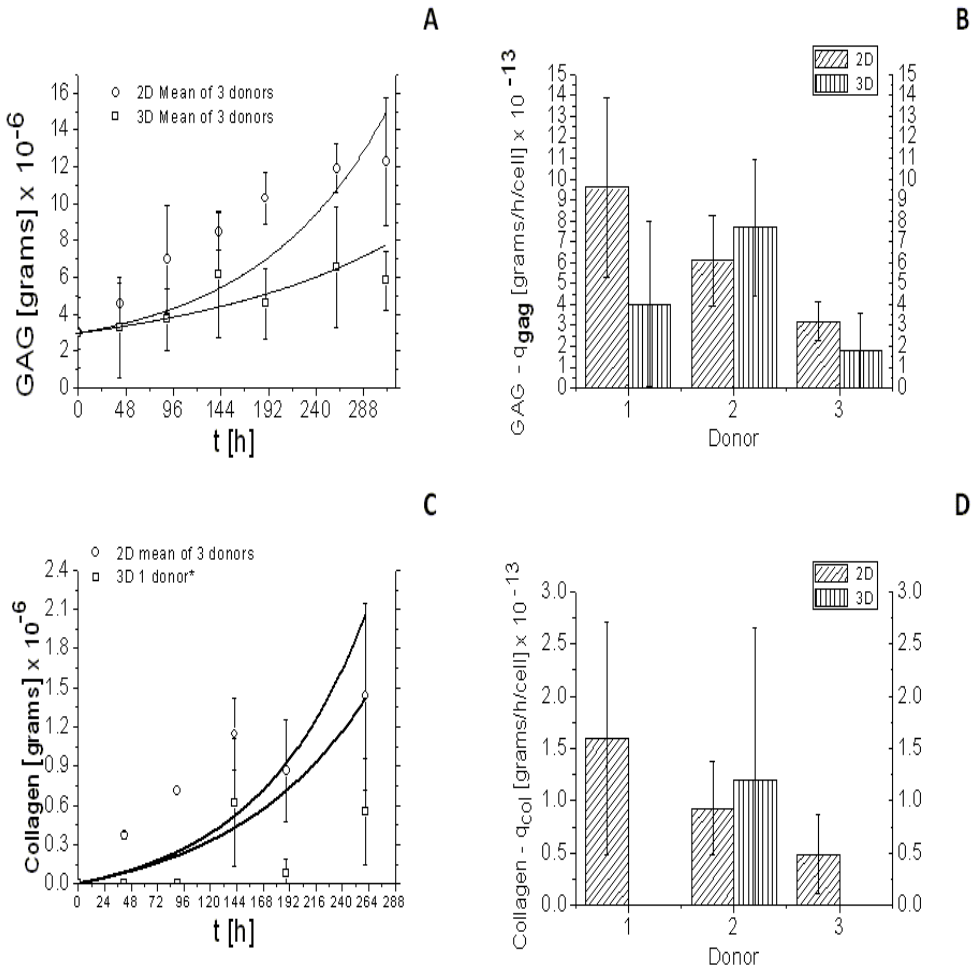


Figure 7 GAG and hydroxyproline or total collagen in time. **A:** GAG on 2D discs (○) and 3D (□) scaffolds. Kinetics model fit of GAG in 2D (—) and 3D (—) cultures. **B:** Box plot with GAG consumption per cell (q_{gag}) of three donors on 2D discs and 3D scaffolds with 95 % confidence interval. **C:** Total collagen on 2D discs (○) and 3D (□) scaffolds. Kinetics model fit of collagen in 2D (—) and 3D (—) cultures. **D:** Box plot with collagen consumption per cell per h (q_{coll}) of three donors on 2D discs and 3D scaffolds with 95 % confidence interval. *2 donors below detection limit.

Molecular concentrations and morphogenesis

All the evidence suggested that chemotaxis (nutrient availability) guided hMSCs into proliferation and migration patterns in 3D scaffolds, but was this morphogenesis? Morphogenesis refers to mechanisms that generate new patterns without generating new cell types [48]. Undetectable total collagen measurements and expression levels of p27 suggested that hMSCs in 3D scaffolds were not differentiat-

ing. On the other hand, GAG measurements indicated that hMSCs in 3D scaffolds could be committing to the cartilage lineage. Histological sections confirmed that hMSCs in the 3D scaffold produced an ECM composed of GAG (Fig. 8A), but not sulphated GAG (Fig. 8B), which is expressed in hMSCs committed to the cartilage lineage. GAG staining also showed that hMSCs migration into the center of the pore produced a loosely associated ECM with nodules of hMSCs and organization into circular patterns. These showed that circular patterns occurred in all axis of the interconnected pore network with an ECM that had similar structural characteristics to those observed during mesenchymal morphogenesis [3]. As a result, these provides evidence to support that morphogenesis guided hMSCs proliferation and migration patterns in 3D scaffolds.

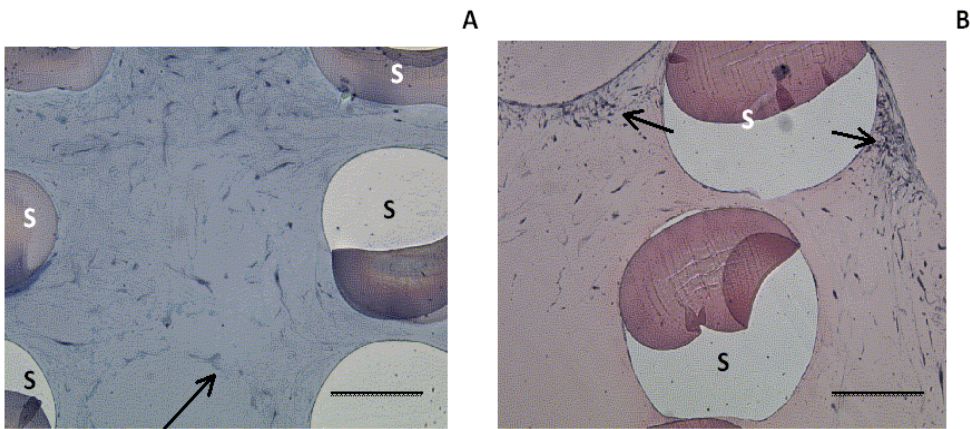


Figure 8 Representative histological section of hMSCs statically cultured in 3D scaffolds (S). GMA embedded. 5 μm sections. **A**: Alcian blue counterstained with haematoxylin. 100 x magnification. Arrow points to hMSCs circular organization pattern. **B**: Safranin-O counterstained with haematoxyline and fast green. Arrows point to nodules with a higher density of hMSCs. 100 x magnification. Scale bar: 100 μm .

The molecular foundations of these morphogenetic patterns can be further elucidated and controlled in microfluidic channels [49, 50]. The morphogenetic nature of nutrient availability can be relevant for understanding how stem cells initiate tissue regeneration and to support the up-scaling of tissues and organ formation.

Conclusions

hMSCs displayed proliferation and migration patterns in 3D scaffolds, which showed a strong correlation to regions of higher nutrient availability. Kinetics, death and cell cycle regulators showed that there was a remarkable adaptability by hMSCs to glucose concentration gradients. Glucosaminoglycans supported ECM organization into circular patterns. In the ECM, sulphated glucosaminoglycans and total col-

lagen did not indicate the differentiation of hMSCs. In conclusion, these evidence supports a morphogenetic effect by nutrients on hMSCs.

References

1. Berg, H.C., *Random walks in biology*. Expanded ed. ed. 1993, Princeton, N.J.: Princeton University Press. 152 p.
2. Bird, R.B., W.E. Stewart, and E.N. Lightfoot, *Transport phenomena*. 2nd rev. ed. ed. 2007, New York ; Chichester: J. Wiley. xii, 905 p.
3. Forgács, G. and S. Newman, *Biological physics of the developing embryo*. 2005, Cambridge: Cambridge University Press. vi, 337 p.
4. Wolpert, L., *Positional information and the spatial pattern of cellular differentiation*. *J Theor Biol*, 1969. **25**(1): p. 1-47.
5. Carrier, R.L., et al., *Effects of oxygen on engineered cardiac tissue*. *Biotechnol. Bioeng.*, 2002. **78**(6): p. 617-25.
6. Freytes, D.O., L.Q. Wan, and G. Vunjak-Novakovic, *Geometry and force control of cell function*. *J Cell Biochem*, 2009. **108**(5): p. 1047-58.
7. Malda, J., T.J. Klein, and S. Upton, *The roles of hypoxia in the in vitro engineering of tissues*. *Tissue Eng.*, 2007. **9**: p. 2153-62.
8. Radisic, M., et al., *Oxygen gradients correlate with cell density and cell viability in engineered cardiac tissue*. *Biotechnol. Bioeng.*, 2006. **2**: p. 332-43.
9. Wang, X., et al., *Growth factor gradients via microsphere delivery in biopolymer scaffolds for osteochondral tissue engineering*. *J Control Release.*, 2009. **134**(2): p. 81-90.
10. Zhou, S., Z. Cui, and J.P. Urban, *Nutrient gradients in engineered cartilage: metabolic kinetics measurement and mass transfer modeling*. *Biotechnol Bioeng*, 2008. **101**(2): p. 408-21.
11. Green, J., *Morphogen gradients, positional information, and Xenopus: Interplay of theory and experiment*. *Developmental Dynamics*, 2002. **225**(392 - 408).
12. Turing, A., *The chemical basis of morphogenesis*. *Philosophical Transactions of the Royal Society of London Series B-Biological Sciences*, 1952. **237**(641): p. 37-72.
13. McBeath, R., et al., *Cell shape, cytoskeletal tension, and RhoA regulate stem cell lineage commitment*. *Developmental Cell*, 2004. **6**(4): p. 483-495.
14. Angele, P., et al., *Cyclic, mechanical compression enhances chondrogenesis of mesenchymal progenitor cells in tissue engineering scaffolds*. *Biorheology*, 2004. **41**(3-4): p. 335-346.
15. Terraciano, V., et al., *Differential response of adult and embryonic mesenchymal progenitor cells to mechanical compression in hydrogels*. *Stem Cells*, 2007. **25**(11): p. 2730-8.
16. Ruiz, S. and C. Chen, *Emergence of patterned stem cell differentiation within multicellular structures*. *Stem Cells*, 2008. **26**(11): p. 2921-7.
17. Grayson, W.L., et al., *Effects of hypoxia on human mesenchymal stem cell expansion and plasticity in 3D constructs*. *Journal of Cellular Physiology*, 2006. **207**(2): p. 331-339.
18. Markway, B., et al., *Enhanced Chondrogenic Differentiation of Human Bone Marrow-Derived Mesenchymal Stem Cells in Low Oxygen Environment Micropellet Cultures*. *Cell Transplant*, 2009. .
19. Caplan, A. and J. Dennis, *Mesenchymal stem cells as trophic mediators*. *J Cell Biochem*, 2006(98): p. 1076.

20. Moroni, L., J.R. de Wijn, and C.A. van Blitterswijk, *Three-dimensional fiber-deposited PEOT/PBT copolymer scaffolds for tissue engineering: Influence of porosity, molecular network mesh size, and swelling in aqueous media on dynamic mechanical properties*. Journal of Biomedical Materials Research Part A, 2005. **75A**(4): p. 957-965.
21. Landers, R. and R. Mulhaupt, *Desktop manufacturing of complex objects, prototypes and biomedical scaffolds by means of computer-assisted design combined with computer-guided 3D plotting of polymers and reactive oligomers*. Macromolecular Materials and Engineering, 2000. **282**(9): p. 17-21.
22. Moroni, L., J.R. de Wijn, and C.A. van Blitterswijk, *3D fiber-deposited scaffolds for tissue engineering: Influence of pores geometry and architecture on dynamic mechanical properties*. Biomaterials, 2006. **27**(7): p. 974-985.
23. Jansen, J., et al., *Fumaric Acid Monoethyl Ester-Functionalized Poly(D,L-lactide)/N-vinyl-2-pyrrolidone Resins for the Preparation of Tissue Engineering Scaffolds by Stereolithography*. Biomacromolecules, 2009. **10**(2): p. 214-220.
24. Hildebrand, T. and P. Ruegsegger, *A new method for the model-independent assessment of thickness in three-dimensional images*. Journal of Microscopy-Oxford, 1997. **185**: p. 67-75.
25. Both, S.K., et al., *A Rapid and Efficient Method for Expansion of Human Mesenchymal Stem Cells* Tissue Engineering, 2007. **13**(1): p. 3 - 9.
26. Wendt, D., et al., *Uniform tissues engineered by seeding and culturing cells in 3D scaffolds under perfusion at defined oxygen tensions*. Biorheology, 2006. **43**: p. 481 - 488.
27. Saltzman, W., *Tissue engineering: principles for the design of replacement organs and tissues*. 1st ed. 2004: Oxford University Press.
28. Sidoli, F.R., A. Mantalaris, and S.P. Asprey, *Modelling of Mammalian Cells and Cell Culture Processes*. Cytotechnology, 2004(44): p. 27 - 46.
29. Kontoravdi, C., et al., *Modeling Amino Acid Metabolism in Mammalian Cells Toward the Development of a Model Library*. Biotechnol. Prog., 2007. **23**(6): p. 1261 - 9.
30. Mohler, L., A. Bock, and U. Reichl, *Segregated Mathematical Model for Growth of Anchorage-dependant MDCK Cells in Microcarrier Culture* Biotechnol. Prog., 2008. **24**(1): p. 110-119.
31. Frame, K.K. and W.S. Hu, *A Model for Density-Dependent Growth of Anchorage-Dependent Mammalian-Cells*. Biotechnology and Bioengineering, 1988. **32**(8): p. 1061-1066.
32. Alberts, B., et al., *Molecular Biology of the Cell*. 5th ed. 2008, New York: Garland Science. 1268.
33. Higuera, G., et al., *Quantifying In Vitro Growth and Metabolism Kinetics of Human Mesenchymal Stem Cells Using a Mathematical Model*. Tissue Engineering Part A, 2009. **15**(9): p. 2653-2663.
34. Lemon, G., et al., *Mathematical modelling of human mesenchymal stem cell proliferation and differentiation inside artificial porous scaffolds*. Journal of Theoretical Biology, 2007. **249**(3): p. 543-553.
35. Zhao, F., et al., *Effects of oxygen transport on 3-D human mesenchymal stem cell metabolic activity in perfusion and static cultures: Experiments and mathematical model*. Biotechnology Progress, 2005. **21**(4): p. 1269-1280.

36. Nelson, C.M., et al., *Emergent patterns of growth controlled by multicellular form and mechanics*. Proceedings of the National Academy of Sciences of the United States of America, 2005. **102**(33): p. 11594-11599.
37. Thompson, D.A.W. and J.T. Bonner, *On growth and form*. an abridged edition. / edited by John Tyler Bonner. ed. 1971, [S.l.]: Cambridge University Press.
38. Sekiya, I., et al., *Expansion of Human Adult Stem Cells from Bone Marrow Stroma: Conditions that Maximize the Yields of Early Progenitors and Evaluate their Quality*. Stem Cells, 2002. **20**: p. 530 - 541.
39. Schop, D., et al., *Growth, Metabolism and Growth Inhibitors of Mesenchymal Stem Cells*. Tissue Engineering: Part A, 2009. **15**.
40. Egozi, D., et al., *Regulation of the cell cycle inhibitor p27 and its ubiquitin ligase Skp2 in differentiation of human embryonic stem cells*. Faseb Journal, 2007. **21**(11): p. 2807-2817.
41. Pelayo, R., et al., *Cell cycle quiescence of early lymphoid progenitors in adult bone marrow*. Stem Cells, 2006. **24**(12): p. 2703-2713.
42. Stehr, W., et al., *Opposing roles for p21(waf1/cip1) and p27(kip1) in enterocyte differentiation, proliferation, and migration*. Surgery, 2005. **138**(2): p. 187-194.
43. Walkley, C.R., et al., *Negative cell-cycle regulators cooperatively control self-renewal and differentiation of haematopoietic stem cells*. Nature Cell Biology, 2005. **7**(2): p. 172-U90.
44. Hawke, T.J., et al., *p21 is essential for normal myogenic progenitor cell function in regenerating skeletal muscle*. American Journal of Physiology-Cell Physiology, 2003. **285**(5): p. C1019-C1027.
45. Zhao, F., R. Chella, and T. Ma, *Effects of shear stress on 3-D human mesenchymal stem cell construct development in a perfusion bioreactor system: Experiments and hydrodynamic modeling*. Biotechnol Bioeng, 2007. **96**(3): p. 584-95.
46. Forgacs, G., et al., *Assembly of collagen matrices as a phase transition revealed by structural and rheologic studies*. Biophysical Journal, 2003. **84**(2): p. 1272-1280.
47. Newman, S., et al., *Viscosity and elasticity during collagen assembly in vitro: Relevance to matrix-driven translocation*. Biopolymers, 1997. **41**(3): p. 337-347.
48. Salazar-Ciudad, I., J. Jernvall, and S.A. Newman, *Mechanisms of pattern formation in development and evolution*. Development, 2003. **130**(10): p. 2027-2037.
49. Nie, F.Q., et al., *On-chip cell migration assay using microfluidic channels*. Biomaterials, 2007. **28**(27): p. 4017-4022.
50. Choi, N.W., et al., *Microfluidic scaffolds for tissue engineering*. Nat Mater, 2007. **6**(11): p. 908-15.



III

From Kinetics to Application

Chapter 5

High-throughput in 3D: Cell and tissue screening *in vitro* and *in vivo*

Gustavo A. Higuera, Joost van Dalum, Ling Wu, Liliana Moreira-Teixeira, Jeroen Leijten, Marcel Karperien, Lorenzo Moroni, and Clemens A. van Blitterswijk.

Department of Tissue Regeneration, Institute for Biomedical Technology, University of Twente, Enschede, The Netherlands.

Abstract

We report the development of the first highthroughput screening (HTS) system that can be used *in vitro* and *in vivo*. Free form fabrication was used to design a 3D well macroarray system. This means that materials already used with this fabrication method can be controlled to produce HTS systems. The implantability of the HTS system depends on the biocompatibility of the material. Hundreds to thousands of these wells of μm^3 to mm^3 size can be organized in a matrix array (macroarray). We used hMSCs to test the HTS design *in vitro*. Well dimensions, cell numbers and culture time were critical parameters that determined 3D hMSCs organization in the wells. The size of each macroarray can be adjusted to fit the implantation site of the test animal. We subcutaneously implanted 3×3 macroarray wells in nude mice and screened three cell types and a coculture. Tissue formation in a well was screened for 6,000, 12,000 and 25,000 cell numbers/well for hMSCs, chondrogenic differentiated hMSCs and primary chondrocytes. In addition, a coculture of hMSCs:primary chondrocytes at 100:0, 50:50, 0:100 were screened. *In vivo* HTS can significantly reduce the number of animals used in drug, toxicity, chemical and tissue screening.

Introduction

Every year, millions of animals are used to evaluate the impact of substances, materials and treatments on the environment and human health. Despite the ethical concerns and financial costs, vertebrate animals will continue to be used. In Europe alone, government policy [1] has mandated the testing of existing substances requiring 54 million vertebrate animals at a projected cost of at least € 9.5 billion over 10 years [2]. One alternative to reduce the number of lives and costs in animal testing involves highthroughput screening (HTS) [3, 4] of *in vitro* models [5, 6]. Despite promising three-dimensional and microfabricated systems [7-14] that mimic the cellular environment and novel drug screening methods [15], the benefit

of high-throughput to predict effects *in vivo* has not been definitely proven [3, 16]. One reason for that is the lack of control and understanding of the variables present in 3D culture [17, 18]. Another reason involves the difficulties to always translate *in vitro* results into *in vivo* settings and the unpredictability of results *in vivo* depending on the species and the analysis methods employed. Remarkably, novel methods to screen polymer blends *in vitro* [19] and *in vivo* [20] have increased the efficiency and predictability of toxicity with animals. In this paper, we explored another alternative to reduce the number of lives and costs in animal testing. This approach involves the development of implantable HTS systems.

The development of the HTS system consists of μm^3 to mm^3 size wells organized in a matrix array (well macroarray). The well macroarrays, made via free-form fabrication, are flexible with respect to the design, well dimensions and biomaterials used (Fig. 1). Human mesenchymal stem cells (hMSCs) were cultured in the macroarrays to evaluate the suitability of the well design *in vitro*. hMSCs were used because these have been shown to be an ideal cell source for various potential medical treatments [21]. To test the highthroughput system *in vivo*, three cell types were seeded in macroarrays at different dilutions per well. In addition, a coculture was seeded in a macroarray at different ratios per well. Then, four conditions (three cell types and a coculture) and 12 subconditions (cell dilutions or coculture ratio) were subcutaneously implanted in nude mice. After explantation, the tissue in each well were screened for host responses and tissue presence in a well.

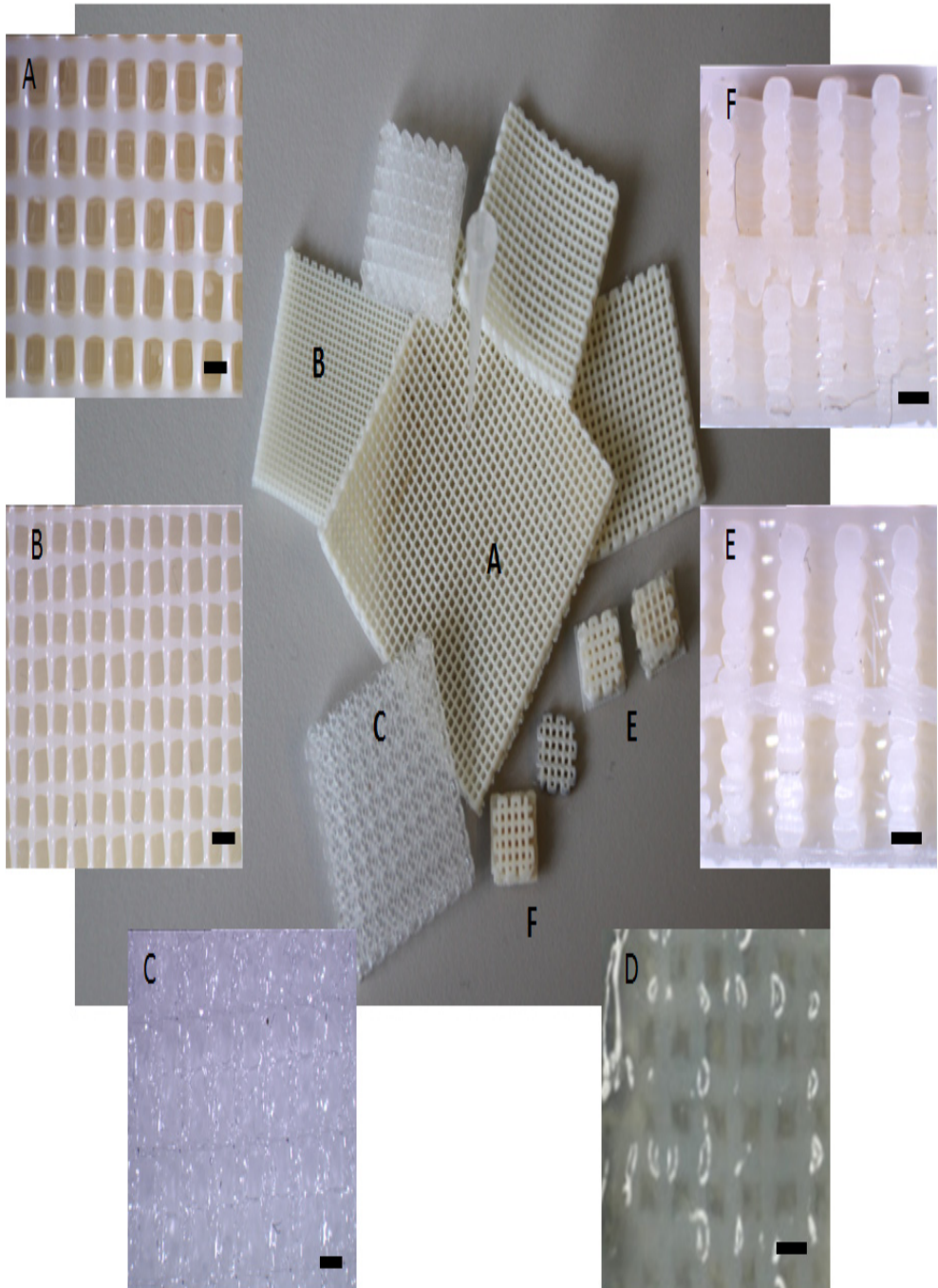


Figure 1 Microarray wells can be made of different materials and with different architectures. White arrow points to pipette tip size that fits into a well. **A:** Top view of 1024 wells in a 32×32 array made of PEOT/PBT of 300/55/45 composition. **B:** Top view of 100 wells in a 10×10 array made of PEOT/PBT of 1000/70/30 composition. **C:** Top view of 100 wells in

a 10×10 array made of poly lactic acid. **D**: Top view of 100 wells in a 10×10 array made of alginate (in PBS). **E**: Cross section of a double array with polymer layer in between and opened bottom and top sides made of 300/55/45 composition of PEOT/PBT. **F**: Cross section of wells made of PEOT/PBT 300/55/45 with a porous layer in the middle. Closed bottom layer and an opened top. Scale bar: 1 mm.

Materials and methods

Well macroarray fabrication

A Bioplotter device (Envisiontec GmbH, Germany), which is a XYZ plotter [22], was used to make the well macroarrays. In this study, most of the macroarray fabrication process is similar to that used for scaffold fabrication [23] (Fig. 2A). 3D cubical models were CAD-designed with Rhinoceros software (Delft, The Netherlands) and loaded on the Bioplotter CAM software (PrimCAM, Einsiedeln, Switzerland). In addition, materials were loaded in a steel syringe for thermoplastic polymers or plastic syringe for hydrogels. Then, the syringe-cartridge unit was mounted on the mobile X-arm of the apparatus. A nitrogen variable pressure between 0.4 Bar and 4 Bar was applied to the syringe for material extrusion. Pressure varied depending on the biomaterial deposited. The combination of software and physical set-up resulted in the extrusion of materials in the form of fibers deposited layer-by-layer onto a stage. The starting fiber deposition speed varied from 320 mm/min and 1800 mm/min depending on the biomaterial composition.

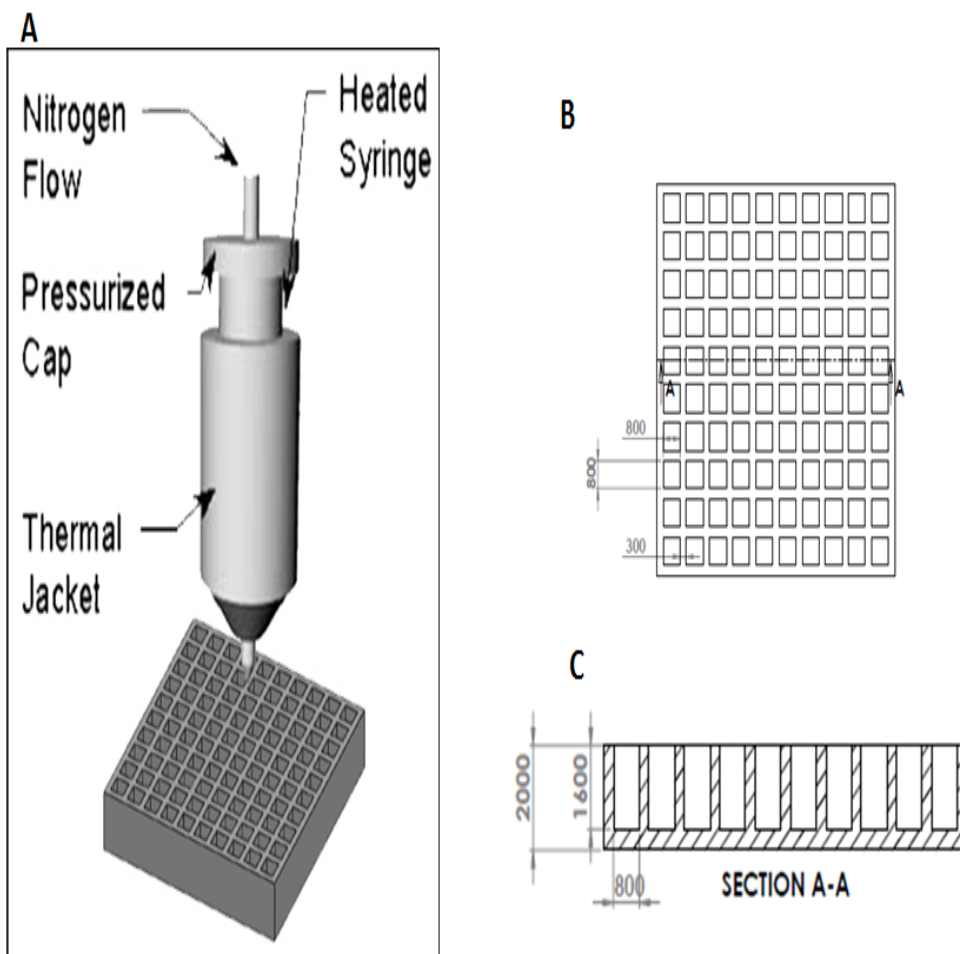


Figure 2 Macroarray well fabrication. **A:** Free form fabrication with 3D-plotters. Material extrusion occurred either by nitrogen pressure. **B:** Top view of a wells in a matrix array (10 columns x 10 rows) **C:** cross section view of the wells where the well is rectangular, with closed bottom and sides, and opened top .

To obtain macroarrays in a matrix form (columns \times rows), closed wells were made by depositing fibers on top of each other at a 90° angle to obtain rectangular wells (Fig. 2B). The well XY dimensions were defined by increasing or decreasing fiber distances in the XY axis. In addition, the well height was defined by the height of the cubical model (Fig. 2C), where the first layer deposited was always closed. Macro-wells were made with four materials with their respective parameters as shown on Table 1.

Table 1 Materials used to make macro-arrays and processing parameters.

Material	Cartridge Temperature [°C]	1 st layer Strand Distance [mm]	2 nd layer and higher strand distance [mm]	Layer thickness [mm]	Inner Needle diameter [mm]
PEOT/PBT 300/55/45	200	0.3	1.5	0.2	0.4
PEOT/PBT 1000/70/30	190	0.3	1.5	0.2	0.25
Polylactic acid	220	0.3	1.5	0.2	0.4
Alginate	25	0.5	3	0.2	0.25

Furthermore, different architecture designs were fabricated to maximize the number of macroarray wells and to create co-culture macroarray systems as shown on figures 1E-F. For these macroarrays of 4 mm in height, the same processing parameters as shown on table 1 were implemented depending on the material. For design on figure 1E, a third layer strand distance (0.5 mm) in the middle of the well macroarray height (at 2 mm) was introduced. For this design, first and second layer strand distances were maintained elsewhere as shown on table 1. Furthermore, the design on figure 1F involved first depositing second layer strand distances (Table 1) to maintain an opened bottom. Then, depositing the first layer strand distance (Table 1) in the middle of the well macroarray height (at 2 mm). Subsequently, layer deposition with second layer strand distances (Table 1) was resumed.

Two-dimensional PEOT/PBT discs

2D substrates of 300PEOT55PBT45 were fabricated by a hot-embossed compression molding technique. Two silicon wafers served as support and defined the molded surface. A stainless steel mold with circular features through holes of 2.2 cm in diameter was placed in between the molds. Granules of 300PEOT55PBT45 were placed inside the mold to fill up the mold cavities upon polymer melting.

Silicon supports were cleaned by immersion in piranha solution (3:1 concentrated H_2SO_4 / 33% aqueous H_2O_2) for 15 min. These were rinsed with water and dried in N_2 . Then, they were functionalized with 1H,1H,2H,2H-perfluorodecyltrichlorosilane (ABCR). After, these were deposited in gas phase that served as anti-adhesion layer to ease the polymer-support separation. For the hot embossing processing, a hydraulic press equipped with a water cooling system and temperature control (Fontune Holland, the Netherlands) was used. The 300PEOT55PBT45 was placed on top of the silicon support and in the aperture of the mold. Then, the system was heated up to a temperature of 180 °C and 10 bars were applied. After 5 minutes the system cooled down to 60 °C and the pressure was released. The mold and the supports were manu-

ally separated and the 2D disc released from the mold.

hMSCs culture

hMSCs were isolated, cultured and cryopreserved as described by Both *et al.*, (2007) [24]. hMSCs were obtained from the acetabulum of three donors who were undergoing total hip replacement surgery and gave informed consent for bone marrow biopsy, approved by the local medical ethical committee. Gender and donor age were: Donor 1: Female, 81 years. Donor 2: Male, 65 years. Donor 3: Female, 66 years. Mono-nucleated cells were counted in the aspirate and plated at a density of 500,000 cells/cm² on tissue culture plastic (Nunc, Thermo Fischer Scientific, Roskilde, Denmark).

Cells were cultured for four to five days in α -minimal essential medium (α MEM) proliferation medium in an incubator with a humidified atmosphere of 5% carbon dioxide at 37 °C. The α MEM proliferation medium contained minimal essential medium (GIBCO, Carlsbad, CA); 10 % fetal bovine serum of a selected batch (FBS; Biowhittaker, lot:8SB0002; Loza, Verviers, Belgium); 0.2mM l-ascorbic-acid-2-phosphate (Sigma, St. Louis, MO); penicillin G (100 Units/ml, Invitrogen, Carlsbad, CA); streptomycin (100 μ g/ml, Invitrogen); 2mM l-glutamine (Sigma) and 1ng/ml basic fibroblast growth factor (Instruchemie, Delfzijl, The Netherlands).

After the four to five day culture period, non-adherent cells and α MEM proliferation medium were discarded. Adherent cells were thoroughly washed twice with PBS phosphate-buffered-saline (PBS, Sigma) and α MEM proliferation medium was refreshed. Adherent cells were proliferated for two passages and cryopreserved. For well macroarray culture, cryopreserved hMSCs - passage 2 - were recounted and plated at 1,000 cells/cm² on tissue culture plastic (Nunc) in α MEM proliferation media. hMSCs were expanded for one week with one refreshment of α MEM proliferation media.

Chondrocyte culture

Primary chondrocytes were isolated through collagenase digestion from articular cartilage harvested from an 18-month old bovine knee joint. Cells were aggregated with 300 μ g/ml of fibronectin (Invitrogen). Primary chondrocytes were expanded for one passage with medium refreshments twice a week. The chondrocyte culture medium contained HEPES (Invitrogen)-buffered DMEM (Invitrogen) supplemented with 10% fetal bovine serum (FBS; Biowhittaker, lot:8SB0002; Loza, Verviers, Belgium), 100 μ g/ml streptomycin (Invitrogen), 0.1 mM nonessential amino acids (Sigma-Aldrich), 0.2 mM ascorbic acid 2-phosphate (Invitrogen), 0.4 mM proline (Sigma-Aldrich) and 100 units/ml penicillin (Invitrogen).

Macroarray sterilization and conditioning for cell culture

Macroarrays were sterilized with 70% Ethanol solution for 15 min. After, macroarrays were washed and incubated at room temperature for two hours with sterile PBS. We repeated this washing step three times. Then, macroarrays were incubated in α MEM proliferation media overnight at 37°C before seeding.

Well macroarray seeding

From a cell suspension of 5×10^6 cells/ml, hMSCs and chondrocytes were centrifuged at 200 Relative Centrifugal Force (RCF) and re-suspended in 0.2 ml of medium. From this cell suspension, dilutions and the coculture were prepared with a maximum of 2.5×10^4 cells in 1 μ l volume seeded per well. Every subcondition (i.e. cell dilutions and coculture ratios), was seeded in all the wells of a column. For example, in a 3 \times 3 macroarray, three replicates or three wells were seeded with the same sub-condition. Seeded well macroarrays were incubated for 20 min at 37°C in a humid atmosphere with 5% CO₂. Non-detached cells in a macroarray were removed by washing with culture medium, then these were placed in a well of a 25-well plate (Nunc), and covered with the culture medium of the seeded cell type and incubated at 37°C.

Coculture

hMSCs:Chondrocytes were seeded in well macroarrays in α MEM proliferation media. Three Chondrocytes:hMSCs ratios (1:0, 0.5:0.5, and 0:1) were seeded in triplicates of three wells of a 3 \times 3 macroarray. 2.5×10^4 were the maximum number of cells seeded in a well with ratios obtained prior to well macroarray seeding.

Chondrogenic differentiation

Macroarrays with hMSCs dilutions were cultured for 4 weeks in chondrogenic differentiation medium. Chondrogenic differentiation medium was composed of DMEM (GIBCO) with the following supplements: 0.01 μ g/ml TGF β 1 (RnD Systems, UK), 0.1nM Dex, 100 μ g/ml sodium pyruvate (Sigma), 40 μ g/ml L-proline (Sigma), 100 μ g/ml streptomycin, 1 \times insulin-transferrin-selenite (ITS+ (Sigma), and 100 U/ml of penicillin. Medium refreshment occurred twice a week.

Immunohistochemistry

Click-iT® EdU Alexa Fluor® 488 Imaging Kit (Invitrogen) was used to image the DNA synthesis by proliferating hMSCs in well macroarrays. Wells with hMSCs were incubated in a 1:1 solution of EDU in proliferation medium at 37 °C for 24 h. Then, these were fixed in 1% formalin (Sigma-Aldrich) for 30 min. 3D scaffolds

were embedded in Tissue-Tek OCT (Qiagen, The Netherlands) and placed at -80°C overnight. $5\ \mu\text{m}$ sections were then cut in a cryomicrotome. After, sections on a slide were permeabilized and washed with the secondary antibody (horseradish peroxidase conjugated goat-anti-human immunoglobulin antibody, Dako, Denmark) and counterstained with DAPI (Invitrogen). Fluorescent microscopy was used to visualize EdU (DNA) and DAPI (cell nuclei) signals.

Implantation in nude mice

Nude mice studies were performed after consent from the ethical committee for animal studies (DEC-GDL Utrecht, The Netherlands). Six-week-old nude mice (Hdcpb:NMRI-nu Harlan, The Netherlands) were anaesthetized with 0.02 ml of a 3.5:3:1 mixture of ketamine (100 $\mu\text{g}/\text{ml}$): Xylazine (20 $\mu\text{g}/\text{ml}$): atropine (0.5 $\mu\text{g}/\text{ml}$). Four 3×3 macroarray wells containing each of the conditions and sub-conditions were subcutaneously implanted per mouse in the posterior-lateral side of the back and sutured. The four conditions implanted were: hMSCs, differentiated hMSCs, chondrocytes, and hMSCs:chondrocytes coculture. The 3 sub-conditions tested for each condition within each macroarray are referenced on Table 2. After 2 weeks ($n = 10$) and 4 weeks ($n=10$) mice were euthanized via CO_2 asphyxiation and macroarrays were excised and processed for analysis.

Table 2 Subconditions screened in the well macroarrays subcutaneously implanted in nude mice.

Number	Sub-condition	Number	Sub-condition
1	hMSCs 4X, wk 2	13	BPCs 4X, wk 2
2	hMSCs 2X, wk 2	14	BPCs 2X, wk 2
3	hMSCs 1X, wk 2	15	BPCs 1X, wk 2
4	hMSCs 4X, wk 4	16	BPCs 4X, wk 4
5	hMSCs 2X, wk 4	17	BPCs 2X, wk 4
6	hMSCs 1X, wk 4	18	BPCs 1X, wk 4
7	Diff. hMSCs 4X, wk 2	19	hMSCs:BPCs 0:1, wk 2
8	Diff. hMSCs 2X, wk 2	20	hMSCs:BPCs 0.5:0.5, wk 2
9	Diff. hMSCs 1X, wk 2	21	hMSCs:BPCs 0:1, wk 4
10	Diff. hMSCs 4X, wk 4	22	hMSCs:BPCs, 0.5:0.5, wk 4
11	Diff. hMSCs 2X, wk 4	23	hMSCs:BPCs, 1:0, wk 4
12	Diff. hMSCs 1X, wk 4	24*	hMSCs:BPCs, 1:0, wk 2

*Quantification was not possible.

Histology

3×3 macroarray wells implanted in nude mice were washed in PBS and fixed in 10 % Formalin at 4°C overnight. After washing in PBS, macroarrays were cut into

rows with a sharp blade and stained with 1% Methylene blue. For hematoxylin/eosin (H&E) staining, after cutting a macroarray row (3 wells) with a sharp blade, samples were dehydrated and embedded in Glycol Methyl Acrylate (GMA). 5 μm sections were cut with a microtome and stained with H&E.

Tissue quantification

A row in the 3 \times 3 macroarray matrix stained with 1 % methylene blue was imaged with a stereomicroscope. Images were processed by cutting the images of wells in a row and converting them to a binary pixel image (Fig. 6E) with ImageJ software (Free source). Black and white pixels within an image of a well were quantified with the histogram function in ImageJ, where the total pixels and tissue pixels were obtained. The tissue/total pixels ratio was obtained for each well in a row of a 3 \times 3 macroarray implanted.

Statistical analysis

Statistical significance was set at $p < 0.05$. 3 \times 3 Macroarray wells were implanted in nude mice ($n = 20$) for explantation on weeks 2 and 4. Linear regression was performed for the means of tissue/total ratio [pixel/pixel] vs. cell number for each sub-condition (Table 2) for $n = 10$ mice per time point. Anova analysis between and within means of tissue/total ratio [pixel/pixel] of all sub-conditions was performed with the *anova1* and *multcompare* functions of Matlab (version 7.0.4 release 2007a; Mathworks, Natick, MA) on a windows-based system.

Results

Free-form fabrication was used to develop the HTS system. This allowed us to define both the well architecture and the number of wells in column \times rows arrays (Fig. 2). Rectangular 90 $^\circ$ -angle wells were seeded with hMSCs and cultured in time. In this manner, it was observed that there was an inverse correlation between hMSCs organization and well size (Fig. 3): As the well size increased (Fig. 3 A- C), hMSCs organized from 3D aggregates to mono-layers, thus showing that hMSCs organization could be controlled through the well volume and culture time.

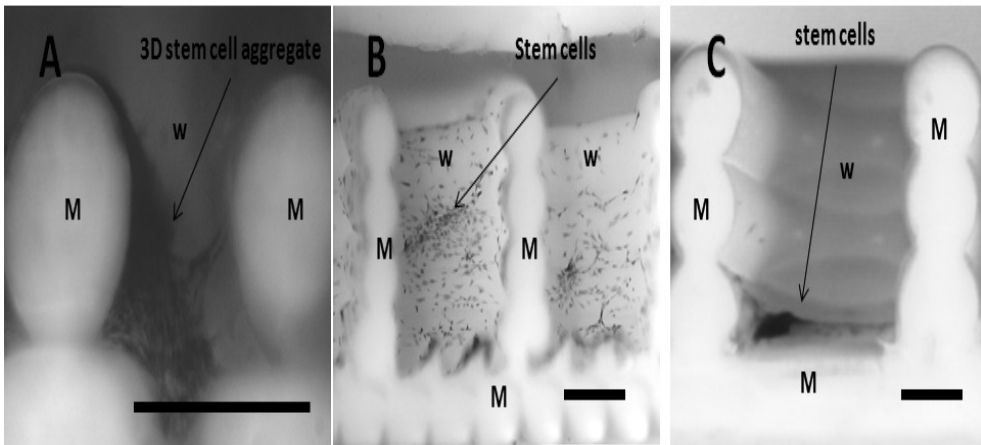


Figure 3 Well dimensions produce a different hMSCs organization level. Cross sections of smallest to biggest well used **A**, **B** and **C**, respectively. All well dimensions were seeded with 12,000 hMSCs and cultured for 2 days. The “m” stands for material, “w” stands for well. Stem cells were stained with methylene blue . Scale bar: 0.5 mm.

In addition, different cell dilutions seeded into different wells illustrated that it was possible to maintain different levels of hMSCs organization in different wells (Fig. 4A) in the same macroarray. The well with the highest number of hMSCs contained 3D aggregates whereas hMSCs dilutions produced wells with monolayer hMSCs cultures. This showed that different conditions could be maintained in different wells in an array style. On the contrary, hMSCs on 2D PEOT/PBT discs did not form 3D aggregates neither in time nor as a function of cell numbers (Fig. 4B).

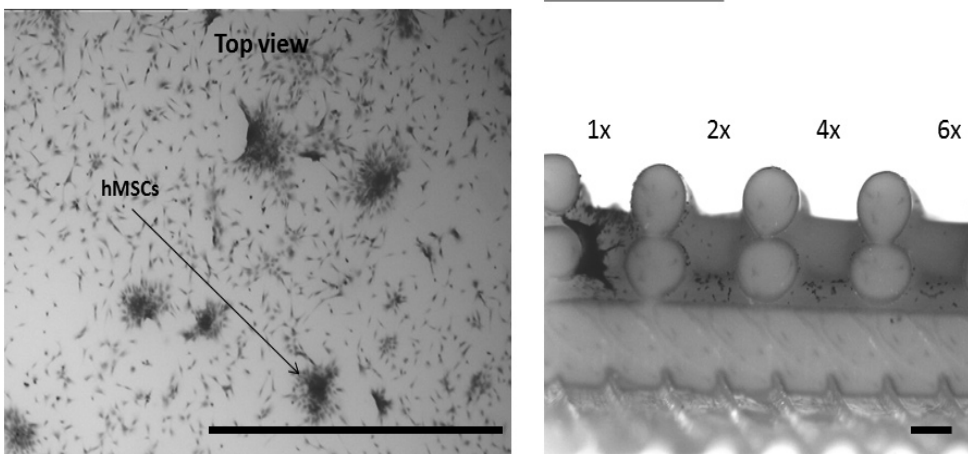


Figure 4 **A**: Cross section of hMSCs dilutions seeded in a row. 1X was equivalent to 25,000 hMSCs. **B**: hMSCs on 2D PEOT/PBT disc. 300,000 hMSCs seeded. Culture time 5 days. hMSCs do not form a 3D construct. Scale bar: 0.5 mm.

The time-dependent nature of hMSCs proliferation was exploited to produce

hMSCs aggregates of different sizes (Fig. 5) in different wells of the same macroarray. As the culture time increased, hMSCs proliferated and formed larger aggregates (Fig. 5).

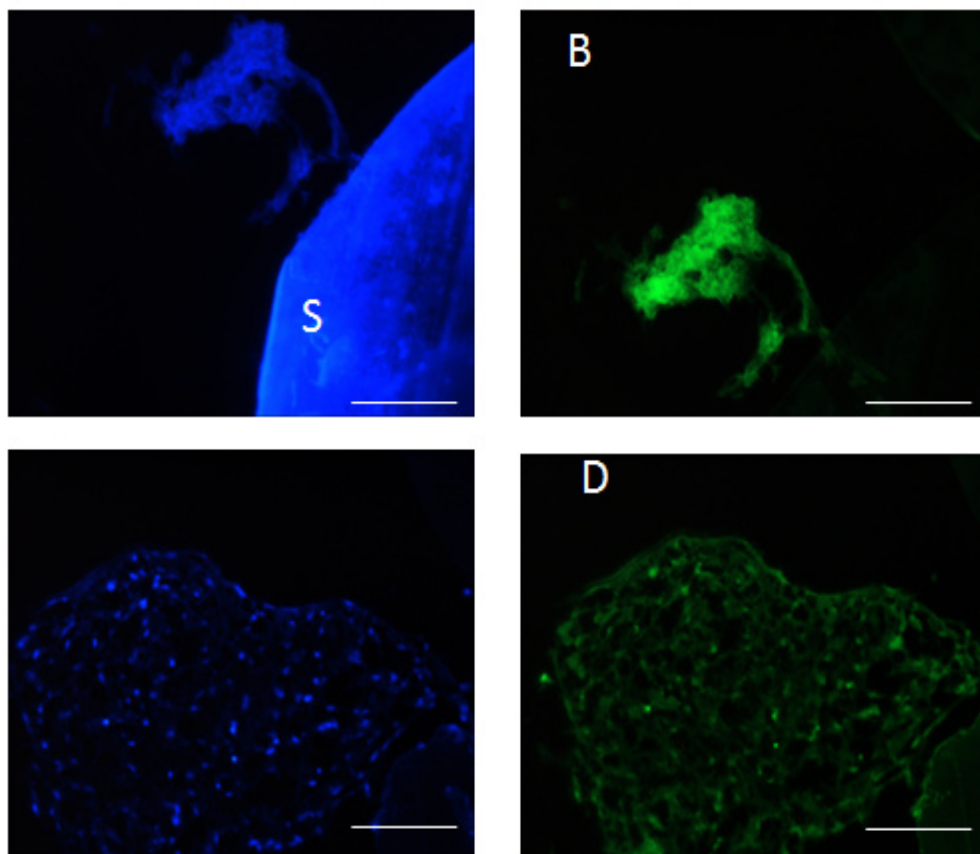


Figure 5 hMSCs proliferation in time produces aggregates of different sizes inside of the wells. 25,000 hMSCs seeded per well. S: Scaffold. **A:** 2 days of culture. Cell nuclei (Dapi) in aggregate. **B:** 2 days of culture. Proliferation marker (EDU) in aggregate. **C:** 5 days of culture. Cell nuclei (Dapi) in aggregate. **D:** 5 days of culture. Proliferation marker (EDU) in aggregate. Scale bar: 100 μ m. Magnification 200 X.

Well macroarrays were tested *in vivo* in 3×3 well macroarrays custom-made to fit in a mouse pocket. Each of the 9 wells within the implanted 3×3 macroarray measured 1 mm \times 1 mm \times 1.8 mm. (Fig. 3B). hMSCs, differentiated hMSCs, primary bovine chondrocytes (PBCs) and a hMSCs:PBCs co-culture, for a total of four conditions were evaluated in each of four mouse pockets (Fig. 6). For each condition, $1\times$, $2\times$ and $4\times$ cell dilutions (Fig. 6) were made for a total of three sub-conditions. Each sub-condition was seeded into each well column to obtain three replicates in each 3×3 well macroarray.

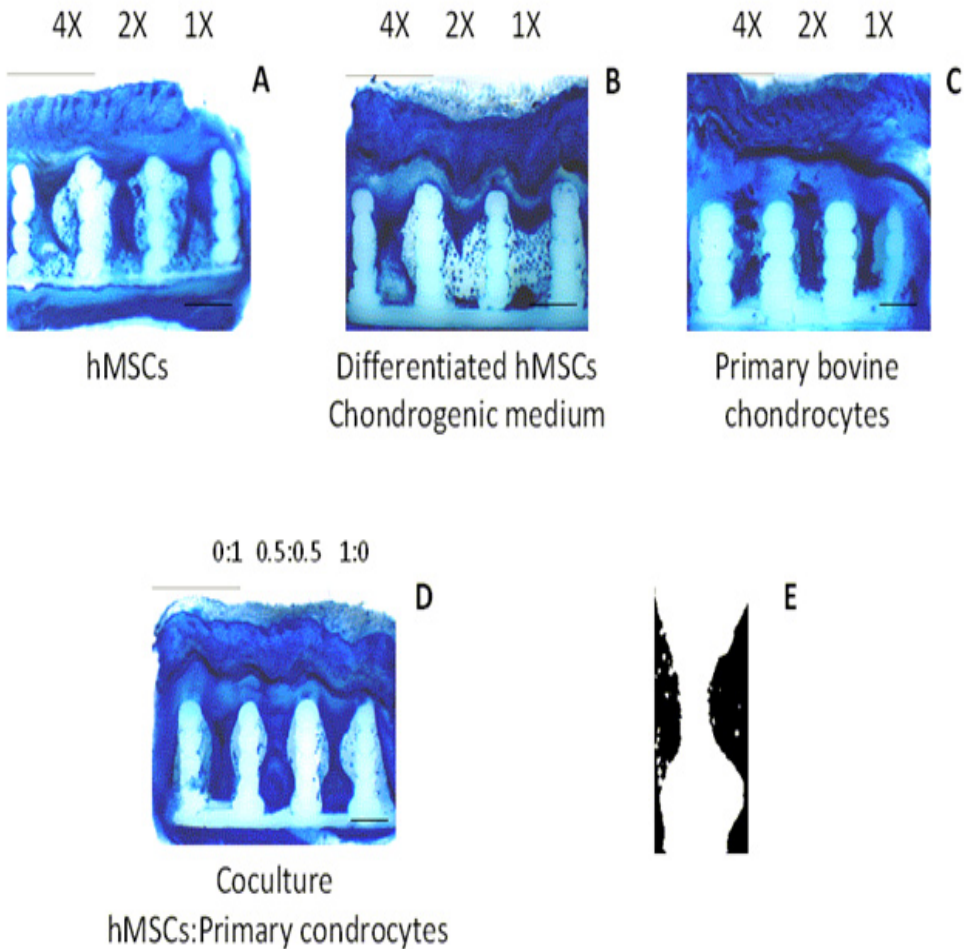


Figure 6 Four conditions seeded in 3×3 macroarray and implanted in mice. 1X was equivalent to 25,000 cells seeded per well. 25,000 cells were the highest number of cells seeded in a well. **A:** hMSCs. **B:** Differentiated hMSCs **C:** PBCs **D:** coculture hMSCs:PBCs in three ratios 0:1, 0.5:0.5, 1:0. **E:** Example of image used for tissue area quantification within each well. The image fits into the area contained in one well using the macrowell material as reference. Scale bar: 1 mm.

Implantations occurred on weeks 2 and 4, with 10 mice sacrificed on each week to evaluate the conditions and sub-conditions implanted in each macroarray. Figure 6 shows tissue (host and implanted) penetration in all sub-conditions. Tissue bulges were present in all wells. Consequently, tissue coverage was quantified. This was done by quantifying the tissue (host and implanted) coverage ratio of tissue pixels over total area pixels (Fig. 6E).

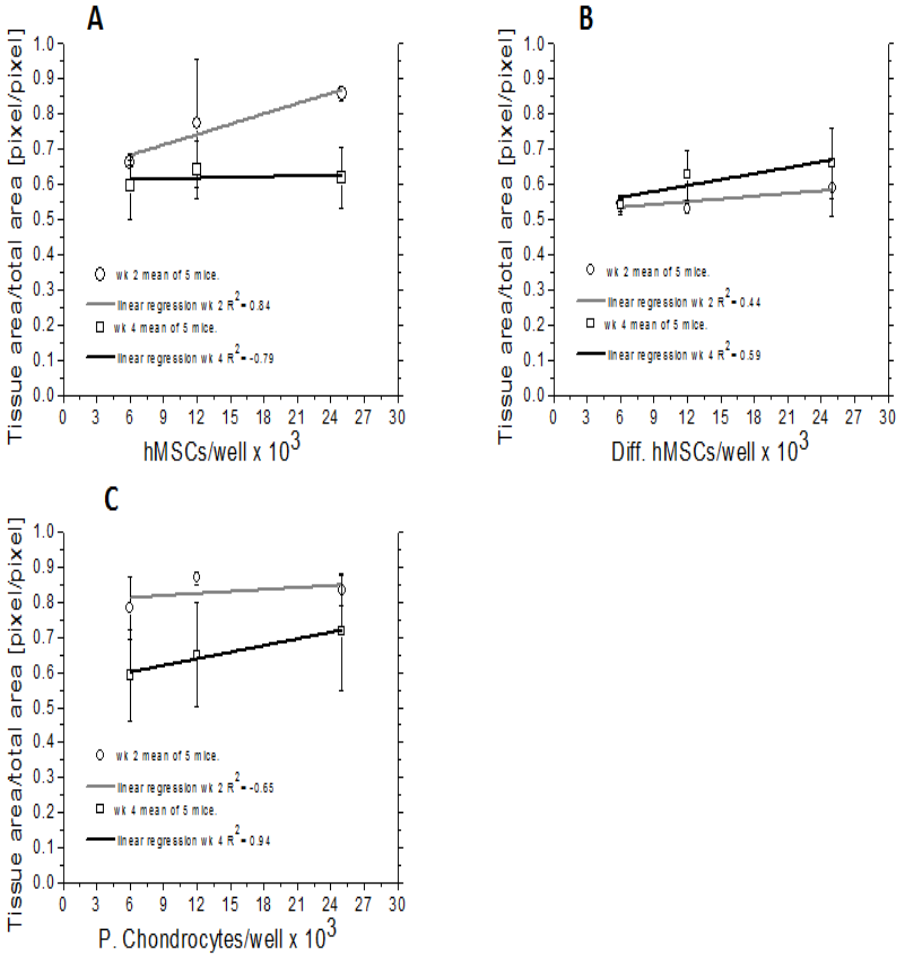


Figure 7 Linear regression analysis of tissue area vs. cell numbers on weeks 2 and 4. **A:** hMSCs **B:** Differentiated hMSCs. **C:** Primary chondrocytes . Statistical significance $p < 0.05$.

Linear regression analysis was performed on the means of tissue area vs. cell numbers for the three cell types implanted in macroarrays (Fig. 7). This analysis showed that there was strong linear correlation for tissue area vs. cell numbers for hMSCs week 2 ($R^2 = 0.84$, Fig. 7A) and for primary chondrocytes week 4 ($R^2=0.94$, Fig. 7C). All other subconditions did not show a strong correlation coefficient.

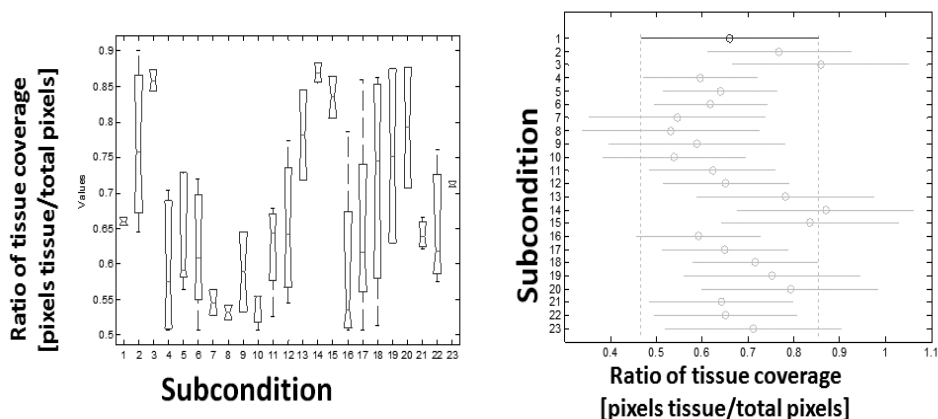


Figure 8 Statistical analysis of tissue area quantification in each well of all sub-conditions implanted. Each sub-condition is represented by a number referenced in table 1. **A**: ANOVA box plot of all sub-conditions. **B**: Multiple comparison test of means of all sub-conditions with each other according to ANOVA statistics and their 95 % confidence interval.

To compare subconditions between each other, ANOVA and multiple comparison analysis of the means were performed (Fig. 8, numbers of subconditions on table 2, ANOVA table on table 3). The box plots (Fig. 8A) of each subcondition showed that there were different subconditions from each other ($p = 0.0058$ on Table 3). But, multiple comparison analysis of each of the means showed that these differences were not significant (Fig. 8B). The ratio of tissue coverage was not significantly different between conditions in any macroarray.

Table 3 ANOVA table comparing means of all sub-conditions

Source	SS	df	MS	F	Prob>F
Sub-conditions	0.53	22	0.024	2.42	0.0058
Error	0.46	46	0.011		
Total	0.99	68			

Representative histological sections of the host tissue above were stained with H&E (Fig. 9). Host tissue above the wells of the hMSCs (Fig. 9A) condition showed lumens of larger size and in higher numbers than on the other three conditions (Fig. 9B-D).

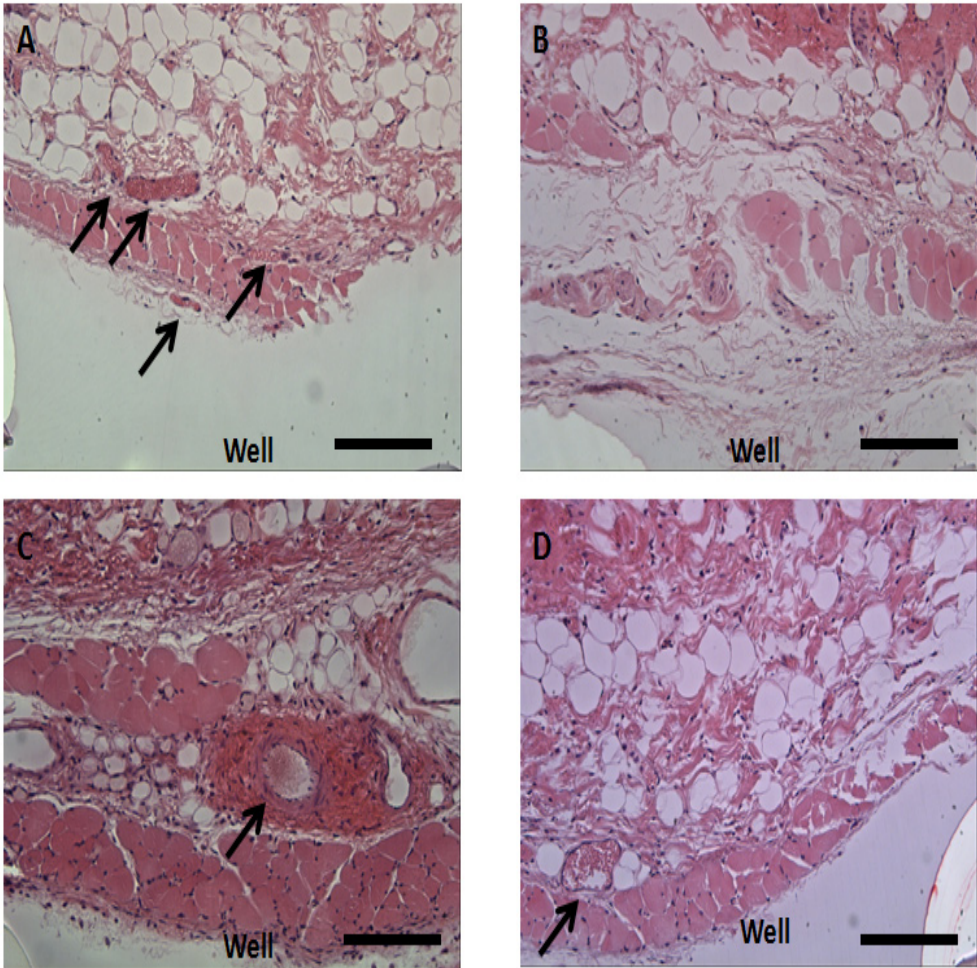


Figure 9 H&E staining of representative sections of host tissue above well macroarrays after 1 month implantation. 100 X magnification. Arrows point to vessel lumens. **A:** hMSCs. **B:** Differentiated hMSCs **C:** Primary Chondrocytes. **D:** Coculture hMSCs:Primary Chondrocytes. Scale bar: 100 μ m.

Discussion

Performing thousands of experiments within a single vertebrate animal offers the extraordinary possibility to screen multiple conditions *in vivo*. First, we explored this possibility *in vitro* by creating 3D well macroarrays of PEOT/PBT and seeding hMSCs in them. hMSCs were used to evaluate the effect of well sizes on hMSCs growth, and organization, and on tissue development. Well dimensions, cell numbers, and culture time were the most important parameters to control tissue culture within the macroarray. Concentrating hMSCs in a well significantly reduced the need

for hMSCs expansion [25]. In addition, with 6,000 - 25,000 hMSCs, 3D hMSCs aggregates of different sizes could be produced by adjusting the culture time. 1.8 mm³ wells were optimal to seed, culture and manually manipulate macroarrays *in vitro* with 25,000 hMSCs or less.

The size of wells developed in this high throughput screening (HTS) system falls between the sizes of microfabricated HTS and culture plate arrays. The size presented here combines two advantages from the standard sizes: (i) less resources are used. For example, low cell numbers are used to seed each well; (ii) manipulation is possible. For instance, the use of standard pipettes is possible. One of the biggest limitations that we faced were the analytical techniques available, the HTS was too large to use microfabricated HTS methods and too small to be analyzed with standard plate array technology. Even though few wells were tested as a proof-of-principle, this HTS system has the potential to house thousands of wells within one macroarray. Without a doubt, the biggest contribution this HTS can offer is to reduce the number of animals used in *in vivo* experiments. This was achieved by processing biocompatible polymers, where well numbers and macroarray size can be adjusted to the implantation site of the test animal.

In *in vivo* HTS development, 3×3 well macroarrays were subcutaneously implanted in mice to screen the effect on tissue formation of having different cell numbers per well in one mouse pocket. Three cell types were tested. In addition, three different ratios of hMSCs:primary chondrocytes coculture were implanted. Trend analysis with linear regression showed that there was a correlation between tissue area ratio vs. cell number for hMSCs at week 2 and for primary chondrocytes at week 4. This indicated that wells with high cell numbers produced wells with a higher tissue coverage ratio. Even though there were trends detected, ANOVA analysis of the tissue coverage ratio did not vary significantly between subconditions. This suggests that sub-conditions tested were not extreme enough to produce a significant difference in tissue coverage of the well with the markers analyzed. Methods that avoid histological processing [20, 26, 27] would be convenient to improve the quantification and sensitivity of *in vivo* HTS. Interestingly, well macroarrays with hMSCs displayed the presence of lumens of larger size and in higher numbers than in other conditions. This could have been a host response to trophic factors secreted by hMSCs [28]. Despite the probability that vessels were already present above the wells, we observed vessels repeatedly in this sub-condition. This supports the proposition of a new strategy for tissue regeneration relying on concentrating hMSCs in strategic locations in a scaffold. By doing this, instructive materials [29] could be designed to deliver trophic factors and induce the regeneration of the host tissue towards the implanted hMSCs.

Without the HTS system here developed, performing tissue screening analysis of the same cell numbers and co-culture ratios would have required 3 times the number of animals as each subcondition would have had to be tested separately. This proof-of-principle study used PEOT/PBT. As shown in Figure 1, many other materials could be also used showing the versatility of our approach. In addition, it is foreseen that novel methods to monitor biomechanics [30] and elucidating gene regulatory networks [31, 32] of tissues and cells could be adapted. This platform drastically reduces vertebrate animal lives and costs in pharmaceutical, toxicological, chemical, and disease screening, while allowing for the first time to perform such screening in true three-dimensional tissues. We anticipate that this technology will contribute to advance our society health conditions.

Conclusions

In vivo HTS reduces the number of animals used in animal experiments. Thousands of wells can be made with a wide range of materials, where the HTS size can be defined for the implantation site of the tested animal. This significantly reduces financial costs and lives of vertebrate animals used in the chemical, biotechnological, pharmaceutical, and biomedical industries among others.

References

1. European-Commission, *Reach: In Brief*, E.D. General, Editor. 2007. p. 19.
2. Hartung, T. and C. Rovida, *Chemical regulators have overreached*. . Nature, 2009. **460**: p. 1080 - 1081.
3. Kunz-Schughart, L.A., et al., *The use of 3-D cultures for high-throughput screening: The multicellular spheroid model*. Journal of Biomolecular Screening, 2004. **9**(4): p. 273-285.
4. Stokstad, E., *Putting chemicals on a path to better risk assessment*. Science, 2009. **325**: p. 694-695.
5. Inch, W., J. McCredie, and R. Sutherland, *Growth of nodular carcinomas in rodents compared with multi-cell spheroids in tissue culture*. Growth, 1970. **34**: p. 271-282.
6. Cheng, K., Y. Lai, and W.S. Kisaalita, *Three-dimensional polymer scaffolds for high throughput cell-based assay systems*. Biomaterials, 2008. **29**: p. 2802 - 2812.
7. Yen, C.M., C.C. Chan, and S.J. Lin, *High-throughput reconstitution of epithelial-mesenchymal interaction in folliculoid microtissues by biomaterial-facilitated self-assembly of dissociated heterotypic adult cells*. Biomaterials, 2010. **31**(15): p. 4341-4352.
8. Gallego-Perez, D., et al., *High throughput assembly of spatially controlled 3D cell clusters on a micro/nanoplatfom*. Lab on a Chip, 2010. **10**(6): p. 775-782.
9. Ibold, Y., et al., *Development of a high-throughput screening assay based on the 3-dimensional pannus model for rheumatoid arthritis*. Journal of Biomolecular Screening, 2007. **12**(7): p. 956-965.
10. Schindler, M., et al., *Living in three dimensions - 3D nanostructured environments for cell culture and regenerative medicine*. Cell Biochemistry and Biophysics, 2006. **45**(2): p. 215-227.
11. Kane, B.J., et al., *Liver-specific functional studies in a microfluidic array of primary mammalian hepatocytes*. Analytical Chemistry, 2006. **78**(13): p. 4291-4298.
12. Khademhosseini, A., et al., *Micromolding of photocrosslinkable hyaluronic acid for cell encapsulation and entrapment*. Journal of Biomedical Materials Research Part A, 2006. **79A**(3): p. 522-532.
13. Yan, Y.N., et al., *Direct construction of a three-dimensional structure with cells and hydrogel*. Journal of Bioactive and Compatible Polymers, 2005. **20**(3): p. 259-269.
14. Albrecht, D.R., et al., *Photo- and electropatterning of hydrogel-encapsulated living cell arrays*. Lab on a Chip, 2005. **5**(1): p. 111-118.
15. Gupta, P.B., et al., *Identification of Selective Inhibitors of Cancer Stem Cells by High-Throughput Screening*. Cell, 2009. **138**(4): p. 645-659.
16. Peters, A., D.M. Brey, and J.A. Burdick, *High-Throughput and Combinatorial Technologies for Tissue Engineering Applications*. Tissue Engineering Part B-Reviews, 2009. **15**(3): p. 225-239.
17. Woodfield, T.B.F., L. Moroni, and J. Malda, *Combinatorial Approaches to Controlling Cell Behaviour and Tissue Formation in 3D via Rapid-Prototyping and Smart Scaffold Design*. Combinatorial Chemistry & High Throughput Screening, 2009. **12**(6): p. 562-579.
18. Wan, H. and A.G. Holmen, *High Throughput Screening of Physicochemical Properties and In Vitro ADME Profiling in Drug Discovery*. Combinatorial Chemistry &

- High Throughput Screening, 2009. **12**(3): p. 315-329.
19. Khan, F., et al., *Strategies for cell manipulation and skeletal tissue engineering using high-throughput polymer blend formulation and microarray techniques*. Biomaterials, 2010. **31**(8): p. 2216-2228.
 20. Bratlie, K.M., et al., *Rapid Biocompatibility Analysis of Materials via In Vivo Fluorescence Imaging of Mouse Models*. Plos One, 2010. **5**(3): p. -.
 21. Caplan, A., *Why are MSCs therapeutic? New data: new insight*. Journal of Pathology, 2009. **217**(2): p. 318-324.
 22. Landers, R. and R. Mulhaupt, *Desktop manufacturing of complex objects, prototypes and biomedical scaffolds by means of computer-assisted design combined with computer-guided 3D plotting of polymers and reactive oligomers*. Macromolecular Materials and Engineering, 2000. **282**(9): p. 17-21.
 23. Moroni, L., J.R. de Wijn, and C.A. van Blitterswijk, *Three-dimensional fiber-deposited PEOT/PBT copolymer scaffolds for tissue engineering: Influence of porosity, molecular network mesh size, and swelling in aqueous media on dynamic mechanical properties*. Journal of Biomedical Materials Research Part A, 2005. **75A**(4): p. 957-965.
 24. Both, S.K., et al., *A Rapid and Efficient Method for Expansion of Human Mesenchymal Stem Cells* Tissue Engineering, 2007. **13**(1): p. 3 - 9.
 25. Aubin, J.E., *Bone stem cells*. Journal of Cellular Biochemistry, 1998: p. 73-82.
 26. Judex, S., et al., *Quantification of adiposity in small rodents using micro-CT*. Methods, 2010. **50**(1): p. 14-19.
 27. Bhargava, R., et al., *High throughput assessment of cells and tissues: Bayesian classification of spectral metrics from infrared vibrational spectroscopic imaging data*. Biochimica Et Biophysica Acta-Biomembranes, 2006. **1758**(7): p. 830-845.
 28. Caplan, A. and J. Dennis, *Mesenchymal stem cells as trophic mediators*. J Cell Biochem, 2006(98): p. 1076.
 29. Karp, J.M. and R. Langer, *Development and therapeutic applications of advanced biomaterials*. Current Opinion in Biotechnology, 2007. **18**(5): p. 454-459.
 30. La, R. and M.F. Arnsdorf, *Multidimensional atomic force microscopy for drug discovery: A versatile tool for defining targets, designing therapeutics and monitoring their efficacy*. Life Sciences, 2010. **86**(15-16): p. 545-562.
 31. Licatalosi, D.D., et al., *HITS-CLIP yields genome-wide insights into brain alternative RNA processing*. Nature, 2008. **456**(7221): p. 464-U22.
 32. Whittington, T., A.C. Perkins, and T.L. Bailey, *High-throughput chromatin information enables accurate tissue-specific prediction of transcription factor binding sites*. Nucleic Acids Research, 2009. **37**(1): p. 14-25.

General Discussion

Mesenchymal stem cells occupy a natural microenvironment rich in physical forces [1]. Despite that, MSCs are programmed to sense and respond to specific physical and biochemical signals for each musculoskeletal tissue [2]. Examples to support this to be true of MSCs can be observed in their mechanotransduction [3-6]. This also indicates that there are kinetic responses specific to the physical and biochemical forces around MSCs. The main thesis of this book proposed that physical phenomena underlies the formation of 3D tissue. Diffusive mass transport and shear stress were studied to determine how these affected hMSCs organization.

The future model

From monolayer (Chapters 1 and 2) into three-dimensions (Chapters 3, 4 and 5), the kinetics referred to the analysis of hMSCs proliferation through the law of conservation of mass. To visualize this, the environment surrounding hMSCs populations in each condition must be taken into account (Fig. 1). The mass balances were determined by reaction rates of molecules entering or leaving a vessel containing any of the attachment surfaces (Fig. 1). This mathematical approach intended to simplify the complexity of hMSCs proliferation [7, 8]. Mathematical models are needed to combine knowledge and hypotheses from multiple disciplines in tissue regeneration into common objectives [9].

Currently, mathematical modelling is at an infant stage in successfully describing tissue processes. To engineer tissue, the extracellular matrix (ECM) is a strategic biological aspect to be considered by mathematical models because of the ECM's mechanical and biological importance [10, 11]. From the perspective of the ECM, it is possible to explore cellular [12] and tissue [2] biology. Thus, theoretical description of the forces present in ECM development and maintenance can stimulate significant progress in 3D tissue regeneration.

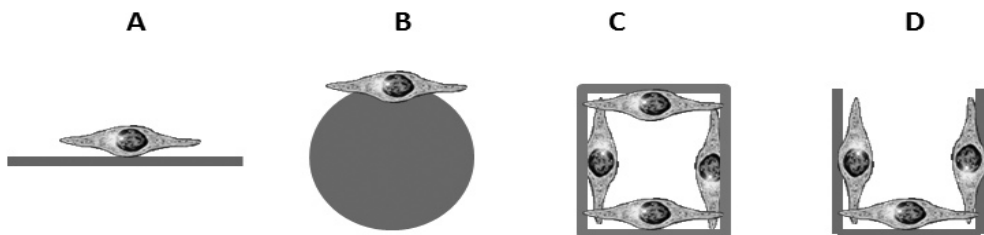


Figure 1 hMSCs depicted on culture conditions investigated in this thesis. Conditions are represented by the cross section of the geometry of the attachment surface. Not a scale representation. **A:** hMSCs attached to tissue culture plastic (Chapter 1, 2) or the PEOT/PBT disc (Chapter 4). **B:** hMSCs attached to the surface of a cytodex microcarrier (Chapter 2). **C:**

hMSCs attached to fibers of a rectangular pore in a 3D scaffold (Chapter 3 and 4). **D**: hMSCs attached to the walls of a 3D well (Chapter 5).

Food produces tissue

When culturing hMSCs in different conditions, one notable aspect involved the organization of hMSCs proliferation. Chapter 1 identified metabolic differences that suggested that competition for substrates [13] controlled hMSCs proliferation. By controlling the diffusive mass transport in 3D culture, competition for substrates was intensified. Thus, chapter 4 and 5 (Fig. 1 C-D) also strongly suggest that competition for substrates regulates hMSCs proliferation. This agreed with previous results showing that nutrient availability correlates with specific growth rates of hMSCs [8]. In addition, hMSCs 3D organization was significantly different in chapters 4 and 5 despite sharing the same material and geometrical dimensions.

On chapter 4, 3D scaffolds had pores measuring 0.4 and 0.8 mm, where hMSCs migrated towards the center of the pore in circular 3D patterns. On chapter 5, well channels measured 0.5, 1 and 1.5 mm in width, where hMSCs migrated upwards, forming 3D hMSCs aggregates. Also, the pore architecture was similar in both culture conditions, but 3D circular patterns were never seen on well channels (Chapter 5). Another notable aspect was that hMSCs 3D organization correlated with the expected concentration gradients that form during culture. As was shown in chapter 4, MSCs on flat surfaces and pores experience gradients with different profiles. These evidence made us propose that hMSCs proliferation and migration occurs in the direction of high molecular concentrations.

Kinetics from Monolayer to 3D

Diffusive mass transport was present in all culture conditions (Fig. 1). Thus hMSCs static culture causes steep concentration gradients (Chapter 4). To be able to determine, concentration-dependent responses, hMSCs proliferation was analyzed through kinetics. Resources availability modulates the cell cycle [13]. Therefore, cell numbers and glucose were considered with parameters (μ and q_g , respectively) estimated in chapters 1, 2 and 4.

Table 1 shows a comparison of these parameters for hMSCs cultures in this thesis and in the literature. It is important to note that many experimental parameters varied between studies have an effect on μ and q_g , such as materials chemistry [14]. The highest μ was estimated for cultures on tissue culture plastic (TCP) ([15], chapter 1 and 2). The cause for this may be due to the fact that isolation of hMSCs takes place on TCP, thus, a selection for hMSCs that attach to TCP is made. Despite this, the

specific growth rate (μ) uncovers two characteristics of hMSCs proliferation:

- (i) Proliferation kinetics decrease in cultures with steep concentration gradients (see chapter 4). Note that the slowest specific growth rates were estimated for 3D PEOT/PBT (Chapter 4) and the 3D-static Poly(ethylene terephthalate) (PTE) [8] when compared to all other studies with the exception of one study [7].
- (ii) Proliferation kinetics decrease in cultures under shear stress. Note that from low to high, the following range of specific growth rates were estimated for microcarrier cultures [16] and chapter 2 and 3D-perfusion PTE.

These two characteristic suggests that the factor that affects the most hMSCs proliferation kinetics are steep concentration gradients. However, as shown on chapter 4, concentration gradients may induce hMSCs into 3D patterns of proliferation and migration. Thus, in 3D cultures, fluid dynamics support hMCs proliferation and concentration gradients may induce a developmental response by hMSCs.

Table 1 hMSCs kinetics and culture conditions in this thesis and in the literature. Attachment surface, specific growth rates (μ), glucose consumption rates (q_g) and yield of lactate to glucose ($Y_{l/g}$). Means and standard deviations.

Chapter	Attachment surface (Fig.1)	μ [h^{-1}] $\times 10^{-2}$ mean of n = 3 donors*	q_g [moles/cell/h] $\times 10^{-12}$ mean of n = 3 donors*	$Y_{l/g}$ [q_l/q_g] mean of n = 3 donors*
1	Tissue culture plastic	1.6 ± 0.29	0.22 ± 0.09	1.95
2	Tissue culture plastic	1.57 ± 0.08	0.78 ± 0.15	1.81
2	Microcarriers * n=2	1.13 ± 0.06	0.6 ± 0.05	2.1
4	2D PEOT/PBT	1.01 ± 0.17	0.3 ± 0.35	0.89
4	3D PEOT/PBT	0.4 ± 0.34	0.6 ± 0.35	0.85
Ref.	Attachment surface	μ [h^{-1}] $\times 10^{-2}$	q_g [moles/cell/h] $\times 10^{-12}$	$Y_{l/g}$ [q_l/q_g]
Dos Santos et al.[15]	Tissue culture plastic	1.96 ± 0.02	0.6 ± 0.04	2
Schop et al.[16]	microcarriers	0.84 ± 0.6	0.3 ± 0.08	2.3
Lemon et al.[7]	Poly ethylene terephthalate (static)	5.54 ± 3.8	NA	NA
Zhao et al.[8]	Poly ethylene terephthalate (static)	$0.14 \pm NA$	NA	NA
Zhao et al.[8]	Poly ethylene terephthalate (perfusion)	$0.43 \pm NA$	NA	NA

NA-Not available.

When analyzed as a mean of hMSCs donors, glucose consumption rates (q_g) did not vary significantly between culture conditions (Table 1). However, differences in q_g were significant for the same donor in different culture conditions on chapters 1 and 4. hMSCs used glucose through glycolysis [17] as shown by the lactate to glucose yield ($Y_{l/g}$) (Table 1). Interestingly, this glycolysis trend was not present for hMSCs proliferating on PEOT/PBT. This could have been due to the low number of hMSCs cultured (Chapter 4) and low oxygen consumption rates by hMSCs [18]. These two factors together could account for maintaining an oxygen supply to hMSCs that prevented glycolysis.

The other possibility is that the mechanotransductive properties of PEOT/PBT could regulate how hMSCs use resources such as glucose. However, this needs further exploration. These results confirmed that there was a kinetic effect that was

dependent on nutrient availability.

Function follows form

The combination of nutrient availability with hMSCs proliferation could have a morphogenetic effect as explored on chapter 4. Kinetics of total collagen and glucosaminoglycans (GAG) also showed how nutrient availability can support 3D patterns. Extracellular matrix was found to be mostly composed of GAG, which supported hMSCs organization into circular patterns. These patterns showed that form was a direct result and consequence of hMSCs proliferation [19]. The possibility to direct tissue formation with gradients has interesting implications for the field of regenerative medicine. (i) chapter 4 showed mm scale proliferation and migration patterns. (ii) function follows form [20] is observed in circular 3D patterns.

Nutrients are essential for life, thus it would be reasonable to expect that nutrient competition awakens basic developmental responses by hMSCs [1, 2]. As a result, morphogenetic tissue patterns are formed that could develop a function if the suitable combination of physical and biochemical signals are provided. On chapter 4, the 3D circular patterns largely resemble vessels as they span the pore interconnectivity. Thus, providing shear stress and angiogenesis factors could be combined in a bioreactor (Chapter 3 and 4) to induce the development of hMSCs organization into mm size blood vessels in the 3D scaffolds.

Pathway flow

Kinetics suggested the presence of similar amino acid metabolic pathways in proliferating hMSCs (Chapter 2, fig. 1 A-B), regardless of culture conditions. These findings can pave the way for global pathway analysis [21, 22] of how components, quantities and regulation of processes occur in hMSCs. For example, amino acid metabolism patterns can introduce the quantification and flow of intracellular and extracellular components towards making extracellular matrix. In addition, with hMSCs proliferation kinetics defined in chapters 1, 2 and 4, other proliferating or differentiation signals can be removed or introduced to determine the kinetic response of hMSCs.

It is believed that hMSCs proliferation and differentiation do not occur at the same time. One possibility to test this would be to combine differentiation and proliferation media [3] and perform kinetic experiments to determine whether proliferation and differentiation can occur at the same time. This can be done by measuring and analyzing key markers of proliferation and differentiation markers such as those measured in chapter 4.

Highthroughput screening of tissue

The effects of physical phenomena on hMSCs culture can stimulate the invention of a broad range of technologies applicable to research, industry and medicine. Chapter 5 is an example of this, where the roles of diffusive mass transport and hMSCs proliferation stimulated the development of 3D aggregates in a well (Fig. 1D). Then, the sensorial abilities [23] of hMSCs were exploited in this chapter to create the 3D well macroarray system.

This high-throughput screening system significantly reduces the number of animals needed for *in vivo* experiments. This is also an example on how material-cell interactions can stimulate the implementation of controlled culture of 3D tissue *in vitro* and *in vivo*. Within the well, host's tissue and implanted cells interact in a controlled environment. This allows a multidimensional analysis of tissue behavior in a high-throughput manner. Novel imaging techniques and well macroarrays of different materials can greatly enhance the sensitivity of this technology to screen substances and tissue behavior in animal models.

Reverse engineering of tissues

In vitro 3D culture may not capture the full complexity of tissues any time soon. To mimic this complexity *in vitro*, we should understand the natural environment more fully. Therefore, it is time to increase the level of control (Chapter 5), analysis and monitoring [24] of implantations in animal models. Our state of the art technology in regenerative medicine already has the tools to develop sensitive materials and methods to monitor tissue in animal models [25]. Reverse engineering of tissue can create a return on investment beyond financial benefits: A supply chain. *In vivo* data provides basic knowledge of tissue biology; basic tissue biology channels into technology; and ultimately these fuse together to develop the medicine of the future.

References

1. Gurkan, U.A. and O. Akkus, *The mechanical environment of bone marrow: a review*. Ann Biomed Eng, 2008. **36**(12): p. 1978-91.
2. Forgács, G. and S. Newman, *Biological physics of the developing embryo*. 2005, Cambridge: Cambridge University Press. vi, 337 p.
3. McBeath, R., et al., *Cell shape, cytoskeletal tension, and RhoA regulate stem cell lineage commitment*. Developmental Cell, 2004. **6**(4): p. 483-495.
4. Rosel, D., et al., *Up-regulation of Rho/ROCK signaling in sarcoma cells drives invasion and increased generation of protrusive forces*. Mol Cancer Res, 2008. **6**(9): p. 1410-20.
5. Yourek, G., M.A. Hussain, and J.J. Mao, *Cytoskeletal changes of mesenchymal stem cells during differentiation*. ASAIO J, 2007. **53**(2): p. 219-28.
6. Titushkin, I. and M. Cho, *Modulation of cellular mechanics during osteogenic differentiation of human mesenchymal stem cells*. Biophys J, 2007. **93**(10): p. 3693-702.
7. Lemon, G., et al., *Mathematical modelling of human mesenchymal stem cell proliferation and differentiation inside artificial porous scaffolds*. Journal of Theoretical Biology, 2007(249): p. 543 - 553.
8. Zhao, F., et al., *Effects of oxygen transport on 3-D human mesenchymal stem cell metabolic activity in perfusion and static cultures: Experiments and mathematical model*. Biotechnol. Prog., 2005. **21**: p. 1269-1280.
9. MacArthur, B.D. and R.O.C. Oreffo, *Bridging the Gap*. Nature, 2005. **433**: p. 19.
10. Huebsch, N., et al., *Harnessing traction-mediated manipulation of the cell/matrix interface to control stem cell fate*. Nat Mater, 2010. **9**(6): p. 518-26.
11. Engler, A.J., et al., *Matrix elasticity directs stem cell lineage specification*. Cell, 2006. **126**(4): p. 677-689.
12. Ingber, D.E., *Tansegrity-based mechanosensing from macro to micro*. Progress in biophysics and molecular biology, 2008. **97**: p. 163 - 179.
13. Alberts, B., et al., *Molecular Biology of the Cell*. 5th ed. 2008, New York: Garland Science. 1268.
14. Curran, J.M., R. Chen, and J.A. Hunt, *The guidance of human mesenchymal stem cell differentiation in vitro by controlled modifications to the cell substrate*. Biomaterials, 2006. **27**(27): p. 4783-4793.
15. Santos, F.D., et al., *Ex Vivo expansion of human mesenchymal stem cells: A more effective cell proliferation kinetics and metabolism under hypoxia*. J. Cell. Physiol., 2010. **223**: p. 27-35.
16. Schop, D., et al., *Expansion of human mesenchymal stromal cells on microcarriers: growth and metabolism*. J Tissue Eng Regen Med, 2010. **4**(2): p. 131-40.
17. Schop, D., et al., *Growth, Metabolism and Growth Inhibitors of Mesenchymal Stem Cells*. Tissue Engineering: Part A, 2009. **15**.
18. Grayson, W.L., et al., *Effects of hypoxia on human mesenchymal stem cell expansion and plasticity in 3D constructs*. Journal of Cellular Physiology, 2006. **207**(2): p. 331-339.
19. Thompson, D.A.W. and J.T. Bonner, *On growth and form*. an abridged edition. / edited by John Tyler Bonner. ed. 1971, [S.l.]: Cambridge University Press.
20. Ingber, D.E., *Mechanical Control of Tissue Growth: Function Follows Form*. Proc

- Natl Acad Sci U S A, 2005. **102**(33): p. 11571- 11572.
21. Wang, J., et al., *Dependence of Mouse Embryonic Stem Cells on Threonine Catabolism*. Science, 2009. **325**(5939): p. 435-439.
22. Engler, A.J., et al., *Multiscale modeling of form and function*. Science, 2009. **324**(5924): p. 208-12.
23. Albrecht, D.R., et al., *Photo- and electropatterning of hydrogel-encapsulated living cell arrays*. Lab on a Chip, 2005. **5**(1): p. 111-118.
24. Bratlie, K.M., et al., *Rapid Biocompatibility Analysis of Materials via In Vivo Fluorescence Imaging of Mouse Models*. Plos One, 2010. **5**(3): p. -.
25. Huebsch, N. and D.J. Mooney, *Inspiration and application in the evolution of biomaterials*. Nature, 2009. **462**(7272): p. 426-32.

Summary

The main thesis in this book proposes that physical phenomena underlies the formation of three-dimensional (3D) tissue. Cells and tissues maintain 3D function and organization in the human body despite experiencing various types of biological and physical stimuli at the same time. Cells of musculoskeletal tissues respond specifically to changes in pressure, concentrations and chemical composition. For example, in musculoskeletal tissues, changes in pressure (hydrostatic pressure, shear stress) determine whether mesenchymal stem cells (MSCs) become cartilage or bone cells (differentiation). Thus, not only biological signals, but also physical signals can induce cell differentiation and tissue regeneration (Introduction).

Hence, if biological and physical signals are well understood, MSCs differentiation potential could be harnessed to develop therapies to cure or treat diseases and trauma of musculoskeletal tissues. However, there exist two major challenges: One, MSCs are found in low numbers in the human body. Therefore, expansion (proliferation) is necessary. Second, the biology of MSCs (and Tissue) in 3D is largely unknown. In this thesis, tissue regeneration with mesenchymal stem cells is studied through the law of conservation of mass, which states that mass is converted and it is not created nor destroyed. Both challenges; MSCs proliferation and 3D tissue formation are explored from 2D to 3D conditions. The kinetics of proliferation is the unifying principle to compare and analyze the behavior of human MSCs (hMSCs) through the quantification of the movement or conversion of mass during proliferation.

The 3D tissue environment is stimulated by various types of physical stimuli. This thesis focuses on the kinetics of proliferation of hMSCs under two physical phenomena (Diffusive mass transport and shear stress). Under the effects of diffusive mass transport in 2D, the kinetics of hMSCs cultured at different starting cell numbers (seeding densities) are studied in chapter 1. It was expected that proliferation kinetics would be the same at both seeding densities. Surprisingly, lower seeding densities show higher reaction rates of glucose, lactate, glutamine and glutamate. These results indicate that hMSCs kinetics are sensitive to the seeding density. Thus, starting with a low number of hMSCs results in higher metabolic rates and more efficient proliferation.

To further explore the kinetics, hMSCs were cultured under both diffusive mass transport and shear stress (Chapter 2). It was expected that hMSCs would maintain a kinetic pattern despite experiencing major culture differences. 20 amino acids were measured and their kinetics established. It was determined that 14 amino acids' kinetics were consistent under both diffusive mass transport and shear stress. 11 amino

acids were consumed and 3 amino acids were produced by hMSCs in both culture conditions. The importance of this lies in that there are metabolic processes during hMSCs proliferation that are independent of physical parameters. Thus, depending on culture parameters, hMSCs' proliferation kinetics vary in quantity (Chapter 1 and 2), but not in the overall pattern of consumption or production processes.

Proliferation kinetics unraveled differences and similarities of hMSCs culture in 2D (Chapters 1 and 2). Before exploring the kinetics of hMSCs in 3D, the shear stress profile in 3D culture was assessed (Chapter 3). This chapter estimates the shear stress regimes that MSCs experience in 3D culture. This characterization provides Darcian permeability constants to include in the design of 3D scaffolds.

hMSCs proliferation in static 2D and 3D culture and in 3D bioreactor culture is the subject of chapter 4. The main purpose in this chapter is to explore 3D tissue formation with hMSCs under diffusive mass transport (static) and shear stress (bioreactor). These results show that 3D tissue formation correlates with concentration gradients that were estimated through computational fluid dynamics. The kinetics of proliferation of hMSCs under both 2D and 3D indicate that hMSCs proliferate slower in 3D than in 2D, but achieve a higher degree of organization in 3D. These suggest that 3D tissue formation with hMSCs can be driven by higher concentration of nutrients (Chemotaxis).

In chapter 5, hMSCs chemotactic behavior is explored in another 3D environment. The result is that hMSCs organized into 3D tissue in the direction where higher concentration of nutrients are expected. The practical application of 3D tissue formation by hMSCs is further explored in this chapter towards the development of an *in vivo* high throughput screening (HTS) system. This HTS system offers the possibility to screen multiple conditions in animal models, thereby significantly decreasing the costs and lives sacrificed in animal experiments.

The general discussion provides an analysis of the results presented in this thesis. A strategy to mathematically model musculoskeletal tissues is presented. In addition, this chapter analyzes the proliferation kinetics of hMSCs in the context of the available literature and towards metabolic pathway flow analysis. Furthermore, this chapter speculates on how physical phenomena affect the theory of function follows form and applications in high throughput screening and reverse engineering of musculoskeletal tissues.

Samenvatting

De belangrijkste stelling in dit boek zegt dat fysische verschijnselen ten grondslag liggen aan de vorming van driedimensionaal (3D) weefsel. In het menselijk lichaam houden cellen en weefsels een 3D functie en organisatie ondanks de verschillende soorten biologische en fysische prikkels die tegelijk worden ervaren. Cellen in musculoskeletaal weefsels spelen in op veranderingen in druk, concentratie en chemische samenstelling. Veranderingen in druk (hydrostatische druk, schuifspanning) bepalen in deze weefsels bijvoorbeeld of mesenchymale stem cellen (MSCs) kraakbeen of bot cellen worden (differentiatie). Niet alleen biologische- maar ook fysische signalen kunnen dus de differentiatie van cellen en regeneratie van weefsels induceren (inleiding). Kennis en begrip van biologische en fysische signalen kan dus bijdragen aan de ontwikkeling van therapieën, waarbij de differentie van MSCs wordt gebruikt om ziektes en trauma's van het musculoskeletaal weefsel te genezen of behandelen. Er zijn echter twee grote uitdagingen; (i) Het aantal MSCs aanwezig in het menselijk lichaam is zeer laag. Daarom is expansie (proliferatie) een noodzakelijke stap. (ii) De biologie van MSCs (en weefsels) in een 3D organisatie is grotendeels onbekend.

In dit proefschrift wordt weefselregeneratie door MSCs bestudeerd met behulp van de wet van behoud van massa, welke stelt dat massa omgezet wordt, maar niet wordt gecreëerd of vernietigd. Beide uitdagingen; de proliferatie van MSCs en de vorming van 3D weefsel worden onderzocht van 2D naar 3D. De kinetiek van proliferatie is het principe van eenheid te vergelijken en te analyseren het gedrag van mens MSCs (hMSCs) waarbij kwantificatie van de beweging of de omschakeling van de massa tijdens proliferatie mogelijk is. De proliferatie kinetiek vormt het principe voor de vergelijking en analyse van het gedrag van humane MSCs (hMSCs) tijdens de kwantificatie van beweging of de omzetting van massa tijdens de proliferatie.

Het 3D weefsel milieu wordt beïnvloed door verschillende fysische verschijnselen. Dit proefschrift richt zich op de kinetiek van de proliferatie van hMSCs gedurende twee fysische verschijnselen (schuifspanning en massatransport door diffusie). Als onderdeel van massatransport door diffusie, wordt in hoofdstuk 1 de kinetiek van hMSCs op verschillende zaaidichtheden bestudeerd. De verwachting was dat proliferatie kinetiek hetzelfde zou zijn bij verschillende zaaidichtheden. Tot onze verrassing bleek echter dat lagere zaaidichtheden resulteren in grotere hoeveelheden glucose, lactaat, glutamine en glutamaat. Deze resultaten duiden erop dat de kinetiek van hMSCs afhangt van de zaaidichtheid en dat het zaaien van lage aantallen hMSCs leidt tot een snellere stofwisseling en efficiëntere proliferatie.

Om de kinetiek verder te onderzoeken hebben we hMSCs proliferatie onder zowel

diffuse massatransport en schuifspanning (hoofdstuk 2) onderzocht. De verwachting was dat hMSCs hetzelfde kinetische patroon behouden, ondanks grote verschillen in kweek condities.

20 aminozuren werden gemeten, en vastgesteld werd dat de kinetiek van 14 aminozuren zowel onder diffuse massatransport en schuifspanning consistent is. 11 aminozuren werden verbruikt en 3 aminozuren werden geproduceerd door hMSCs in beide condities. Het belang van deze metingen ligt in het feit dat bepaalde metabolische processen onafhankelijk zijn van fysische parameters. Afhankelijk van de kweekcondities varieert de proliferatie kinetiek van hMSCs dus in kwantiteit (hoofdstuk 1 en 2), maar niet in het algehele consumptie- of productie-patroon.

Kinetiek van de proliferatie heeft verschillen en overeenkomsten ontrafelt van hMSCs in 2D-kweek (hoofdstuk 1 en 2). Voordat de kinetiek van hMSCs in 3D is onderzocht werd de schuifspanning in 3D onderzocht (hoofdstuk 3). Dit hoofdstuk raamt de schuifspanning regimes die hMSCs in 3D-kweek ervaren. Deze karakterisatie geeft Darcian permeabiliteit constanten welke gebruikt kunnen worden in het ontwerp van 3D scaffolds.

De proliferatie van hMSCs in statische 2D- en 3D-kweken en in 3D bioreactor kweken is het onderwerp van hoofdstuk 4. Het voornaamste doel in dit hoofdstuk is het onderzoeken van 3D weefsel formatie door hMSCs onder invloed van diffusie massatransport (statisch) en schuifspanning (bioreactor). Deze resultaten tonen aan dat 3D weefsel formatie correleert met concentratie gradiënten welke zijn bepaald met behulp van *computational fluid dynamics*. De kinetiek van hMSC proliferatie in zowel 2D als 3D tonen aan dat hMSCs langzamer vermenigvuldigen in 3D dan in 2D, maar dat hMSCs in 3D een hogere organisatie graad bereiken. Dit suggereert dat 3D weefsel formatie met hMSCs door een hogere concentratie voedingsstoffen (chemotaxis) wordt aangedreven.

In hoofdstuk 5 wordt het chemotactische gedrag van hMSCs in een andere 3D-omgeving onderzocht. Hieruit bleek dat hMSCs in 3D organiseren in de richting van hogere concentraties voedingsstoffen. De praktische toepassing van 3D weefsel formatie door hMSCs is in dit hoofdstuk verder onderzocht met als doel de ontwikkeling van een *in vivo high throughput screening* (HTS) systeem. Dit HTS-systeem biedt de mogelijkheid om meerdere condities in diermodellen te screenen, waardoor de kosten en het aantal benodigde dieren voor dierexperimenten significant worden verlaagd.

De algemene discussie geeft een analyse van de gepresenteerde resultaten uit dit proefschrift. Er wordt een strategie voorgesteld om musculoskeletaal weefsels wiskundig te modelleren. Daarnaast wordt in de hoofdstuk een vergelijking gemaakt tussen de proliferatie kinetiek van hMSCs en de beschikbare literatuur.

Verder wordt in dit hoofdstuk gespeculeerd over hoe fysische verschijnselen de *function follows form* theorie beïnvloeden en over de toepassingen in *high throughput screening* en *reverse engineering* van musculoskeletaal weefsels.

Resumen

La tesis principal tratada en este libro propone que los fenómenos físicos son la base fundamental para la formación tri-dimensional (3D) de tejido. Las células y tejidos mantienen las funciones y organización 3D del cuerpo humano a pesar de experimentar varios tipos de estímulos biológicos y físicos a la vez. Las células en tejido musculo esquelético responden específicamente a cambios en presión, concentración y composición química en el entorno celular. Por ejemplo, en estos tejidos, los cambios en presión (presión hidrostática y tensión de corte) determinan si las células madre mesenquimales (MSCs) se convierten en tejido cartilaginoso u óseo (diferenciación). Por lo tanto, no solamente señales biológicas sino también señales físicas, pueden inducir la diferenciación celular y regeneración de tejido (Introducción).

Si estas señales son identificadas, el potencial de diferenciación de MSCs puede ser direccionado a desarrollar terapias para curar o tratar enfermedades y trauma de tejido músculo esquelético. Sin embargo, existen dos retos importantes: Primero, en el cuerpo humano las MSCs existen en números muy bajos. Por ende, su expansión (proliferación) es necesaria. Segundo, gran parte de la biología de las MSCs (y el tejido) en 3D es aún desconocida. En este trabajo la regeneración de tejidos con MSC es estudiada por medio de la ley de conservación de masa que propone que la masa se convierte pero no puede ser ni creada ni destruida. Ambos retos, proliferación de MSCs y formación 3D de tejido son explorados en 2D y 3D. La cinética de proliferación es el principio unificador para comparar y analizar el comportamiento MSCs humanas (hMSCs) por medio de la cuantificación del movimiento o conversión de masa durante la proliferación celular.

El entorno 3D de tejido es estimulado por varios tipos de estímulos físicos. Esta tesis trata la cinética de proliferación de hMSCs en la presencia de dos tipos de estímulos físicos (Difusión de masa y tensión de corte). Bajo los efectos de difusión de masa en 2D la cinética de hMSCs cultivadas con concentraciones iniciales diferentes (Densidad de siembra) son estudiados en el capítulo 1. Se esperaba que la cinética de proliferación fuera similar con densidades de siembra diferentes. Sorprendentemente, bajas densidades de siembra mostraron más altas velocidades de metabolismo en glucosa, lactosa, glutamina y glutamato que altas densidades de siembra. Estos resultados indican que la cinética de hMSCs es sensible a la densidad de siembra de hMSCs. En consecuencia bajas densidades de siembra de hMSCs resultan en altas velocidades de metabolismo y una proliferación eficiente de hMSCs.

Para explorar la cinética de proliferación más a fondo hMSCs fueron cultivadas bajo difusión de masa y tensión de corte (Capítulo 2). Se esperaba que las hMSCs mantendrían un patrón cinético de metabolismo a pesar de experimentar diferencias significativas en las condiciones de cultivo. Se midieron 20 aminoácidos y se estableció su cinética de consumo. Se determinó que la cinética de 14 aminoácidos es consistente en la presencia de difusión de masa y tensión de corte. Independientemente del estímulo físico en las hMCS 11 aminoácidos fueron consumidos y 3 producidos. La importancia de este resultado es que hay procesos metabólicos que son independientes de parámetros físicos. Dependiendo de los parámetros de cultivo la cinética de proliferación de hMSCs varía en las velocidades del metabolismo (Capítulos 1 y 2) pero no en los patrones generales de los procesos de consumo o producción.

La cinética de proliferación hace evidente donde están las diferencias y similitudes en el cultivo de hMSCs en 2D (Capítulos 1 y 2). Antes de explorar la cinética de proliferación de hMSCs en 3D, se estudia la tensión de corte que las MSCs experimentan en 3D. Esta caracterización de entorno 3D resulta en constantes de permeabilidad Darcian que pueden ser incluidas en el diseño de andamios 3D.

La proliferación de hMSCs en sistema estático en 2D y 3D y en un cultivo 3D en bioreactor es el tema de el capítulo 4. El propósito principal de este capítulo es explorar la formación 3D de tejido con hMSCs bajo la presencia de difusión de masa (estático) y tensión de corte (Bioreactor). Estos resultados muestran que la formación 3D de tejido está correlacionada con los gradientes de concentración que fueron estimados por medio de dinámica de fluidos. La cinética de proliferación de hMSCs en 2D y 3D indica que las hMSCs proliferan más lentamente en 3D que en 2D, pero alcanzan un grado más alto de organización en 3D. Esto sugiere que la formación 3D de tejido con hMSCs puede ser dirigido por altas concentraciones de nutrientes (Quimiotaxis).

En el capítulo 5 el comportamiento quimiotáctico de hMSCs es explorado en otro entorno 3D. El resultado es que las hMSCs se organizan en tejido 3D en la dirección donde están las concentraciones más altas de nutrientes. La aplicación práctica en la formación 3D de tejido con hMSCs es investigada en este capítulo hacia el desarrollo de un sistema *in vivo* de selección de alto rendimiento (HTS - *high throughput screening*) que ofrece la posibilidad de analizar múltiples condiciones en modelos animales, reduciendo de manera significativa los costos y vidas sacrificadas en experimentos con animales.

La discusión general presenta un análisis de los resultados obtenidos en esta tesis. Se incluye también, una estrategia para simular matemáticamente los tejidos músculo-esqueléticos. Este capítulo analiza la cinética de proliferación de hMSCs

con respecto a la literatura disponible y hacia el análisis de caminos metabólicos. Además, se especula sobre cómo los fenómenos físicos afectan la teoría de “función sigue la forma” y las aplicaciones en HTS e ingeniería reversa de tejidos músculo-esqueléticos.

Acknowledgements

The last four years have been an incredible journey of personal and professional discovery. I want to thank Prof. Clemens van Blitterswijk for giving me the opportunity to do my Ph.D. research in his laboratory. I have nothing but admiration for you both as a person and as a scientist. Also, I want to thank Dr. Anton van Boxtel for his patience and support throughout my studies in the Netherlands. You are one of the brightest people I have ever met, you have taught me many, many important lessons so far. Clemens, Ton, Marcel, Jan, Roman, Pamela, Aart and last but not least, Lorenzo. Each one of you has been a role model to me. I hope that the professional that I am, and that I hope to develop into, has a bit of each one of you.

My buddies of 145! Anand, Hemant and Nico: We went through funny, difficult and rewarding experiences by sharing the office. We share a special bond because we got to know each other so well. I hope your careers flourish and our friendship grows. Our office was never the most organized, but it was without a doubt the most unusual and interesting.

Petra, Joost, and Nils: It was a privilege to work so closely with you. Your hard work and dedication can be found throughout this thesis. You will accomplish anything you set out to do. Your assignments were as much a learning experience for me as they were for you.

The international atmosphere in TR was stimulating in all fronts. I think we may even have created a dialect of English called TR-English. The warmth of the people in our lab made you my family away from home. Hugo, Ana and Andrei: We can say that everyone in the lab speaks “some” Portuguese because of you. De beste voetbal kapitein, Joyce: Hartelijk bedankt voor de hulp met de samenvatting. Alice: Your laughter and good spirit are contagious. Jun and Nan: I wish you the best with all your plans. Anouk: Je geduld met ons in de TC lab is bewonderenswaardig. Jacqueline: Je antwoorden en opmerking op mijn vragen waren altijd handig. Anandita, Karolina, Jeroen, Liliana, Bin, Ling, Bjorn, Charlene, Tim, Wim, Anne, Mijke, Janneke and Nathalie: Good luck and enjoy the rest of your projects. Jeroen R: Korea with you and Shakti was a memorable trip. Juan: Te convertiste en un gran compañero y amigo durante los años que vivimos en Hengelo. Cuanto hablamos! Muchas felicidades para ti y Sandra. Audrey en Joyce: Bedankt voor alles; chit-chat, veel afspraken en proefschrift administratie. Jet: Je bent een verwonderende en begenadigde docent. Na ik je les had vond ik het Nederlands een interessant taal.

Frank: I do not know what I would have done without you during the first two years of my research. Intervet is lucky to have you. Deborah: It has been a pleasure

Acknowledgements

to get to know you, study and work with you these last 6 years. Joost: Thank you for your support during STEX. Riemke: That very first experiment you proposed to me was the right push in the right direction. Davide: I have the feeling you can find a solution to almost every problem. Yuan: I admire you because you have made a rock into both a scientific and commercial success. Jeanine: Your Ph.D. thesis was always on my desk.

Prof. Luz marina Restrepo: Gracias por tus comentarios en el resumen. Espero que tengamos la oportunidad de llevar acabo algún proyecto de colaboración.

Tolis, Julien, Vanessa, Carlos, Fiona, Jean, Marta, Stelios, Jan, Olga, Isabel, Lorena, Sole y Carla: You have made adjusting to Rotterdam a very easy and fun ride!

Ishay, Sabina, Ben, Julia, Baci, Jorge, Marzia and Aldana: I look forward to every one of our gatherings. These have been therapeutical during my life in the Netherlands. Jorge: Gracias por tus comentarios en la introducción.

Manu: Creo que al final achique el agua pero no los agradecimientos. Vegueros: Habrá que asistir a todos los toros embolados antes de que nos los prohíban.

Lorenzo: Hacemos un dúo científico y carranguero fenomenal. En este ultimo año fuiste un gran tutor. Me sentí en mi tierrita contigo y Vicky.

Gerardo: Has sido un hermano en Holanda. Ishay, you and me will not be satisfied until we have cruised every slope on the Alps.

Ximo, Jose y en general los Hermoso me han hecho sentir como a un hijo o primo mas. Y como tal, la Vega se ha convertido en un destino anual al cual no quiero faltar. Primo: Hoy desde Madrid y Rotterdam, mañana desde cualquier lugar del mundo. Tenerlo “cerca” ha sido un gran apoyo.

Fabio, Melissa, tio Armando y Antonio: No estaría aquí si no fuera porque ustedes creyeron en mi. Le dedico este libro a mis abuelos porque si no fuera por ellos ningún Higuera o Sierra existiría: Soy muy afortunado de que sean mi familia.

Mi Clarita: Tu inquebrantable comprensión, inteligencia y apoyo están plasmadas en cada una de estas páginas. Tú me das fortaleza para creer y hacer de nuestros sueños una realidad.

Papa, Mama, Jota y Jaime: Su apoyo y amor son una fuerza que jamás se podría medir. Ustedes y Clara son el comienzo y el final. Lo más importante para mí.

Now, let's turn the page...

Gustavo, Rotterdam, 2010.

A lot of people never use their initiative because no-one told them to

BANKSY

List of Publications

- Vossenbergh P., **Higuera G.A.**, van Straten G., van Blitterswijk CA. and van Boxtel A.J. Darcian Permeability Constant as Indicator for Shear Stresses in Regular Scaffold Systems for Tissue Engineering. **Biomech Model Mechanobiol.** 2009 Apr 10.
- **Higuera G.A.**, Schop D., Janssen F., van Dijkhuizen-Radersma R., van Boxtel A. and van Blitterswijk CA. Quantifying in Vitro Growth and Metabolism Kinetics of Human Mesenchymal Stem Cells Using a Mathematical Model. **Tissue Eng Part A.** 2009 Sep;15(9):2653-63.
- Tan Q., El-Badry A.M., Contaldo C., Steiner R., Hillinger S., Welti M., Hilbe M., Spahn DR., Jaussi R., **Higuera G.A.**, van Blitterswijk CA. Luo Q. and Weder W. The Effect of Perfluorocarbon-Based Artificial Oxygen Carriers on Tissue-Engineered Trachea. **Tissue Eng Part A.** 2009 Sep;15(9):2471-80.
- Papenburg B., Liu J., **Higuera G.A.**, Barradas AM., de Boer J., van Blitterswijk CA., Wessling M. and Stamatialis D. Development and Analysis of Multi-Layer Scaffolds for Tissue Engineering. **Biomaterials.** 2009 Oct; 30(31):6228-39.
- Bat E., Kothman B., **Higuera G.A.**, van Blitterswijk C.A., Feijen J., Grijpma D.W. Ultraviolet Light Crosslinking of Poly(trimethylene carbonate) And Its Application In Preparing Elastomeric Tissue Engineering Scaffolds. **Biomaterials.** Accepted. Aug, 2010.

- Patent application number: EP10168610.3 **Gustavo A. Higuera**, Joost van Dalum, Lorenzo Moroni, and Clemens A. Van Blitterswijk. High-throughput multiwell system for culturing 3D tissue constructs in-vitro or in-vivo, method for production said multiwell system and methods for preparing 3D tissue constructs from cells using said multiwell system. Date filed: 06-July-2010.

Curriculum Vitae

Gustavo Andrés Higuera Sierra was born on January 25th, 1979 in Tunja, Boyacá, Colombia. In Tunja, he attended the *Gimnasio Campestre del Norte*, where his fascination with the life sciences was patiently nurtured. In 2002, he obtained his Bachelor of Science in Biology degree at the University of Texas at Austin. During 2005, he worked on the production and characterization of structured materials made in a micro-fluidic device at Unilever Colworth in England. In 2006, he graduated from Wageningen University in The Netherlands with a Master of Science in Biotechnology. Under the supervision of Dr. Anton van Boxtel, he analyzed the dynamics of *hybridoma* metabolism. This resulted in a master thesis entitled “Dynamic Metabolic Flux Measurement for Hybridoma Cells”. His interests in biological and engineering sciences led him in 2006 to the laboratory of Prof. Clemens A. Van Blitterswijk at the University of Twente in The Netherlands. The research performed at the University of Twente is the subject of this dissertation. During his doctorate research, he has received awards such as a travel grant award to the engineering principles in biological systems meeting at Cold Spring Harbor Laboratory (U.S.A) and the young investigator award by the Tissue Engineering and Regenerative Medicine Society (TERMIS) in London, England.

A grayscale microscopic image showing a complex, interconnected network of cells or fibers, likely representing a 3D tissue structure. The cells are elongated and spindle-shaped, forming a dense, porous mesh. The background is dark, and the cells are lighter, creating a high-contrast, textured appearance.

Stellingen Bij Het Proefschrift
Statements With This Dissertation

3D Tissue Formation
The Kinetics Of Human
Mesenchymal Stem Cells

Gustavo A. Higuera
September 2010

1. If food produces tissue mass, then the key to regenerate tissues could be to discover how much and what tissue is produced by a certain amount of food (This thesis).
2. Two-dimensional tissue regeneration conceals the fact that tissue regeneration is, in engineering terms, an “up-scaling” problem (This thesis).
3. How fast would have Astronomy progressed without physical principles? Under those circumstances, Astronomy would have evolved at about the same pace as the field of tissue regeneration.
4. *Bioreactors offer control over two types of physical phenomena: Mass transport and mechanical conditioning* (I. Martin et al. (2004) Trends in Biotechnology: 22; (2)). Not all tissues require these types of physical phenomena. Therefore, it is fundamental to quantitatively distinguish biological processes that are directly affected by physical phenomena. Only then can the control over physical phenomena in bioreactors be exploited to the fullest of its potential to induce 3D tissue development.
5. In developmental biology tissue morphology can result from various biological processes. One of them maintains that *form can be a direct resultant and consequence of growth* (D’arcy Thompson). This biological process can be exploited to robustly induce 3D tissue regeneration with stem cells.
6. The extracellular matrix (ECM) structurally supports 3D tissue development. Therefore, ECM dynamics are of strategic importance to engineer tissues (This thesis).
7. When analyzing biological processes through mathematical models it is important to realize that *all models are wrong, but some models are useful* (Unknown).
8. The manner in which nutrients stimulate the activity of stem cells could be analogous to the following biological situation: Bears hibernate when there is little food in their habitat. Conversely, bears are active when food becomes available (This thesis).
9. High-throughput screening (HTS) lacks tools to analyze 3D tissue. Hence, one possibility for successful scientific and industrial application of 3D HTS could be to incorporate sensors into HTS systems.
10. Nature provides many examples where one organism or cell invests time and energy on performing one small and seemingly insignificant task. When all organisms or cells in a community or population perform this one task, all organisms ultimately benefit. *We don’t need any more heroes, we just need someone to take out the recycling* (Banksy).